



POLITECNICO DI MILANO
MECHANICAL ENGINEERING DEPARTMENT
DOCTORAL PROGRAMME IN MECHANICAL ENGINEERING

BIO-INSPIRED COMPOSITE MATERIALS: FROM HUMAN BONE TO BONE-LIKE COMPOSITES

Doctoral Dissertation of:
Flavia Libonati

Supervisor:
Prof. Laura Vergani
Prof. Markus J. Buehler

Tutor:
Prof. Bianca M. Colosimo

Coordinator:
Prof. Bianca M. Colosimo

Year 2012-Cycle XXV

Acknowledgement

This Thesis project is carried out part in the Department of Mechanical Engineering of Politecnico di Milano, under the supervision of Professor Laura Vergani, and part in the Laboratory of Atomistic and Molecular Modeling (LAMM) of Massachusetts Institute of Technology, under the supervision of Professor Markus J. Buehler, where I did a period of research as visiting student. The experiments are supported by the technical staff of the Department of Mechanics of Politecnico di Milano. The numerical simulations are performed on the LAMM cluster (MIT), and on the FERMI cluster (CINECA, Italy). I would like to thank all the people involved in my research for the support given to me. My special thank goes to my thesis advisor, Professor Laura Vergani, for her guidance, encouragement, support, and for giving me the opportunity of doing a research period abroad. I am also grateful to her for providing me with the opportunity to take part to academic activities and to be involved in different research projects. Sincere gratitude goes to my co-advisor, Professor Markus J. Buehler, for giving me the opportunity of working in his research group, and for opening me the door of research in bone and atomistic modeling. I would also like to thank him for his encouragement, guidance, support, and continuous advices. A special thank goes to Progetto Rocca, for giving me the opportunity of doing research at MIT. It was an incredible life experience, where work, colleagues, friendship, all of them contribute to make it unique! Thanks to Progetto Rocca, I could explore a new field of research, learning something new every day in a lively and stimulating environment, like MIT, and creating a bridge with my lab at Politecnico. I would also like to show my gratitude to my colleagues at MIT, for their countless advices, and in particular to my officemate, Ph.D. Arun K. Nair, for his willingness and support. Furthermore, I would like to thank my officemates and 'corridormates' in Politecnico: "I miss all of you guys a lot during my research period in the U.S., and unfortunately some of you had already moved when I came back!". I am very grateful to Chiara, who has been my tutor since the Bachelor, to Ramin, who introduced me to LaTeX, and to the administrative assistant of the Department of Mechanical Engineering, Licia Simonelli for her friendship and support during my graduate studies. My thanks also go to the technical staff of the Department of Mechanical Engineering of Politecnico di Milano, which help me with testing machines and laboratory tools. My gratitude also goes to Alessandro Panizio, the MSc student, who carried out the manufacturing process in the laboratories of the Technical University of Clausthal, and to Professor Ziegmann (Technical University of Clausthal), who actively collaborates to the project. Moreover, I would like to thank Professor Miccoli, from Politecnico di Milano, for his valuable advices for the computational time optimization. A special thought goes to my MSc thesis advisor, emeritus Professor Robert D. Adams (University of Oxford) who strongly encouraged me to do a PhD: his words have been a great support during the past years! A great thank to all of my friends, for supporting and encouraging me to face this challenge, and to my roommates, to make me feel at home!

The last, but most important THANK goes to my family and in particular to my lovely parents, for their support throughout my study and for their encouragement for each new challenge.

Abstract

B IOMIMETICS is an engineering design approach to create new structures, by reproducing characteristics found in nature. Indeed, in nature it is possible to find many smart solutions, which can be mimicked to build new materials, with potential applications to various engineering fields. Research in biomimetics has led to the development of a large number of innovative materials and technological solutions, such as gecko-like adhesives, self-repairing materials, self-cleaning materials, lightweight wood-like composites, and new bio-inspired nanocomposites. Nature is the largest producer of composite materials: wood, bone, nacre, all of them are examples of composite materials. Wood is a natural composite made of cellulose fibers and a resinous matrix, the polysaccharide lignin. Bone, teeth, mollusc shells, are all made of organic-inorganic composite materials, consisting of hard ceramic reinforcing phases embedded into natural organic polymer matrices. The latter biocomposites, also known as bone-like materials or biominerals, are characterized by a hierarchical structure, consisting of a highly controlled organization at different levels, with characteristic structural dimensions at each level, ranging from the nanometer to the macroscopic length scale. This results in a complex architecture, which provides the material with multifunctional properties. The controlled growth and the specific size of the components of the biocomposites, resulting from the biomineralization process, play a crucial role in determining the mechanical performance of the whole composite; hence, there is an increasing interest among researchers to understand the mechanisms behind the controlled biomineralization. Among biocomposites, an intriguing material is the human bone, a composite of collagen and hydroxyapatite. Bone is considered as a biomineral, due to the high content of calcium-phosphate minerals, which make it hard and stiff. However, a common characteristic of bone is the incredible toughness, in spite of its brittle mineral components; in fact, bone toughness is about three to five orders of magnitude more than that of the mineral it is made of. Until now, no conventional man-made composite material has reached such an amplification in toughness, compared to the raw components; for this reason bone is considered as a biomimetic model material. The reasons of the toughness and ductility of this materials have to be seek in the hierarchical organization. The key mechanisms, which make it a quasi-ductile and damage-tolerant material, with an increased toughness, are different and act at various length scales. The simultaneous operation of toughening mechanisms, acting at different length scales, provides the bone with its enduring strength and toughness. Hence, to understand the effects of the hierarchy on the mechanical response of bone, and the structure-property relationship, it is worthwhile to use a multi-scale approach. In this work, after a deep study of the bone hierarchical structure, an atomistic approach is used to get an insight into the mechanical properties of the bone building blocks, the collagen organic fibers and the hydroxyapatite (HAP) mineral crystals. Full atomistic simulations are carried out to get information about the mechanical behavior of the bone basic components, their interactions and the size effect on their mechanical performance, and in particular on the

fracture behavior of the brittle mineral components. Indeed, the mechanical response of HAP crystals in presence of a defect is studied, by means of an atomistic approach, and the effect of confinement on their fracture behavior is investigated. A systematic variation of the crystal size allows to identify a critical size, below which the material becomes flaw tolerant, approaching a constant level of strength, regardless the presence of the defect. The concept of size-driven flaw tolerance is very common for natural materials, confirming the importance of characteristic size in smart natural systems. A further study of the confinement effect is carried out, by performing molecular dynamics simulations, on bone nanocomposites, made of HAP crystals and collagen fibers. This study confirms the hypotheses of a positive size-effect on the mechanical performance of these material at the sub-nanoscale. At the meantime, a biomimetic approach is used to create a new material, with the aim of replicating some of the toughening mechanisms operating in bone and harnessing them in engineering materials. Hence, by observing the bone structure, selected structural features of bone, the osteons, characteristic of the secondary haversian structure of bone at the micro-scale (*i.e.* μm to mm), are implemented in a new glass-carbon/epoxy synthetic composite, which could replicate the toughening mechanisms of crack deflection and twisting. The osteon-like structure is chosen for the simple geometry and the for the role played in enhancing the toughness, by deflecting and twisting the crack. Conventional structural materials, widely used in the field of composites, such as glass fibers, carbon fibers and epoxy matrix, are chosen for the new structural materials. The initial design is simplified to make it feasible, with respect to the available manufacturing process. The material is manually laminated and characterized, by performing experimental tests (*i.e.* tensile, compression, three point bending, fracture toughness) according to ASTM standards. Also, microscopic analyses are performed to get an insight into the fracture process. Moreover, in order to assess if the bio-inspired composite could really offer improved mechanical properties, compared to existing structural materials, a classical laminate, with the same type and amount of fibers and resin of the osteon-like composite, is created and tested, to allow a direct comparison. The new concept of bio-inspired material is not meant to be a mere copy of what is found in nature, but instead it should provide a smart solution for engineering problems. Until now, it is only a first solution, which could be optimized, by adding reinforcing nano-structural elements with proper shapes and characteristic sizes, as suggested by the results of full atomistic simulations. This work is carried out jointly at the LAMM (Laboratory of Atomistic and Molecular Modeling) of MIT, where molecular dynamics simulations are carried out under the supervision of Prof. Markus J. Buehler, and the Department of Mechanical Engineering of Politecnico di Milano, under the supervision of Prof. Laura Vergani, where the design and the experimental characterization of the new bio-inspired material and of the comparative laminate are performed. The manufacturing process of the materials is carried out at the Technical University of Clausthal (Germany), thanks to a collaboration with the laboratory directed by Prof. Ziegmann.

Contents

I	Introduction	1
1	Biomimetics: learning from Nature	3
1.1	Introduction	3
1.2	The History of Biomimetics	4
1.3	Biomimetic Approach	6
1.4	Biological Materials and Bio-inspired Materials	7
1.5	Bone	10
1.5.1	Bone Composition	11
1.5.1.1	Collagen	11
1.5.1.2	Hydroxyapatite	12
1.5.2	Biom mineralization	12
1.5.3	The Hierarchical Structure of Bone	13
1.5.4	Mechanical Properties of Bone	14
1.5.5	Aging and Disease	16
1.6	Outline	17
	Bibliography	18
2	Introduction to Composite Materials	25
2.1	Introduction	25
2.2	Composites for Structural Applications	26
2.2.1	The Reinforcement	26
2.2.1.1	Fiber Reinforcement: Inorganic Fibers	27
2.2.1.2	Fiber Reinforcement: Carbon Fibers	28
2.2.1.3	Fiber Reinforcement: Polymeric Fibers	28
2.2.2	The matrix	29
2.2.2.1	Polymer Resins	30
2.2.2.2	Metal Matrices	31
2.2.2.3	Ceramic Matrices	31
2.2.3	The interface and the sizing	31
2.2.4	The Manufacturing Techniques	32
2.2.4.1	Wet Lay-up	32
2.2.4.2	Spray Lay-up	33
2.2.4.3	Pultrusion	33
2.2.4.4	Filament Winding	33
2.2.4.5	Resin Transfer Molding - RTM	33
2.2.5	The Applications	34
2.3	Bio-Inspired Composites	35

2.4	Outline	36
	Bibliography	38
II	Numerical simulations	39
3	Introduction to Atomistic Modeling of Materials	41
3.1	Introduction	41
3.2	Modeling and Simulations	42
3.3	Classical Molecular Dynamics	42
3.3.1	Interatomic Potentials	43
3.3.1.1	CHARMM force field	44
3.3.2	Numerical Algorithms	45
3.3.3	Thermodynamical Ensembles	45
3.3.4	Energy Minimization	46
3.3.5	Boundary conditions	46
3.3.6	Steered Molecular Dynamics	47
3.4	Parallel Computing	47
3.5	Post-processing Methods	48
3.6	Advantages and Limitations	48
3.7	Applications	49
3.8	Outline	50
	Bibliography	51
4	Atomistic Modeling of Collagen-Hydroxyapatite Nanocomposites	53
4.1	Introduction	53
4.2	Background	54
4.2.1	Collagen-Hydroxyapatite Nanocomposites	54
4.3	Materials and Methods	55
4.3.1	Atomistic Model	55
4.3.2	Crystal Geometry	56
4.3.3	Protein Model	56
4.3.4	Hydroxyapatite Force Field Parametrization	57
4.3.5	Steered Molecular Dynamics Simulations	57
4.3.6	Data Post-processing	58
4.4	Results	59
4.5	Remarks	62
	Bibliography	64
5	Fracture Mechanics of Hydroxyapatite Crystals	67
5.1	Introduction	67
5.2	Background	68
5.2.1	Hydroxyapatite	68
5.2.2	Geometric confinement	69
5.3	Materials and Methods	70
5.3.1	Atomistic Model	70
5.3.2	Crystal Geometry	71
5.3.3	Hydroxyapatite Force Field Parametrization	71

5.3.4	Molecular Dynamics Simulations	71
5.3.5	Data Post-processing	71
5.3.6	Stress Analysis	72
5.4	Results	72
5.5	Remarks	75
	Bibliography	78
 III Experimental analysis		81
6	Bio-inspired Composite: from Concept to Realization	83
6.1	Introduction	83
6.2	The Approach	83
6.3	Bone Model	84
6.3.1	Haversian System: Mechanical Properties	84
6.3.2	Haversian System: Toughening Mechanisms	85
6.4	Concept	87
6.5	Realization of the Bone-Inspired Material	88
6.5.1	Choice of Materials	90
6.5.1.1	Material for the Osteons	90
6.5.1.2	Material for the Internal Lamellae	90
6.5.1.3	Material for the Outer Lamellae	90
6.5.1.4	Materials for the Matrix	90
6.5.1.5	Materials for the Comparative Laminate	90
6.5.2	Manufacturing	91
6.5.2.1	Manufacturing of the Osteon Composite	91
6.5.2.2	Manufacturing of the Comparative Laminate	93
6.6	Remarks	94
	Bibliography	95
7	Experimental Characterization of the Bone-inspired Composite	97
7.1	Introduction	97
7.2	Experimental Testing	97
7.2.1	Tensile Tests	98
7.2.2	Compressive Tests	99
7.2.3	Flexural Bending Tests	100
7.2.4	Translaminar Fracture Toughness Tests	101
7.2.5	Interrupted Fracture Toughness Tests	102
7.2.6	Microscopic Analyses	103
7.3	Results	103
7.3.1	Tensile Tests	103
7.3.2	Compressive Tests	106
7.3.3	Flexural Bending Tests	108
7.3.4	Translaminar Fracture Toughness Tests	109
7.3.5	Interrupted Fracture Toughness Tests	112
7.3.6	Microscopic Analyses	113
7.4	Remarks	113
	Bibliography	118

IV	Conclusion	119
8	Conclusion	121
8.1	Remarks and Conclusions	121
8.2	Future Work	125
	Bibliography	127
V	Appendix	129
A	Sample Input Script for LAMMPS	131
B	Sample Script for Atom Definition in LAMMPS	133
C	Material Properties	137
C.1	Carbon Fiber Sleeves	137
C.2	Glass Fibers	137
C.3	Glass-Non-crimp Fabric	138
C.4	Carbon-Non-crimp Fabric	138
C.5	Resin	139
C.6	Hardner: RIMH 134	139
C.7	Hardner: RIMH 137	139

List of Figures

1.1	(a) SEM image of the structure of velcro, with tiny hooks and loops [6]. (b) A commercial application of velcro as a fastening device.	5
1.2	Scale structure of a Galapagos shark [6].	6
1.3	(a) Example of a gecko foot. (b) A new gecko-foot adhesive: the <i>Geckskin</i> (image via U.Mass Amherst).	7
1.4	(a) A mussel shell showing the nacre or mother-of-pearl layer. (b) SEM image showing the composite microstructure of nacre, adapted from [22].	8
1.5	Comparison between artificial and natural materials in terms of stiffness and toughness. (a) Stiffness and toughness values for biological materials. (b) Stiffness and toughness values for synthetic materials; the green region represents the region with the best combination in terms of stiffness and toughness, which may be reached by designing new bio-inspired materials (adapted from [7]).	9
1.6	Hierarchical structure of bone, showing 7 levels of hierarchy [7].	14
1.7	Structures of level 2 and level 5 of bone. (a) Level 2: staggered arrangement of collagen and HAP in mineralized collagen fibrils (adapted from [61]). (b) Level 5: schematic representation of the microstructure (<i>i.e.</i> Haversian system) of cortical bone (adapted from [40]).	15
2.1	Schematic of the classification of composite materials on the basis of the reinforcement type; schematic examples of structural composite (on the right).	27
2.2	Schematic representation of the Vacuum infusion process.	34
2.3	Comparison between the internal structure of wood and that of plywood. (a) Microstructure of wood, showing the primary and secondary layers in the tracheid and the pores aligned with the long axis in each cell (reproduced from [15]). (b) Structure of a commercial plywood.	36
3.1	(a) Atom point representation in classical molecular dynamics. (b) Schematic representation of the dynamics of the system, governed by the Newton's law; particle-particle interactions are highlighted with color dashed lines (different colors aims to show the different interaction forces depending on the bond type).	43
3.2	Schematic representation and mathematical formulation of each term included in the potential expression of the CHARMM force field (H-bonds are included in the vdW-terms) - adapted from [4].	45
3.3	Schematic example of the concept of periodic boundary conditions.	47
3.4	Different types of representation of a collagen fibril, plotted with VMD [14].	48
3.5	Simulation tools corresponding to different length- and- time scales [4].	49

4.1	Geometry and dimensions of the sandwich models used for steered molecular dynamics simulations.	55
4.2	Snapshot of the sandwich model, showing the basic structures of the collagen molecule and the HAP unit cell.	56
4.3	Simulation setup. (a) Simulation scheme followed for the initial case: boundary and loading conditions during the equilibrium and loading phase. (b) Simulation scheme followed for the confined case: boundary and loading conditions during the equilibrium, the confinement and the stretching phase.	58
4.4	Snapshots of the initial structure (left), after equilibrium, and the confined one (right), after "compression". The central snapshot represents the confinement phase: the HAP top layer before confinement is represented in gray color, whereas the same layer after confinement is shown in red color.	59
4.5	Snapshots showing various mechanisms of deformation during the tests. (a)-(b) Chain unfolding. (c)-(d) Hydrogen bond formation and breaking (in the first snapshot, panel (c), H-bond is highlighted with red lines; in the second snapshot corresponding to the following frame, panel (d), the previous H-bond is broken and a new one, highlighted with blue line, is formed. (e)-(f) Chain sliding and stretching.	60
4.6	Force-displacement. (a) Comparison between the vacuum and the solvated case: initial structure. (b) Comparison between the vacuum and the solvated case: confined structure.	61
4.7	Force-displacement. (a) Comparison between the initial structure and the confined one: vacuum case. (b) Comparison between the initial structure and the confined one: solvated case.	61
4.8	Number of hydrogen bonds during the tests. (a) Number of intramolecular H-bonds as a function of the displacement in dry condition for both initial and confined structures. (b) Number of intermolecular H-bonds as a function of the displacement in dry condition for both initial and confined structures. (c) Number of intramolecular H-bonds as a function of the displacement in solvated condition for both initial and confined structures. (b) Number of intermolecular H-bonds as a function of the displacement in solvated condition for both initial and confined structures.	63
5.1	VMD "atom representation" of Hydroxyapatite (HAP) unit cell. Each atom is represented with a different color: H (green), Ca (blue), O (red), P (gray). The HAP unit is highlighted with a dashed line; the size of H atoms is increased to make them visible and to show the alignment of OH groups along the <i>c</i> -direction. Both the crystal axes (<i>abc</i>) and the coordinate axes (<i>xyz</i>) are shown. (a) View parallel to the (001) plane. (b) Three-dimensional view of the model.	69
5.2	Geometry, dimensions and loading and boundary conditions of a cracked slab. (a) Model used for our atomistic study of fracture of HAP. Different samples are created by varying the sample height, ' <i>h</i> ', whereby the width, ' <i>w</i> ', and the crack length, ' <i>a</i> ', are fixed for all cases. The dimension ' <i>h</i> ' is considered as half of the height of the sample, excluding the fixed boundary regions (<i>i.e.</i> green-colored). The crack extends over half of the platelet width. (b) Snapshots of two samples.	70

- 5.3 Stress-strain plot of the tested samples. The stress is the longitudinal stress σ_{yy} (*i.e.* in the y -direction) and the strain represents the applied tensile strain in the y -direction. The initial slope of the stress-strain curve is not affected by the size of the sample, whilst the strength decreases by increasing the sample height. 73
- 5.4 Snapshots of the failure mechanisms of two different samples at different applied percent strain (numbers given in %): (a) sample with height $2h = 2.5$ nm; (b) sample with height $2h = 8.4$ nm. The smaller sample is characterized by a more distributed mode of failure with significantly larger strain levels, while in the latter a clear crack path can be recognized, with failure occurring at relatively small applied strains. 74
- 5.5 Stress-strain curve of two samples: (a) sample with height $2h = 2.5$ nm; (b) sample with height $2h = 8.4$ nm. Maps of the stress distribution for two cases: (c) sample with height $2h = 2.5$ nm; (d) sample with height $2h = 8.4$ nm. The maps show the stress field (in the middle section of each sample) at the critical strain ε^* , which is highlighted in the curves above. Also, the maximum stress (σ_{max}), reached before failure occurs, is highlighted in the two curves. 75
- 5.6 Stress field reaching from the crack tip to the far field for all samples shown in Table 5.1 and in Figure 5.3. The longitudinal stress field, averaged over a thin strip in the middle and over the entire thickness, is plotted against the x -direction (the zero x -coordinate represents the crack tip). The values on both the axes are normalized by the maximum values, respectively. The continuous lines represent power law fits to the atomistic data. 76
- 5.7 Normalized maximum strength over the normalized sample size. Comparisons with the Griffith theory prediction are given, showing a clear deviation at small length scales below the critical size $2h = 4.15$ nm. 76
- 5.8 Summary of the principal findings described in Chapter 5: flaw tolerance occurs below a certain critical size, which corresponds to the nanosize of HAP crystals in bone [5, 29, 41, 42]; HAP crystals fails in a non-brittle mode with large strain at failure and strength approaching the values of uncracked samples; the stress field, before critical crack propagation occurs, is homogeneous, showing no stress concentration at the tip of the crack. 77
- 6.1 Representation of the microstructure of bone: on the left, spongy bone; on the right, the complex microstructure of cortical bone, characterized by the repeating osteon unit. Adapted from [2]. 84

6.2	Toughening mechanisms in bone at different length scales in the 1-100 μm range [2]. (a) Crack deflection and twist: a crack, starting from a notch, encounters microcracks at the weak boundary of adjacent osteons (indicated with a black arrow); those microcracks cause energy dissipation and deviation of the growing crack from the direction of the maximum tensile stress, leading to an increase in toughness. (b) Constrained microcracking: effect of compression in the region around the main crack, preventing the crack to quickly propagate; such effect of compression is given by the presence of a large amount of small microcracks, which are naturally occurring in bone, allowing the remodeling process. (c) Uncracked-ligament bridging: an unbroken region, located between the growing crack a smaller crack, initiated ahead of it, can act as a bridge, increasing the toughness by carrying significant load. (d) Collagen fibril bridging: unbroken collagen fibrils act as a bridge between the two crack surfaces, preventing crack opening and growing.	86
6.3	Schematic representation of the osteon cylindrical structure and examples of crack propagation in cortical bone (image available from the University of Cambridge). (a) Osteon cylindrical structure: the red line represents the Haversian canal, the concentric lines the lamellae, and the outer line (grey) is the cement line. (b) Example of longitudinal crack propagation (blue) along the cement line of an osteon cylindrical structure. (c) Example of transversal crack propagation (blue) in an osteon cylindrical structure: initial propagation orthogonal to the osteon main axis, and deviation and splitting along the cement line.	87
6.4	Comparison between the structure of the osteon laminate and the microstructure of cortical bone. (a) Representation of the internal structure of the osteon laminate with the designed components. (b) Microstructure of the cortical bone; the most important structural components are color-highlighted. The color corresponds to the mimicked elements in (a).	89
6.5	Schematic axonometric view of the two realized materials: (a) the internal structure of the osteon laminate with the designed components; (b) the internal structure of a classical laminate with a typical lay-up.	89
6.6	Materials used as reinforcement for the osteon laminate and for the comparative laminate. (a) carbon fiber sleeve with a diameter of 5 mm, used to replicate the osteon. (b) UD-glass fibers used for internal part of the osteon and the interstitial regions. (c) NCF made of UD-GF used for the external surfaces of the osteon laminate. (d) NCF with orthogonally oriented CF used only for the comparative laminate.	91
6.7	Schematic representation of the microstructure of the bone-inspired composite used for the sizing of the fibers; A_1 , A_2 , and A_3 are the three areas to be fulfilled with UD-GF.	92
6.8	Schematic representation of the manual lamination process of the bio-inspired composite: (a) lamination and particular of the osteon-inspired tubular structure; (b) final internal structure before the impregnation process.	93
6.9	Schematic representation of the manual impregnation process of the bio-inspired composite: (a) resin impregnation with resin and hardener; (b) curing, (c) final product.	93

6.10	Schematic representation of the manual impregnation process of the comparative laminate: (a) resin impregnation with resin and hardener; (b) curing, (c) final product.	94
7.1	Draft showing the geometry of the specimens used for tensile and compressive tests.	98
7.2	(a) Experimental setup of a tensile test; the sample is clamped into the grips and an extensometer is placed. (b) Examples of specimens to be tested.	99
7.3	(a) Experimental setup of a compressive test with the sample clamped into the grips. (b) Samples to be tested.	100
7.4	Drawing of the three-point-bending configuration.	100
7.5	Three-point-bending tests: experimental setup. (a) Initial setup. (b) Final setup with two lateral supports to limit the transversal displacement of the load bearing rolls.	101
7.6	Drawing of the ESE(T) specimen for translaminal fracture toughness tests.	102
7.7	(a) Test arrangement for translaminal fracture toughness tests: load is applied through pin clevises and a displacement gage, mounted on knife edges, is used to measure the notch opening displacement (adapted from [4]). (b) Experimental setup of translaminal fracture toughness tests.	102
7.8	(a) Test arrangement for the interrupted translaminal fracture toughness tests: an optical microscope is placed in front of the specimen surface and connected to a computer to monitor the crack growth. (b) Image acquisition, during an interrupted translaminal fracture toughness test, with a computer connected to the optical microscope.	103
7.9	Comparison between the tensile behavior of the bio-inspired composite and that of the comparative laminate. (a) Stress-strain curve for the tensile tests on longitudinal configurations. (b) Stress-strain curve for the tensile tests on transversal configurations.	104
7.10	Longitudinal tensile tests: failure mode of the bio-inspired composite (a) and of the comparative laminate (b). Transversal tensile tests: failure mode of the bio-inspired composite (c) and of the comparative laminate (d).	105
7.11	Comparison between the compressive behavior of the bio-inspired composite and that of the comparative laminate. (a) Stress-strain curve for the compressive tests on longitudinal configurations. (b) Stress-strain curve for the compressive tests on transversal configurations.	106
7.12	Longitudinal compressive tests: failure mode of the bio-inspired composite (a) and of the comparative laminate (b). Transversal compressive tests: failure mode of the bio-inspired composite (c) and of the comparative laminate (d).	107
7.13	Comparison between the flexural behavior of the bio-inspired composite and that of the comparative laminate. (a) Stress-strain curve for the three-point bending tests on longitudinal configurations. (b) Stress-strain curve for the three-point bending tests on transversal configurations.	109
7.14	Longitudinal bending tests: failure mode of the bio-inspired composite (a) and of the comparative laminate (b). Transversal bending tests: failure mode of the bio-inspired composite (c) and of the comparative laminate (d).	110
7.15	Comparison between the fracture behavior of the bio-inspired composite and that of the comparative laminate. Force - Notch-mouth-displacement curves for both the materials.	110

7.16	Comparison between the fracture behavior of the bio-inspired composite and that of the comparative laminate; the red dashed lines show the cracks. (a) Failure of bio-inspired composite: crack splitting. (b) Failure of the comparative laminate: crack propagation and damaged area near crack tip region.	112
7.17	Pictures of the interrupted fracture toughness tests on the bio-inspired laminate. (a) Crack splitting during the test. (b) Failure.	113
7.18	Microscopic images showing the region near the crack tip, during the interrupted fracture toughness tests on the bio-inspired laminate. The red dashed lines in subfigures (a)-(e) show the cracks formation and propagation. The yellow dashed lines in subfigure (f) show the main cracks propagation, leading to splitting failure mode.	114
7.19	SEM images - with magnitude 40X and 100X - showing a cross-section of a specimen (bio-inspired material). (a) The image (from backscattered electrons) shows a region far from the crack propagation area. (b) The image (from backscattered electrons) shows the region where the main crack propagates; the crack region is highlighted with a dashed red line circle. (c) The image (from secondary electrons) shows the crack deviation, from the intra-osteon to the inter-osteon region. (d) The image (from backscattered electrons) shows the crack deviation, from the intra-osteon to the inter-osteon region; the crack path is highlighted with a red dashed line.	115
7.20	SEM images (from backscattered electrons) - with magnitude 40X and 100X - showing a cross-section, close to the cracked region, of a specimen (comparative laminate material). (a) The image, referred to the whole section, shows spread damages across the surface. (b) Union of two SEM images with an increased magnitude (100X).	116
8.1	Drawing of bone hierarchical structure [1] and scheme of the research approach followed in this study.	122
8.2	Comparison of the crack deflection mechanism in bone and in the bone-like material. (a) Crack deflection mechanism in bone: micrography and schematic [4]. (b) Crack deflection mechanism in the bone-like material: picture from the optical microscopy, during an interrupted fracture toughness test.	124
8.3	SEM images (from backscattered electrons) - with magnitude 40X and 100X - showing a cross-section of a specimen of the bone-inspired material. (a) The image shows the region where the main crack propagates; the crack region is highlighted with a dashed red line circle. (b)The image shows the crack deviation, from the intra-osteon to the inter-osteon region; the crack path is highlighted with a red dashed line.	124
8.4	Schematic solutions of the internal structure of the bone-inspired composite. (a) Initial solution object of the present study. (b) Alternative proposed solution: multi-layer osteon structure. (c) Alternative proposed solution: inter-osteon woven layer to improve the osteon-osteon interactions, limiting their slipping.	126
8.5	Schematic solution based on the results of atomistic simulations. (a) Representation of the osteon structure with improved adhesion at interface and platelet-like nanoparticles, inspired to the hydroxyapatite crystals. (b) Section of the osteon-like sleeve surrounded by platelet-like nanoparticles.	126

List of Tables

1.1	Literature survey of methods for determining the elastic properties of bone and corresponding values.	16
2.1	Typical properties of some commercial reinforcing fibers (adapted from [12]). . .	29
2.2	Typical properties of some commercial polymer resins (adapted from [11]). . .	31
4.1	Mechanical properties of collagen, HAP, and collagen-HAP nanocomposites from literature experiments and simulations.	55
4.2	Geometric and mechanical properties of HAP-collagen nanocomposites determined from the simulations described in Section 4.3.5.	59
5.1	Mechanical strength of the HAP samples compared to the effect of the sample height $2h$. The initial crack extends over half of the sample in the x -direction. The crack opening angle ($\alpha \approx 2^\circ$), the crack length ($a \approx 15.1$ nm), the sample width ($w \approx 30.1$ nm) and the sample thickness ($t \approx 2.1$ nm) are the same for all cases, and the sample height varies from 2.5 to 9.6 nm. The strength is determined as the maximum stress reached.	73
6.1	Literature survey of mechanical properties of the Haversian system. The values included in the third column are referred to longitudinal samples (first values) and to interchanging orientation of lamellae (second values).	85
6.2	Analysis of the osteon structure: definition of components along with structure and properties; definition of components to be mimicked in the osteon-like composite	88
6.3	Structural components chosen to be mimicked: design and simplifications. . . .	89
6.4	Technical specifications of the final bio-inspired composite plates (1-2-3) and the comparative laminates.	94
7.1	Nominal dimensions of specimens for tensile tests.	98
7.2	Nominal dimensions of specimens for compressive tests.	99
7.3	Nominal dimensions of specimens for three-point bending tests.	100
7.4	Results of tensile tests on the bio-inspired composite and on the comparative laminate, in both longitudinal and transversal directions.	105
7.5	Results of compressive tests on the bio-inspired composite and on the comparative laminate, in both longitudinal and transversal directions.	107
7.6	Results of three-point-bending tests on the bio-inspired composite and on the comparative laminate, in both longitudinal and transversal directions.	109

7.7	Results of the translaminar fracture toughness tests on the bio-inspired composite and on the comparative laminate.	111
7.8	Results of the experimental testing conducted on the bio-inspired composite and on the comparative laminate, in both longitudinal and transversal directions.	117
7.9	Final comparison between the bio-inspired composite and the comparative laminate, in both longitudinal and transversal directions.	117
8.1	Final comparison between the bio-inspired composite and the comparative laminate, in both longitudinal and transversal directions.	123

Part I

Introduction

Chapter 1

Biomimetics: learning from Nature

Biomimetics is an engineering design approach to create new structures, by reproducing characteristics found in nature. Indeed, in nature it is possible to find many smart solutions, which can be mimicked to build new materials, with potential applications to various engineering fields. This thesis work is focused on bio-inspired materials: the first part covers a deep study of bone structure, which provides the basis for the development of a bone-inspired design. The second part deals with numerical modeling of bone, from an atomistic point of view, by means of a molecular dynamics approach. In the third part, a new bone-inspired materials is presented, from its first concept to the final design and realization; an experimental characterization of the material follows. The last part contains a critical discussion of the obtained results and introduces new perspectives on future work.

1.1 Introduction

Nature has developed materials, objects and structures with multiscale functions and adaptation, from the macroscale to the nanoscale. By quoting J. Aizenberg, a pioneer in the rapidly developing field of bio-inspired materials science and engineering:

"Stealing from nature is a very rewarding business."

Indeed nature has a lot of beautiful technological solutions, with the advantage of not being protected by intellectual property. Therefore, it is possible to find something amazing in nature, and try to understand the mechanisms behind the smart natural systems to mimic them.

Biological materials are highly organized at different scale levels, from the nano to the macroscale, often in a hierarchical manner with intricate nanoarchitecture, enabling multifunction and adaptation characteristics [1–7]. Nature uses commonly found materials, whose properties result from an interaction between the structure-level organization and the physical and chemical properties. Examples found in nature that are of commercial interest are molecular-scale devices, superhydrophobicity, self-cleaning, drag reduction surface in fluid flow, energy conversion and conservation, high and reversible adhesion, aerodynamic lift, materials and fibers with high mechanical strength, biological self-assembly, antireflection, structural coloration, thermal insulation, self-healing materials [6–14].

Mimicking natural structures does not mean to create a mere copy of those, such as synthetic materials. But, by observing a smart system, it is possible to get inspired by that, ending up with a new material with novel properties. Nature makes a great job in designing and manufacturing materials and systems. However, man can observe nature and try not to simply copy the natural

materials, but combine them to create smarter systems, to solve different kinds of engineering problems. An example is plywood, a wood-like composite designed to overcome the major drawbacks of natural wood (*e.g.* the limited transversal size and the marked anisotropy).

The interest of biomimetics is to examine biological phenomenology with the hope of gaining insight and inspiration for developing physical or composite bio-physical systems in the image of life. Therefore nature is considered as a 'model', a 'measure' or a 'mentor' in the bio-inspired design. The biomimetic approach has led, in the past, to different solutions, either by creating a copy of natural structures (in terms of shape and functions) or by choosing specific functions of some natural organisms to be replicated in artificial systems, providing innovative technological solutions.

1.2 The History of Biomimetics

The name *biomimetics*, derived from the Greek word *biomimesis*, was coined by Otto Schmitt in the 1960s to transfer ideas from biology to technology. In the past 50 years it has led to many discoveries, successful devices and innovative materials, becoming a real branch of science, though purely empirical. A first idea of Biomimetics appeared in 1957, with the name of biophysics. According to Schmitt, *biophysics* is a point of view, an approach to solve problems of biological science, by using the theory and technology of physical sciences. Later, in 1969 he labeled this concept with the word *biomimetics*, which appeared for the first time in the title of a paper [8], then in the Webster's Dictionary in 1974 with the following definition:

The study of the formation, structure, or function of biologically produced substances and materials (as enzymes or silk) and biological mechanisms and processes (as protein synthesis or photosynthesis) especially for the purpose of synthesizing similar products by artificial mechanisms which mimic natural ones.

Biomimetics, which is also considered as synonymous of 'biomimesis', 'biomimicry', 'bionics', 'biognosis', 'biologically inspired design', has the meaning of copying, adaptation or derivation from biology. Started as an approach to problem solving, today it has become an empirical and inter-disciplinary branch of science, which aims to solve problems arisen in engineering, chemistry or design, by getting inspired by nature.

Historically we have many examples of biomimetic approach. For instance, Leonardo Da Vinci, who studied - in the late 1511 - birds flights and designed machines to reproduce this characteristic found in nature. Indeed, according to Leonardo da Vinci, in order to copy nature we have to understand the reasons behind such smart systems, by looking at experience and try to learn from it:

"Although nature commences with reason and ends in experience it is necessary for us to do the opposite, that is to commence with experience and from this to proceed to investigate the reason."

In the past 50 years, biomimetics has led to many innovative inventions and solutions. *Velcro*, the brainchild of a Swiss engineer, George de Mestral, derived from the action of the hooked seeds of the burdock plant, which caught in the coat his dog when they were out on a walk. By observing this phenomenon with a microscope, he realized that the hooking system consisted in the tiny crochet-like ends of the burdock burrs, that could easily bind to most organic textures. He saw a great potential in this simple fastening device and he proposed it as an alternative to the zip fastener. De Mestral reproduced the natural attachment with two strips of fabric, one

with thousands of tiny hooks and another with thousands of tiny loops and he named his invention Velcro, a combination of the words 'velvet' and 'crochet', and formally patented it in 1955 [15]. The structure and the most common application of velcro are shown in Figure 1.1.

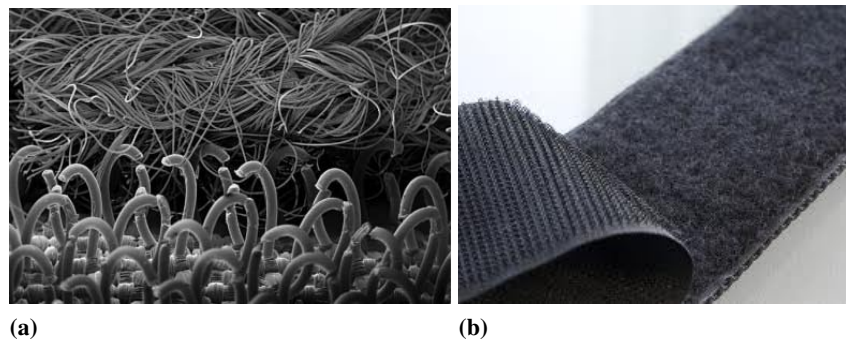


Figure 1.1: (a) SEM image of the structure of velcro, with tiny hooks and loops [6]. (b) A commercial application of velcro as a fastening device.

Another bio-inspired invention, dated to the mid 80s, is a coating able to indicate the impact damage, by means of a paint mixed with microcapsules (1-10 mm in size) and a certain chemical reagent. This invention was inspired to the human skin, which is sensitive to impact, leading to purple marks in the hit areas [16]. This coating was used in the aircraft industry to identify damage to components made of composite materials. Indeed, these materials are generally impact-sensitive, experiencing a significant loss in strength, without visible structural damage; hence, the change of color of the coating can give an indication of a damage, potentially dangerous for the aircraft.

A recent example of bio-inspired design is the new swim suit, the Fastskin bodysuit, designed by Speedo[®] and made of a new fabric, which mimics the shark scales, previously observed by means of a microscope. The new textile, made of a polyurethane woven fabric with a texture based on shark scales, allows the friction to be reduced and the water flow to be increased, making it suitable to improve the agonistic performance [6, 9], as resulted by all the records broken in the 2008 Olympic games. Also boat, ship and aircraft manufacturers are trying to mimic shark skin to reduce friction drag and minimize the attachment of organisms on their bodies. For instance, to reduce friction drag, transparent sheets with a ribbed structure in the longitudinal direction have been used on the commercial Airbus 340 aircraft [6]. An example of the structure of the shark scale under microscope is shown in Figure 1.2.

Another great invention is the gecko foot dry adhesive, based on the idea of mimicking the gecko skin, which can generate high dry adhesion. The gecko skin has a complex hierarchical structure, consisting of lamellae, setae, branches and spatulae [6]. At the larger level there are the lamellae soft ridges (1-2 mm long), located on the attachment pads (toes) that easily compress, to allow contact with rough bumpy surfaces. An extension of lamellae are the setae, which appear as tiny curved hairs, 30-130 μm long. Each seta terminates with 100-1000 spatulae, which represent the points of contact with the surface. This three-level hierarchical structure allows adaptability to surfaces with different magnitudes of roughness; then, to unstick itself, the gecko uses a peeling action. The problem of gecko-like adhesives has been studied for years, intriguing many scientists. Different biomimetic solutions have been developed; the last one, known as *Geckskin* in May 2012, by researchers of UMass Amherst [13], has revealed

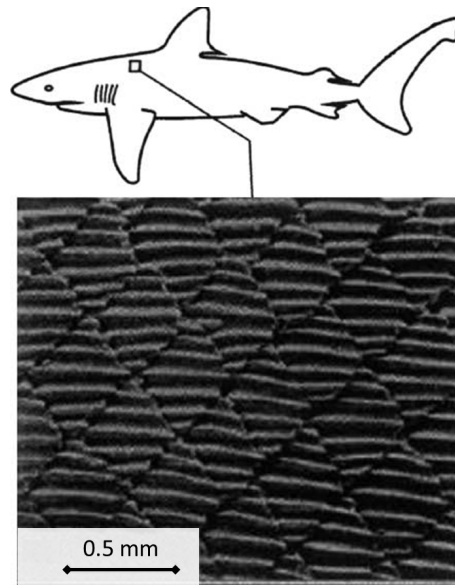


Figure 1.2: Scale structure of a Galapagos shark [6].

to be a great success, since unprecedented force capacities have been reached, through an integrated design with inextensible draping fabrics, inspired by the skin-tendon morphologies found in the Tokay Gecko. Figure 1.3 shows an example of a gecko foot and of the above mentioned *Geckskin*.

Beyond the above described examples of biomimetic solutions, there are many other bio-inspired solutions developed in the last decades, and the number is ever increasing, with the success of the emerging field of biomimetics. Most of the commercial biomimetics applications include new nanomaterials, nanodevices and processes. Hence, the rising trend towards miniaturization and the ever-increasing use of nanotechnology, whereby it is possible to reproduce tiny materials and surface patterns, has opened new frontiers of science to bio-inspired nanomaterials, able to reproduce nanopatterns characteristics of the small level structures of biological materials.

1.3 Biomimetic Approach

Nature develops biological objects by means of controlled growth (*e.g.* mineralization in bone). Generally this process can be seen as a self-assembly, resulting in hierarchical structuring at all levels in order to adapt form and structure to the function [4, 6]. This self-assembly hierarchical organization with multi-scale dimensions of features, ranging from the macroscale to the nanoscale, are extremely common in nature and provide interesting properties, in terms of adaptation.

It is apparent that nature uses hierarchical structures, mostly consisting of nanostructures, to achieve the required performance needed for a specific function [6]. Understanding the role of hierarchical structure and development of low cost and flexible fabrication techniques would facilitate commercial applications. Since the properties of those materials and surfaces result from a complex interplay between surface morphology and physical and chemical characteristics at different levels, an interdisciplinary and multi-scale approach like the biomimetic is needed, to get a deep understanding of biological hierarchical materials. To mimic interesting

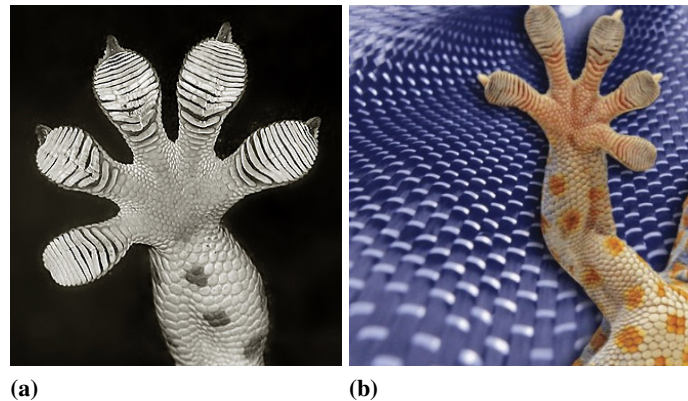


Figure 1.3: (a) Example of a gecko foot. (b) A new gecko-foot adhesive: the Geckskin (image via U.Mass Amherst).

hierarchy-induced properties found in nature, biomimetic materials research follows either a *top-down* or a *bottom-up* approach, allowing all the scale levels to be investigated [17].

Top-down approach. Engineers work together with biologists to observe nature, identify the most promising solutions with additional structural and functional analyses, then deduce the functional principles, and create a modified and appropriate technical solution. Finally they look for an optimal translation into techniques with the appropriate manufacturing methods and materials. This strategy is also used for the optimization of existing biomimetic systems.

Bottom-up approach. Engineers follow the research of biologists, who look into nature's structures, processes, and functional modes of operations; then work together to abstract insight from nature and use them for the design of new technical solutions and new bio-inspired materials.

The former is an approach of problem solving, the latter is a creative approach, which leads to the design of innovative bio-inspired solutions. A bottom-up approach allows one to get a deep understanding of materials and processes, started from a description of its small units, or building blocks. This approach is followed: *i*) experimentally, by means of structural and mechanical nanotechniques, such as microscopy (*e.g.* TEM, SEM, AFM, LM, confocal laser-microscopy), micro-tomography, synchrotron X-ray diffraction, Raman-spectroscopy, nanoindentation, micro- nano- and cell-mechanical testing; *ii*) numerically, by means of computational methods and techniques operating at the atomistic scale. For instance, atomistic modeling providing a fundamental description of materials behavior. This is an interdisciplinary approach, allowing to get an insight into the material behavior, finding a connection among physical, chemical, and mechanical properties of small scale systems. This method, used in this thesis work to study the building blocks of bone, is described in Chapter 3.

1.4 Biological Materials and Bio-inspired Materials

Most of biological materials are composites with a hierarchical structure. Among the large variety of composite materials offered by nature, wood, nacre, and bone are considered very in-

teresting structural materials for their great combination of mechanical properties, and they are often object of study to get inspiration for the design of new materials. Except for wood, which is predominantly a polymer composite made of cellulose fibers in a lignin matrix, the other two are organic-inorganic composites, consisting of hard ceramic reinforcing phases embedded into natural organic polymer matrices [18]. The latter biocomposites, also known as bone-like materials or biominerals, are characterized by an intricate hierarchical structure, consisting of a highly controlled organization at different levels, with characteristic structural dimensions at each level, ranging from the nanometer to the macroscopic length scale. This results in a complex architecture, which provides the material with multifunctional properties. The controlled growth and the specific size of the components of the biocomposites, resulting from the biomineralization process, play a crucial role in determining the mechanical performance of the whole composite; thus, there is an increasing interest among researchers to understand the mechanisms behind the controlled biomineralization.

Among biominerals, an interesting material that is recently object of large study, is nacre, also known as mother of pearl. Nacre is strong, iridescent with changeable colors, used for decorative purposes; it is found in nature as the thick inner layer of the seashells. Seashells are biominerals, which appear as natural nanocomposites with a laminated structure. As artificial composites, they exhibit superior mechanical properties to their constituents [6, 7, 19–21]. This is also due to the organic-inorganic nature of this material, where the inorganic mineral part provides the strength, and the organic part provides the ductility. Seashells are composed of a large fraction of inorganic minerals (typically calcium carbonate, calcium phosphate and amorphous silica with a concentration of the order of 95 %) and a small amount of organic biopolymers (typically keratin, collagen and chitin in the range of 1–5 %). This mixture of brittle platelets and thin layers of elastic biopolymers provides the material with strength and toughness, inhibiting transverse crack propagation. The multiple length sizes further increase its toughness, making it equivalent to silicon [6]. Figure 1.4 shows a mussel shell with the nacre layer and the composite microstructure of nacre.

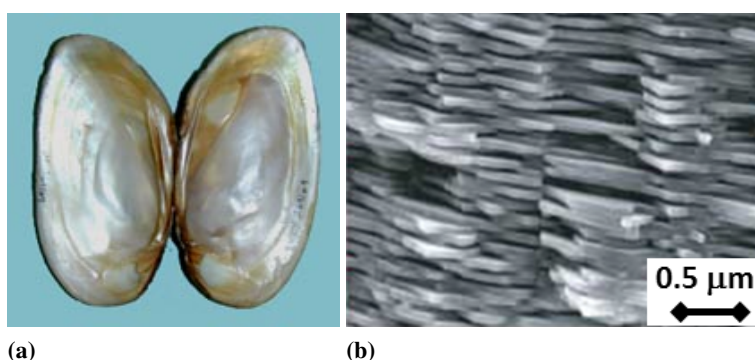
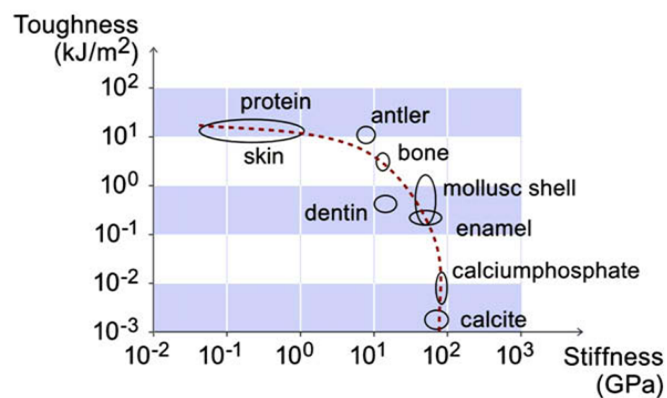


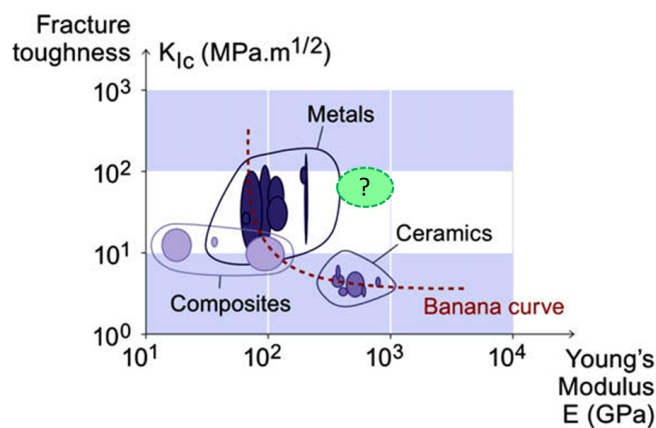
Figure 1.4: (a) A mussel shell showing the nacre or mother-of-pearl layer. (b) SEM image showing the composite microstructure of nacre, adapted from [22].

Among those biocomposites, an intriguing material is the human bone, a composite of collagen and hydroxyapatite. Bone is considered as a biomineral, due to the high content of calcium-phosphate minerals, which make it hard and stiff. However, a common characteristic of bone is the incredible toughness, in spite of its brittle mineral components [3, 23–27]; in fact, bone toughness is about three to five orders of magnitude more than that of the mineral

it is made of. Until now, no conventional man-made composite material has reached such an amplification in toughness, compared to the raw components (see Figure 1.5); for this reason bone is considered as a biomimetic model material. The reasons of the toughness and ductility of this materials have to be seek in the hierarchical organization. The key mechanisms, which make it a quasi-ductile and damage-tolerant material, with an increased toughness, are different and act at various length scales. The simultaneous operation of toughening mechanisms, acting at different length scales, provides the bone with its enduring strength and toughness. Hence, to understand the effects of the hierarchy on the mechanical response of bone, and the structure-property relationship, it is worthwhile to perform a multi-scale study, with a bottom-up approach, starting from a fundamental description of the material. Various microstructural



(a)



(b)

Figure 1.5: Comparison between artificial and natural materials in terms of stiffness and toughness. (a) Stiffness and toughness values for biological materials. (b) Stiffness and toughness values for synthetic materials; the green region represents the region with the best combination in terms of stiffness and toughness, which may be reached by designing new bio-inspired materials (adapted from [7]).

aspects of bone and bone-like materials have provided inspiration for the design of new biomaterials, but also bio-inspired materials. Then, investigations of the individual aspects, related to the microstructure and the length scale, and the resulting properties have led to the improvement of existing biomaterials and to the design of new biomaterials and bio-inspired materials [18].

Being this thesis project focused on the study of human bone and on the development of a bone-inspired material, we provide a more detailed description of bone structure and properties in Section 1.5.

1.5 Bone

Bone is one of the most intriguing materials found in nature. It is an important structural component of the human body and the primary structural element of the skeletal system, providing support to many organisms. In bone family it is possible to recognize different types of structures, intended for diverse functions: long bones, such as femur or tibia, provide stability against bending and buckling, whereas short bones, such as vertebrae, are intended to support compression loads; the plate-like bone, as those forming the skull, ensures protection for organisms instead.

The exceptional combination of strength and stiffness with a low weight, makes it an outstanding material, where its behavior is mainly due to its composite structure. In fact, from an engineering point of view, bone can be considered a composite material, consisting of an inorganic (mineral) phase and an organic phase, which are intricately organized on different scales, allowing a multitude of functions under the various loading conditions, experienced during the daily activities. Like all natural materials, the mechanical properties of bone are determined by its structures, which are in turn inspired by its principal mechanical functions [4, 25, 28, 29].

What makes bone a unique material is its living, growing and dynamical structure, able to self-repair, regenerate and adapt its architecture, to maintain the mechanical properties and continue providing its functions. This is due to the combined activity of specialized cells, in particular the osteoclasts and the osteoblasts. Of particular interest are two characteristics of bone, the remodeling and the adaptation. Bone remodeling is ensured by the simultaneous activity of osteoclasts and osteoblasts. The former control the bone resorption, by digesting aged or damaged bone; the latter, instead, are responsible of the formation of new bone tissue, in order to replace the damaged one, caused by ageing or fracture. In normal physiological conditions, this continuous cellular activity is coordinated, so as to keep constant the bone mass and strength, ensuring the bone load-bearing capacity. During normal physiology, bone cells can also repair fractures that occur [30]. In this case, the remodeling process, also known as fracture healing, primarily depends on the mechanical forces applied to bone [29, 31]. Bone adaptation also occurs as a response to mechanical stimuli, where continuous variations of bone mass and architecture follow changing mechanical environments. The fundamental rules, governing bone adaptation, are three: *i*) the stimulus given by dynamic loads, *ii*) a short duration of mechanical loading necessary to initiate the adaptive response, and *iii*) the capacity of bone cells to accommodate to a regular mechanical loading environment, becoming less responsive to repetitive loading signals [32].

The complex architecture of bone strongly affects its mechanical response, with different effects at each length scale, from the sub-nanoscale to the macroscale. The study of structure-property relationship is crucial in order to get a deep understanding of the material behavior, with the aim of replicating the structure and properties in the design of new biomaterials, or mimicking part of its complex architecture in the design of new bio-inspired materials.

The following sections provide a detailed description of the structure and the properties of bone. Section 1.5.1 contains a description of the composition of bone, along with its basic features. Section 1.5.2 discusses the fascinating process of bone formation. In Section 1.5.3 we describe the bone hierarchical structure, level by level, whereas Section 1.5.4 focuses on the

mechanical properties of bone. Finally Section 1.5.5 is dedicated to a critical issue concerning bone, the effect of aging and disease, with a special focus on *Osteogenesis Imperfecta Disease*, a genetic disorder, which causes weak and fragile bones.

1.5.1 Bone Composition

Bone can be considered, as a first approximation, a ceramic-polymer composite consisting of collagenous matrix, reinforced with calcium-phosphate platelets. The former represents approximately the 35% of the total mass of bone and consists of collagen fibers (90%), noncollagenous proteins (NPCs), water lipids, and cells. The latter, which constitutes approximately the 25% of the total volume of bone and the 50% of its mass, is a mineral phase, mainly composed of calcium and phosphorus in the form of hydroxyapatite (HAP) crystals. The structure and the mechanical properties of bone depend on the characteristics of each phase, on the structural organization and on the physical interactions between them [29].

Collagen and HAP are considered the basic building blocks of bone. HAP, the brittle and stiff part, is mainly responsible for carrying out the load, providing stiffness and strength; the collagen fibers instead, confers flexibility to bone, and the possibility of dissipating energy under large deformation. A brief description of bone basic building block follows (Section 1.5.1.1-1.5.1.2).

1.5.1.1 Collagen

Collagen is a ubiquitous protein, which constitutes the fundamental matrix of all connective tissues. More than 27 different types of collagen are present in biological tissues, though the most abundant one are two: *i*) collagen type I, which is present in the extracellular matrix of various tissues, such as tendons, ligaments, bone, dentine, skin, blood vessels, and muscles; *ii*) collagen type II, which is an important component of soft tissues, such as articular cartilage and cornea. Collagen type I provides the tissues with different mechanical functions: in tendons and ligaments it transmits the force from muscles to bone and stores elastic energy, in bones and dentine it provides yielding and toughness properties, in muscles ensures the contractile functions [33].

Collagen, like all natural materials, has a hierarchical structure, which confers a large versatility on it, with capability of adaptation to different functions, resulting in a large variety of properties. The tropocollagen unit is the basic structural unit of collagen and consists of three polypeptide strands (α -chains), right-end twisted together to form a coil known as triple helix, stabilized by H-bonds between different residues [34]. It is also characterized by a repeating amino acid sequence consisting of glycine molecules (GLY), every third residue, and amino acids (*e.g.* proline and hydroxyproline). Triple-helical collagen molecule are generally 1.5 nm in diameter and 300 nm long, and have short non-helical regions, called telopeptides at each end, known as amino (N) and carboxyl (C) telopeptides, to facilitate later assembly into fibrils. Intermolecular cross-links are formed between the helical and non-helical domains of adjacent collagen molecules, which are then staggered to each other in the fibrillar configuration, and stabilized by covalent cross-links and hydrogen bonds between neighboring molecules. Depending on the collagen type, the triple helix can be homotrimeric, consisting of three identical α -chains (*e.g.* type III collagen), or heterotrimeric, where at least one of the polypeptides is not identical to the others (*e.g.* type I collagen). The predominant form of collagen in bone is type I collagen ($[\alpha 1(\text{I})]_2\alpha 2(\text{I})$); however type II or III ($[\alpha 2(\text{I})]_3$) is also present, in case of genetic disease (*e.g.* Osteogenesis Imperfecta) [33]. The homotrimer form generally character-

izes pathological conditions, though it is also found in physiological conditions in dentine and dermis [35].

1.5.1.2 Hydroxyapatite

Hydroxyapatite (HAP) is the principal component of biomineralized hard tissues, as dentine, enamel and bone, and it is considered, together with the collagen molecules, the fundamental building block of bone, universally present in all bony tissues [7, 24, 25, 36–38]. It strongly affects the properties of bone in terms of stiffness and strength, carrying most of the tensile load. Hydroxyapatite belongs to the family of apatite, calcium-phosphate compounds ($\text{Ca}_5(\text{PO}_4)_3\text{X}$), existent in nature in several different forms, depending on the replacing anion (X), which can be fluorine, chlorine, or hydroxide. The latter is the case of bone [39]. Compared to the calcium phosphate called hydroxyapatite, bone mineral contains various impurities. In particular, it contains about 4–6% of carbonate replacing the phosphate groups, making the mineral more similar to a carbonate apatite (dahllite). The overall shape of the mineral platelets is usually not known, also because it is different depending on bone types. Regarding the size, those crystals are generally tens of nm wide and long, and about 2–4 nm thick [25, 40]. The small size in one direction may have, as we will see in Chapter 5, interesting mechanical implications.

Still object of debate among researchers is how the minerals interact with the collagen; the interactions between the basic building blocks are thought to have a large effect on the mechanical behavior of the bone tissue at nanometer level and are currently object of study [41–48]. A more detailed description of HAP is given in Chapter 5, whereas Chapter 4 discusses the interactions between collagen and hydroxyapatite, and the mechanical behavior of their nanocomposites.

1.5.2 Biomineralization

The process by which living forms precipitates mineral materials is known as mineralization or biomineralization, when it involves biological tissues. This process consists in the nucleation of mineral components, starting at the organic phase, followed by their growing until a specific size has reached, and results in biomineralized inorganic/organic composite [49–51].

Biomineralization is also the process responsible of bone formation, which occurs by precipitation of HAP mineral crystals, within (intrafibrillar HAP) and between (extrafibrillar HAP) the collagen fibrils. Collagen fibers (CFs) are generally aligned and organized in a staggered configuration, with gap regions; these are filled up by HAP at the end of the biomineralization process, leading to the formation of mineralized collagen fibers (MCFs), which combine with the extracellular matrix (ECM) to form the mineralized tissue [33, 52, 53]. These structures, found at small scale, are considered as the main building blocks of bone, and are found universally among the organisms, maintaining their organization, whereas the bone structure at larger scales shows a wide variety among the organisms and tissues [43, 54]. A schematic representation of the staggered arrangement of collagen and HAP in mineralized fibrils is given in Figure 1.7a.

It has been demonstrated, in experimental studies, that the interaction between the organic matrix and the mineral crystals controls the growth process of HAP in bone, determining the final morphology of the mineral platelets [55–57]. Though researchers agree to that the mineral-matrix interactions play a crucial role in controlling the biomineralization, the mechanism behind that, is still unknown. Also, it is not yet possible to study, by experiments alone, the mechanism and fast reactions involved in the biomineralization process; hence, to overcome

these problems, different simulation techniques have been developed and applied to a wide range of problems in biomolecular science [48,58,59].

1.5.3 The Hierarchical Structure of Bone

Bone, as most of the natural materials, shows a complex hierarchical structure, which consists of different organization levels, ranging from the atomistic to the macroscale, with adaptation to local needs and functions. Each level is characterized by its building blocks, and a specific organization between them, optimized to meet specific functions. The resulting properties of the bone composite systems are far superior than those of the individual building blocks.

The structure of bone can be described as a 7-level hierarchy, as shown in Figure 1.6:

Level 0. This is the ultrastructural level, characterized by the basic units of the fundamental building blocks of bone, collagen and HAP. As described above (in Section 1.5.1), the tropocollagen molecule consists in a triple helical arrangement of collagen fibers, which are made of a sequence of amino-acids in polypeptide chains, the non-collagenous proteins, which are made of amorphous ground substances, and the HAP is a calcium-phosphate mineral crystal, with a hexagonal (HCP) lattice.

Level 1. The collagen protein filaments and the HAP mineral crystals are the main components of level 1. These two components, together with a small amount of non-collagenous protein and water, form the basic structural units of bone.

Level 2. At larger length-scale ($\sim 1 \mu\text{m}$) tropocollagen molecules assemble in a hydrated environment, to form bundles called collagen fibrils, also including non collagenous proteins; the collagen fibrils (CFs) are then organized in a staggered configuration. This arrangement shows some gap regions, which are filled by HAP crystals during bone formation, resulting in mineralized collagen fibrils (MCFs). The latter are highly conserved building blocks of bone, universally present in all bony tissues.

Level 3. This level ($\sim 10 \mu\text{m}$) is characterized by fibrils arrays, where fibrils are held together by a protein phase, with additional dissipative functions.

Level 4. It is possible to recognize different fibril array patterns ($\sim 50 \mu\text{m}$), with parallel, random, woven, or tilted orientations. At the upper level, the fibril arrays, with their characteristic patterns, form the lamellae (between $3\text{-}7 \mu\text{m}$ thick).

Level 5. This microstructural level is characterized by the typical cylindrical structure (with a diameter up to $200\text{-}300 \mu\text{m}$ and a length of $1\text{-}2 \text{ cm}$), called *osteons* or *Haversian systems*, made of a concentric lamellar structure and an internal vascular canal ($\sim 50\text{-}90 \mu\text{m}$ in diameter). Beside the concentric lamellae, there are also interstitial lamellae, placed in between different osteons. The outer boundaries of osteons are then surrounded by the so-called "cement lines", about $1\text{-}5 \mu\text{m}$ thick, resulting from a remodeling process.

Level 6. At this level the structure is not highly conserved as at the nanostructural level, but starts to differentiate, in trabecular (also known as spongy or cancellous) and cortical (or compact) bone. The two bone types show different structures (*i.e.* higher porosity in spongy bone), and consequently different mechanical properties, since they are intended to meet different functions.

Level 7. This large-scale level show the overall structural shape of bone.

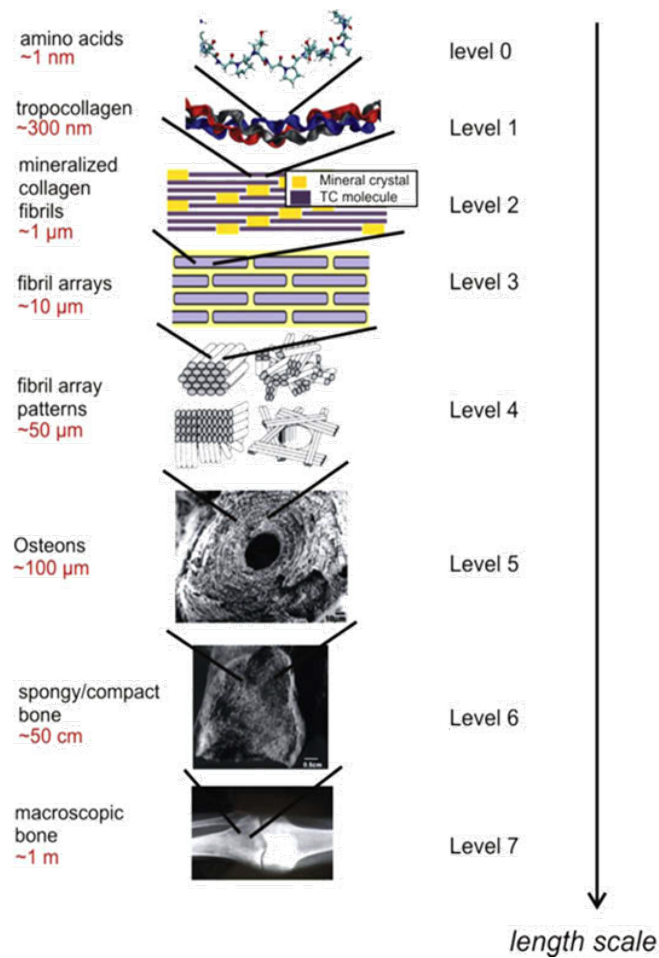


Figure 1.6: Hierarchical structure of bone, showing 7 levels of hierarchy [7].

Cortical bone can also show a woven-fibered structure. In this case, it is known as woven cortical bone, and is the only type of bony tissue which can be formed *ex novo*. It is often found in young growing skeletons (under the age of 5), but it can also be found in adult skeletons in cases of trauma or disease, forming around bone fracture sites. Woven bone is essentially an SOS response by the body to place a mechanically stiff structure within a needy area in a relatively short period of time. For this reasons it is the most disorganized type of bone tissue, without an osteon structural organization, nor a lamellar one [60]. Figure 1.7 schematically shows the two hierarchical levels that are object of this study, the nanoscale and the microscale levels.

1.5.4 Mechanical Properties of Bone

Bone is an incredible material, with a low density and a great combination of mechanical properties, which are not possible to be found in a unique conventional material. Although made of weak and brittle constituent materials, bone results in a very strong material with an excellent resistance to fracture, as shown by Ritchie *et al.* [23–26]. Indeed, among the most fascinating properties of bone is its toughness, which results from the combination of different mechanisms, acting at different organization levels. Many factors, such as the hierarchical organization of bone, the characteristic size of its building blocks, the porosity are considered to affect the bone

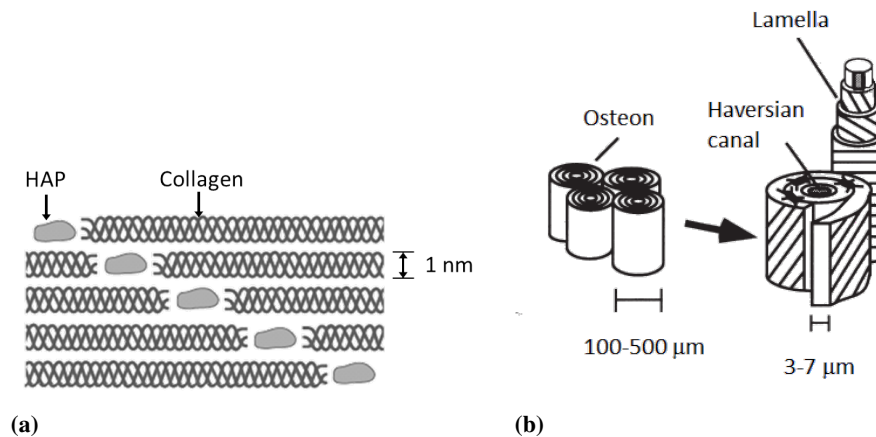


Figure 1.7: Structures of level 2 and level 5 of bone. (a) Level 2: staggered arrangement of collagen and HAP in mineralized collagen fibrils (adapted from [61]). (b) Level 5: schematic representation of the microstructure (i.e. Haversian system) of cortical bone (adapted from [40]).

toughness. The discussion about the origin and the mechanisms of toughness in bone is covered in Chapter 6, providing a direct link with the description of the design of a new biomimetic material. An indication of bone toughness and stiffness is given in Figure 1.5, providing also a direct comparison with artificial and natural materials (in terms of stiffness and toughness).

The bone behavior greatly varies according to the length scale at which it is assessed, depending on the characteristic structure of the corresponding hierarchical level. For this reason, a multi-scale approach has been widely used to investigate the mechanical properties of bone at different length scales, getting a fundamental understanding of its behavior. Thanks to a multi-scale study, now it is possible to distinguish the whole bone mechanical behavior, typical of the macroscale structures, from the tissue-level mechanical behavior, typical of smaller scales, from the micrometer to the atomistic scale. While the large scale behavior can be experimentally determined, for the small scale tissues it is not always possible to perform experimental testing, especially at sub-nanoscale levels. In these cases, simulation techniques are revealed to be a powerful tool to assess the mechanical performance of the bone building blocks, getting an insight into the structure-property relationship. At each scale, bone can be considered as an anisotropic, heterogeneous, nonlinear material. The mechanical response and the failure mechanisms of bone are strongly influenced by the mechanical behavior of the constituents at the nanoscale. In particular, the mechanical properties of the bone building blocks, and their interactions play a crucial role in determining the overall mechanical performance of bone [7, 24, 25, 40, 62–64]. At larger scales, the properties of bone depend on a large extent on the density. Indeed, the density of bone varies with the position in the body. Generally, the trabecular one is among the most porous type in the body, whereas the cortical one has the highest density [25, 40, 65–67]. A literature survey on the elastic properties of bone is given in Table 1.1. To describe bone at a large level (e.g. level 6) two parameters are commonly used: the bone quality and the bone quantity. The former is a loosely defined parameter to describe the microstructure of the bone matrix, such as stiffness, strength, and toughness. Bone quantity instead, is a largely used parameter, known with the acronym BMD (bone mass density or

Table 1.1: Literature survey of methods for determining the elastic properties of bone and corresponding values.

Study	Property	Value [GPa]	Test method	Bone type
McNamara <i>et al.</i> [68]	Elastic modulus	2.81 ± 2.09	Tensile	Trabecular (Rat proximal tibia)
Townsend <i>et al.</i> [69]	Elastic modulus	14.1 (dry) 11.3 (wet)	Compression	Trabecular (Human patella)
Runkle and Pugh [70]	Elastic modulus	8.69 ± 3.17	Buckling	Trabecular (Human subchondral bone)
Ashman and Rho [71]	Elastic modulus	13.00 ± 1.47	Ultrasound	Trabecular (Human distal femur)
Mente and Lewis [72]	Elastic modulus	7.8 ± 5.4 (dry)	Cantilever beam	Trabecular (Human femur)
Choi <i>et al.</i> [67]	Elastic modulus	5.44	Three-point bending	Trabecular (Proximal tibia)
Turner <i>et al.</i> [66]	Elastic modulus	18.14 ± 1.70	Nanoindentation	Trabecular (femur)
Rho <i>et al.</i> [65]	Elastic modulus	17.50 ± 1.12	Acoustic-microscopy	Trabecular (Human vertebrae - transversal direction) Cortical (Tibia-longitudinal direction)
		13.5 ± 2.0	Nanoindentation	
		22.5 ± 1.3		

bone mineral density), and defined as the amount of bone mineral per cross sectional area. This parameter is mainly related to the fracture behavior, and to problems arising with the age (*i.e.* osteoporosis or aging-related diseases are connected to a bone mass loss, which is in turn related to an increased fracture risk) [25]. Nevertheless, BMD is not the unique cause of aging-induced fracture risk; also, being the fracture risk a common problem among elderly, there has been recently a renewed and increasing interest in studying the mechanical properties of bone, to better understand the mechanisms behind the aging-related fracture risks and provide a method to predict the risk of bone fracture.

1.5.5 Aging and Disease

An important aspect of bone is the effect of aging and disease on its properties, being bone the main component of the human skeleton. Aging and disease introduce changes in the collagen and HAP structures, with consequences on the mechanical behavior of bone tissues at all levels. Generally aging-related changes in bone tissue tends to deteriorate bone, causing a loss of bone mass (*Osteoporosis*), thus the risk of fracture. Indeed it has been experimentally demonstrated that aging cause a 40% reduction of crack-initiation toughness and a total elimination of the crack-growth toughness [73].

Aging effects act at various scales, leading to internal changes in the bone structure, thus affecting the nano- to macroscopic properties: at the nanoscale, changes occur in the structure of collagen, due to the reduction of the cross-link density; at the submicrometer scale, a general deterioration of collagen fibrils and mineralized fibrils occurs, with decrease in stiffness, strength and toughness; at the microscale, an increase in the number of osteons, which are proved to have the largest effects on the macroscale fracture toughness [24], alters the structure. At the larger scales, both in the case of cortical and spongy bones, the reduction in bone mineral density (BMD) can be seen as the main consequence of the age-induced fracture risk [74].

Beyond the effects of aging, in case of disease the structure of bony tissues can undergo further changes. Examples of common diseases are the *Osteoporosis* and the *Osteoarthritis*: in the former, the collagen is characterized by a reduced level of the immature cross-links, which

makes the collagen fibrils closer to each other and more disorganized; in the latter case, the age-related effects are on the cartilage collagen. Also, a homotrimer type is present in larger amount than usual, resulting in narrower CF, less stable and more disorganized [75].

Osteogenesis Imperfecta

Osteogenesis Imperfecta (OI), also known as Brittle Bone Disease (BBD) is a heritable disorder of collagen type I, which results in skeletal deformities and weak and brittle bones [31]. This phenomenon is studied through mice OI models (*oim*), which seem to have a similar phenotype to the severe OI in humans. The consequences of this OI have been largely seen in experimental studies on mice, with reduced post-yield deformation and brittle fracture mode [76, 77]. However, the mechanisms are still not clear, and these models includes only modifications of the collagen, though OI is thought to affect the mineral crystals as well. Indeed, a deranged collagen could affect the biomineralization process, in the early stages of bone formation, leading to an altered biomineralization process, and to a different size, shape and distribution of the HAP platelets [78]. This can in turn affect the mechanical response of the platelets, and the whole mineral-matrix composite (*i.e.* mineralized tissue). The effects of OI-related diseases on the protein domain have been largely studied by means of simulation techniques, with a molecular and mesoscale approach [79, 80].

1.6 Outline

In this work, after a deep study of the bone hierarchical structure, we use an atomistic approach to get an insight into the mechanical properties of the bone building blocks, the collagen organic fibers and the hydroxyapatite mineral crystals. We carry out full atomistic simulations to get information about the mechanical behavior of the bone basic components, their interactions and the size effect on their mechanical performance. Moreover, we study the mechanical response of HAP crystals in presence of a defect, by means of an atomistic approach, and investigate the effect of confinement on their fracture behavior. At the meantime, we use a biomimetic approach to create a new material, with the aim of replicating some of the toughening mechanisms operating in bone and harnessing them in engineering materials. Hence, by observing the bone structure, we select structural features of bone, the osteons, characteristic of the secondary haversian structure of bone at the micro-scale (*i.e.* μm to mm), and implement them in a new glass-carbon/epoxy synthetic composite, which could replicate the toughening mechanisms of crack deflection and twisting. After designing and manufacturing the new bio-inspired material, we perform an experimental characterization of both the new material and a classical laminate, chosen for comparison. We also provide optimization techniques to further improve the newly designed material. The new concept of bio-inspired material is not meant to be a mere copy of what is found in nature, but instead it aims to provide a smart solution for engineering problems, with potential applications in structural fields (*e.g.* automotive).

Bibliography

- [1] H. Gao, B. Ji, I. Jager, E. Arzt, and P. Fratzl, "Materials become insensitive to flaws at nanoscale: Lessons from nature," *Proceedings of the National Academy of Sciences*, vol. 100, no. 10, pp. 5597–5600, 2003.
- [2] B. Ji and H. Gao, "Mechanical properties of nanostructure of biological materials," *Journal of the Mechanics and Physics of Solids*, vol. 52, p. 1963, 2004.
- [3] H. Gao, *Application of fracture mechanics concepts to hierarchical biomechanics of bone and bone-like materials Advances in Fracture Research*, pp. 101–137. Springer Netherlands, 2006.
- [4] P. Fratzl and R. Weinkamer, "Nature's hierarchical materials," *Progress in Material Science*, vol. 52, p. 1263, 2007.
- [5] M. Buehler, "Nano- and micromechanical properties of hierarchical biological materials and tissues," *Journal of Materials Science*, vol. 42, p. 8765, 2007.
- [6] B. Bhushan, "Biomimetics: lessons from nature-an overview," *Philosophical Transactions of the Royal Society A: Mathematical, Physical and Engineering Sciences*, vol. 367, no. 1893, pp. 1445–1486, 2009.
- [7] H. D. Espinosa, J. E. Rim, F. Barthelat, and M. J. Buehler, "Merger of structure and material in nacre and bone - perspectives on de novo biomimetic materials," *Progress in Materials Science*, vol. 54, no. 8, pp. 1059–1100, 2009.
- [8] O. Schmitt, "Some interesting and useful biomimetic transofrms," *Third Int. Biophysics Congress*, p. 297, 1969.
- [9] B. Bhushan, *Biomimetics. Biological and Medical Physics, Biomedical Engineering*, Berlin Heidelberg: Springer-Verlag, 2012.
- [10] H. Kessler, R. Ballarini, R. Mullen, L. Kuhn, and A. Heuer, "A biomimetic example of brittle toughening. 1. steady state multiple cracking," *Computational Materials Science*, vol. 5, p. 157, 1996.
- [11] J. Vincent, O. A. Bogatyreva, N. Bogatyrev, A. Bowyer, and A. Pahl, "Biomimetics: its practice and theory," *Journal of The Royal Society Interface*, vol. 3, no. 9, pp. 471–482, 2006.
- [12] P. Fratzl, "Biomimetic materials research: What can we really learn from nature's structural materials?," *Journal of the Royal Society Interface*, vol. 4, p. 637, 2007.
- [13] M. D. Bartlett, A. B. Croll, D. R. King, B. M. Paret, D. J. Irschick, and A. J. Crosby, "Biomimetics: Looking beyond fibrillar features to scale gecko-like adhesion," *Advanced Materials*, vol. 24, no. 8, pp. 994–994, 2012.
- [14] C. Lekakou, D. Lamprou, U. Vidyarthi, E. Karopoulou, and P. Zhdan, "Structural hierarchy of biomimetic materials for tissue engineered vascular and orthopedic grafts," *Journal of biomedical materials research. Part B, Applied biomaterials*, vol. 85, no. 2, pp. 461–8, 2008.

- [15] G. de Mestral, "Improvements in or relating to a method and a device for producing a velvet type fabric," 1955.
- [16] Y. Bar-Cohen, *Biomimetics: Biologically Inspired Technologies*. CRC Press/INC, 2006.
- [17] M. Milwich, T. Speck, O. Speck, T. Stegmaier, and H. Planck, "Biomimetics and technical textiles: solving engineering problems with the help of nature's wisdom," *American Journal of Botany*, vol. 93, no. 10, pp. 1455–1465, 2006.
- [18] K. A. Gross and E. Ezerietis, "Juniper wood as a possible implant material," *Journal of Biomedical Materials Research Part A*, vol. 64A, no. 4, pp. 672–683, 2003.
- [19] H. Lowenstam and S. Weiner, *On Biomineralization*. Oxford University Press, 1989.
- [20] M. Sarikaya and I. Aksay, *Biomimetics: Design and Processing of Materials*. Springer Verlag, 1995.
- [21] M. A. Meyers, P. Y. Chen, A. Y. M. Lin, and Y. Seki, "Biological materials: Structure and mechanical properties," *Progress in Materials Science*, vol. 53, no. 1, pp. 1–206, 2008.
- [22] S. Deville, E. Saiz, R. K. Nalla, and A. P. Tomsia, "Freezing as a path to build complex composites," *Science*, vol. 311, no. 5760, pp. 515–518, 2006.
- [23] R. O. Ritchie, J. J. Kruzic, C. L. Muhlstein, R. K. Nalla, and E. A. Stach, "Characteristic dimensions and the micro-mechanisms of fracture and fatigue in 'nano' and 'bio' materials," *International Journal of Fracture*, vol. 128, no. 1, pp. 1–15, 2004.
- [24] R. O. Ritchie, M. J. Buehler, and P. Hansma, "Plasticity and toughness in bone," *Physics Today*, vol. 62, no. 6, pp. 41–47, 2009.
- [25] M. E. Launey, M. J. Buehler, and R. O. Ritchie, "On the mechanistic origins of toughness in bone," *Annual Review of Materials Research*, vol. 40, no. 1, pp. 25–53, 2010.
- [26] R. Nalla, J. Kruzic, J. Kinney, and R. Ritchie, "Mechanistic aspects of fracture and r-curve behavior in human cortical bone," *Biomaterials*, vol. 26, p. 217, 2005.
- [27] K. J. Koester, J. W. Ager, and R. O. Ritchie, "The true toughness of human cortical bone measured with realistically short cracks," *Nature Materials*, vol. 7, no. 8, pp. 672–677, 2008.
- [28] J. Currey, "Materials science: hierarchies in biomineral structures," *Science*, vol. 309, p. 253, 2005.
- [29] L. M. McNamara, *Bone as a Material*, vol. 1 of *Comprehensive Biomaterials, Seven-Volume Set*. Elsevier Science, 2011.
- [30] D. Taylor, J. G. Hazenberg, and T. C. Lee, "Living with cracks: Damage and repair in human bone," *Nature Materials*, vol. 6, no. 4, pp. 263–268, 2007.
- [31] F. Bronner, M. Farach-Carson, and H. Roach, *Osteogenesis Imperfecta*, vol. 6, ch. 13. Springer-Verlag London Limited, 2010.
- [32] C. H. Turner, "Three rules for bone adaptation to mechanical stimuli," *Bone*, vol. 23, no. 5, pp. 399–407, 1998.

- [33] P. Fratzl, *Collagen: Structure and Mechanics*. Springer US, 2008.
- [34] G. N. Ramachandran and G. Kartha, "Structure of collagen," *Nature*, vol. 176, no. 4482, pp. 593–595, 1955.
- [35] J. Uitto, "Collagen polymorphism: Isolation and partial characterization of $\alpha 1(i)$ -trimer molecules in normal human skin," *Archives of Biochemistry and Biophysics*, vol. 192, no. 2, pp. 371–379, 1979.
- [36] L. C. Wu, J. Yang, and J. Kopecek, "Hybrid hydrogels self-assembled from graft copolymers containing complementary beta-sheets as hydroxyapatite nucleation scaffolds," *Biomaterials*, vol. 32, no. 23, pp. 5341–53, 2011.
- [37] S. Bhumiratana, W. L. Grayson, A. Castaneda, D. N. Rockwood, E. S. Gil, D. L. Kaplan, and G. Vunjak-Novakovic, "Nucleation and growth of mineralized bone matrix on silk-hydroxyapatite composite scaffolds," *Biomaterials*, vol. 32, no. 11, pp. 2812–20, 2011.
- [38] B. Alexander, T. L. Daulton, G. M. Genin, J. Lipner, J. D. Pasteris, B. Wopenka, and S. Thomopoulos, "The nanometre-scale physiology of bone: steric modelling and scanning transmission electron microscopy of collagen-mineral structure," *Journal of the Royal Society Interface*, vol. 9, no. 73, pp. 1774–86, 2012.
- [39] R. Z. LeGeros, A. Ito, K. Ishikawa, T. Sakae, and J. P. LeGeros, *Fundamentals of Hydroxyapatite and Related Calcium Phosphates*, pp. 19–52. John Wiley & Sons, Inc., 2010.
- [40] J. Y. Rho, L. Kuhn-Spearing, and P. Zioupos, "Mechanical properties and the hierarchical structure of bone," *Medical Engineering & Physics*, vol. 20, no. 2, pp. 92–102, 1998.
- [41] R. Bhowmik, K. S. Katti, and D. R. Katti, "Influence of mineral-polymer interactions on molecular mechanics of polymer in composite bone biomaterials," *MRS Online Proceedings Library*, vol. 978, 2006.
- [42] R. Bhowmik, K. S. Katti, and D. R. Katti, "Investigating the interfacial interactions between organic and inorganic phases and their influence on the mechanics of organic phase in natural bone," *MRS Online Proceedings Library*, vol. 975, 2006.
- [43] M. Buehler, "Molecular nanomechanics of nascent bone: fibrillar toughening by mineralization," *Nanotechnology*, vol. 18, p. 295102, 2007.
- [44] R. Bhowmik, K. S. Katti, D. Verma, and D. R. Katti, "Probing molecular interactions in bone biomaterials: Through molecular dynamics and fourier transform infrared spectroscopy," *Materials Science and Engineering: C*, vol. 27, no. 3, pp. 352–371, 2007.
- [45] R. Bhowmik, K. Katti, and D. Katti, "Mechanics of molecular collagen is influenced by hydroxyapatite in natural bone," *Journal of Materials Science*, vol. 42, no. 21, pp. 8795–8803, 2007.
- [46] D. K. Dubey and V. Tomar, "Role of the nanoscale interfacial arrangement in mechanical strength of tropocollagen-hydroxyapatite-based hard biomaterials," *Acta Biomaterialia*, vol. 5, no. 7, pp. 2704–2716, 2009.
- [47] Z. Qin, A. Gautieri, A. Nair, H. Inbar, and M. J. Buehler, "Thickness of hydroxyapatite nanocrystal controls mechanical properties of the collagen-hydroxyapatite interface," *Langmuir*, vol. 28, no. 4, pp. 1982–1992, 2012.

- [48] N. Almora-Barrios and N. H. De Leeuw, "Molecular dynamics simulation of the early stages of nucleation of hydroxyapatite at a collagen template," *Crystal Growth & Design*, vol. 12, no. 2, pp. 756–763, 2011.
- [49] G. H. Nancollas and W. Wu, "Biomineralization mechanisms: a kinetics and interfacial energy approach," *Journal of Crystal Growth*, vol. 211, no. 1-4, pp. 137–142, 2000.
- [50] M. J. Olszta, X. Cheng, S. S. Jee, R. Kumar, Y.-Y. Kim, M. J. Kaufman, E. P. Douglas, and L. B. Gower, "Bone structure and formation: a new perspective," *Materials Science and Engineering: R: Reports*, vol. 58, no. 3-5, pp. 77–116, 2007.
- [51] J. W. Shen, T. Wu, Q. Wang, and H. H. Pan, "Molecular simulation of protein adsorption and desorption on hydroxyapatite surfaces," *Biomaterials*, vol. 29, no. 5, pp. 513–532, 2008.
- [52] I. Jager and P. Fratzl, "Mineralized collagen fibrils: a mechanical model with a staggered arrangement of mineral particles," *Biophysical Journal*, vol. 79, p. 1737, 2000.
- [53] P. Fratzl, H. S. Gupta, E. P. Paschalis, and P. Roschger, "Structure and mechanical quality of the collagen-mineral nano-composite in bone," *Journal of Materials Chemistry*, vol. 14, no. 14, pp. 2115–2123, 2004.
- [54] M. J. Buehler, S. Keten, and T. Ackbarow, "Theoretical and computational hierarchical nanomechanics of protein materials: Deformation and fracture," *Progress in Materials Science*, vol. 53, no. 8, pp. 1101–1241, 2008.
- [55] M. Wallwork, J. Kirkham, J. Zhang, D. Smith, and S. Brookes, "Binding of matrix proteins to developing enamel crystals: an atomic force microscopy study," *Langmuir*, vol. 17, p. 2508, 2001.
- [56] M. Iijima and J. Moradian-Oldak, "Control of apatite crystal growth in a fluoride containing amelogenin-rich matrix," *Biomaterials*, vol. 26, no. 13, pp. 1595–1603, 2005.
- [57] H. B. Wen, A. G. Fincham, and J. Moradian-Oldak, "Progressive accretion of amelogenin molecules during nanospheres assembly revealed by atomic force microscopy," *Matrix Biology*, vol. 20, no. 5-6, pp. 387–395, 2001.
- [58] J. C. Elliott, P. E. Mackie, and R. A. Young, "Monoclinic hydroxyapatite," *Science*, vol. 180, no. 4090, pp. 1055–1057, 1973.
- [59] M. Corno, C. Busco, V. Bolis, S. Tosoni, and P. Ugliengo, "Water adsorption on the stoichiometric (001) and (010) surfaces of hydroxyapatite: A periodic b3lyp study," *Langmuir*, vol. 25, no. 4, pp. 2188–2198, 2009.
- [60] R. Martin, D. Burr, and N. Sharkey, *Skeletal Tissue Mechanics*. Springer, 1998.
- [61] P. Fratzl and H. S. Gupta, *Nanoscale mechanisms of bone deformation and fracture*, vol. 1 of *Handbook of Biomineralization*. 2007.
- [62] D. K. Dubey and V. Tomar, "Microstructure dependent dynamic fracture analyses of trabecular bone based on nascent bone atomistic simulations," *Mechanics Research Communications*, vol. 35, no. 1-2, pp. 24–31, 2008.

- [63] H. Gupta, J. Seto, W. Wagermaier, P. Zaslansky, P. Boesecke, and P. Fratzl, "Cooperative deformation of mineral and collagen in bone at the nanoscale," *Proceedings of the National Academy of Sciences*, vol. 103, p. 17741, 2006.
- [64] H. S. Gupta, W. Wagermaier, G. A. Zickler, D. Raz-Ben Aroush, S. S. Funari, P. Roschger, H. D. Wagner, and P. Fratzl, "Nanoscale deformation mechanisms in bone," *Nano Letters*, vol. 5, no. 10, pp. 2108–2111, 2005.
- [65] J.-Y. Rho, T. Y. Tsui, and G. M. Pharr, "Elastic properties of human cortical and trabecular lamellar bone measured by nanoindentation," *Biomaterials*, vol. 18, no. 20, pp. 1325–1330, 1997.
- [66] C. H. Turner, J. Rho, Y. Takano, T. Y. Tsui, and G. M. Pharr, "The elastic properties of trabecular and cortical bone tissues are similar: results from two microscopic measurement techniques," *Journal of Biomechanics*, vol. 32, no. 4, pp. 437–441, 1999.
- [67] K. Choi, J. L. Kuhn, M. J. Ciarelli, and S. A. Goldstein, "The elastic moduli of human subchondral, trabecular, and cortical bone tissue and the size-dependency of cortical bone modulus," *Journal of Biomechanics*, vol. 23, no. 11, pp. 1103–1113, 1990.
- [68] L. M. McNamara, A. G. H. Ederveen, C. G. Lyons, C. Price, M. B. Schaffler, H. Weinans, and P. J. Prendergast, "Strength of cancellous bone trabecular tissue from normal, ovariectomized and drug-treated rats over the course of ageing," *Bone*, vol. 39, no. 2, pp. 392–400, 2006.
- [69] P. R. Townsend, P. Raux, R. M. Rose, R. E. Miegel, and E. L. Radin, "The distribution and anisotropy of the stiffness of cancellous bone in the human patella," *Journal of Biomechanics*, vol. 8, no. 6, pp. 363–367, 1975.
- [70] J. Runkle and J. Pugh, "The micro-mechanics of cancellous bone. ii. determination of the elastic modulus of individual trabeculae by a buckling analysis," *Bulletin of the Hospital for Joint Diseases*, vol. 36, no. 1, pp. 2–10, 1975.
- [71] R. B. Ashman and J. Y. Rho, "Elastic modulus of trabecular bone material," *Journal of Biomechanics*, vol. 21, no. 3, pp. 177–181, 1988.
- [72] P. L. Mente and J. L. Lewis, "Experimental method for the measurement of the elastic modulus of trabecular bone tissue," *Journal of Orthopedic Research*, vol. 7, no. 3, pp. 456–461, 1989.
- [73] B. Smith, T. Schaffer, M. Viani, J. Thompson, and N. Frederick, "Molecular mechanistic origin of the toughness of natural adhesives, fibres and composites," *Nature*, vol. 399, p. 761, 1999.
- [74] P. J. Thurner, B. Erickson, R. Jungmann, Z. Schriock, J. C. Weaver, G. E. Fantner, G. Schitter, D. E. Morse, and P. K. Hansma, "High-speed photography of compressed human trabecular bone correlates whitening to microscopic damage," *Engineering Fracture Mechanics*, vol. 74, no. 12, pp. 1928–1941, 2007.
- [75] A. J. Bailey, T. J. Sims, and L. Knott, "Phenotypic expression of osteoblast collagen in osteoarthritic bone: production of type i homotrimer," *The International Journal of Biochemistry & Cell Biology*, vol. 34, no. 2, pp. 176–182, 2002.

- [76] J. D. J. McBride, J. R. Shapiro, and M. G. Dunn, "Bone geometry and strength measurements in aging mice with the oim mutation," *Calcified tissue international*, vol. 62, no. 2, pp. 172–176, 1998.
- [77] N. P. Camacho, L. Hou, T. R. Toledano, W. A. Ilg, C. F. Brayton, C. L. Raggio, L. Root, and A. L. Boskey, "The material basis for reduced mechanical properties in oim mice bones," *Journal of Bone and Mineral Research*, vol. 14, no. 2, pp. 264–272, 1999.
- [78] B. Grabner, W. J. Landis, P. Roschger, S. Rinnerthaler, H. Peterlik, K. Klaushofer, and P. Fratzl, "Age- and genotype-dependence of bone material properties in the osteogenesis imperfecta murine model (oim)," *Bone*, vol. 29, no. 5, pp. 453–457, 2001.
- [79] A. Gautieri, S. Vesentini, A. Redaelli, and M. J. Buehler, "Single molecule effects of osteogenesis imperfecta mutations in tropocollagen protein domains," *Protein Science*, vol. 18, no. 1, pp. 161–168, 2009.
- [80] A. Gautieri, S. Uzel, S. Vesentini, A. Redaelli, and M. J. Buehler, "Molecular and mesoscale mechanisms of osteogenesis imperfecta disease in collagen fibrils," *Biophysical Journal*, vol. 97, no. 3, pp. 857–865, 2009.

Chapter 2

Introduction to Composite Materials

This chapter is dedicated to a discussion of composite materials. The purpose of this chapter is to provide an introduction to composites. We describe structural composites, including the description of the basic constituents (*i.e.* reinforcement and matrix), the most common manufacturing techniques, and the wide range of applications. We conclude the chapter with a brief section on bio-inspired composites, topic covered in detail in Chapter 1.

2.1 Introduction

The word composite has a Latin origin, as it comes from the word *componere*, which means to put something together. In material science, a composite is a material made of two or more materials with significantly different physical, chemical and mechanical properties. Although the properties of the constituents remain the same, the combination of them leads to a new material, whose properties are better than those provided by the individual constituents. Composites can be either engineered or naturally occurring materials. Examples of naturally occurring composites are wood, bone and nacre, whereas examples of engineered composites are fiber reinforced plastics (*i.e.* FRP), ceramic/metal composites, and ceramic/ceramic composites, such as concrete.

The aim of creating composites is to get materials with better performances, taking advantage of the best properties of the constituents. For instance, in case of fiber reinforced composites (*i.e.* FRC), or simply fiber composites (*i.e.* FC), stiff and strong fibers are combined with a flexible matrix, which transfers the load between the fibers, protecting them from direct damage. In this way, it is possible to get high mechanical properties, especially if compared with the weight. Moreover, the use of polymer matrix can provide corrosion resistance. Other advantages can be the thermal stability, the thermal and acoustic insulations, and a good fatigue behavior.

Composites are generally designed for a specific application, and manufactured at the same time as the component (*e.g.* a pultruded profile). This is a large difference with conventional materials, such as steels, metals and polymers, whose products are generally produced on a large scale, by different mechanical techniques (*e.g.* extrusion, foundry, die-casting, blow-molding, rolling). Also, the constituent materials, the proportion of each, the direction of the reinforcement are chosen to meet the design requirements, to be suitable for a particular application. Indeed, the possibility of tailoring them to meet specific requirements for the chosen application is probably the best feature of composites. However, to fully exploit this characteristic, it is

important to accurately predict the behavior of the structure they are designed to, based on the material characteristic and design. On the other hand, the recycling is a critical aspect of those materials, especially in case of a polymer matrix.

The most advanced examples of composites perform regularly on spacecraft in demanding environments. However, recently the need of reducing CO₂ emissions, either for the increasing fuel costs and for the environmental impact, has pushed the research forward to produce lightweight structures in the automotive field as well. Therefore, due to their high strength-to-weight ratios, in the last decades there is a larger use of composite materials in different fields, such as building constructions, aviation and automotive industry, replacing the conventional materials (*i.e.* steel); hence, an increasing need of studying their mechanical and damage behavior. Generally, theoretical methods and numerical modeling provide the basis to predict the behavior of composites, hence those are largely used in the design process [1–5]. Nevertheless, due to the complexity of those materials, experimental testing are always carried out to validate the predictions. Besides, nondestructive techniques are becoming more and more useful to study the damage behavior, either in the design phase, and for in-service monitoring.

Natural composites have been described in the previous chapter (Chapter 1), with a particular focus on bone and bone-like materials, which are the key topics of this thesis project. In this chapter, an overview of composites materials is given: first of all a description of structural composites, together with their basic components, the manufacturing techniques and applications. The last part of this chapter (Section 2.4) is dedicated to bio-inspired composite materials, an emergent topic in the field of composites.

2.2 Composites for Structural Applications

Composites for structural applications are generally known as FRC, because of the shape of the reinforcement, and consist of fibrous materials embedded into a polymer based matrix. The choice of the fiber and matrix type is due to different reasons: fibers are generally chosen so as to give the desired properties to the material, whereas the matrix is chosen to meet compatibility requirements with the matrix. In addition to fiber composites, other types of composites, made of different components and with different reinforcement shapes, are also used for structural applications, to satisfy diverse requirements. In this section, a description of the various types of reinforcement and matrix is given. Figure 2.1 shows a classification of composite materials on the basis of the reinforcement type, and schematic examples of structural composites.

2.2.1 The Reinforcement

The most common types of reinforcement for composites can be divided into three main groups, depending on their shape: *i)* spherical particles, *ii)* platelets, *iii)* fibers.

The first type is mainly used in ceramic/ceramic, metal/metal and ceramic/metal composites; however, it is also used in case of polymers, where particulate reinforcements are chosen with the aim of improving the matrix properties (*e.g.* stiffness, toughness, electrical conductivity, surface hardness) and reducing the total cost of the system. For instance fly ash, an industrial waste with good properties, is used as filler in epoxy with the effects of increasing the compressive properties of the resulting composite [6, 7]. Also, since the increasing use of composites has raised the problem of recycling, recycled particles, obtained by mechanically breaking old composite materials into finer elements, are used, together with other reinforcement types, such as fibers, to replace the filler and part of the reinforcement, taking over the reinforcing functions [8]. In some cases, particles, which are less rigid than the matrix, are used to improve the

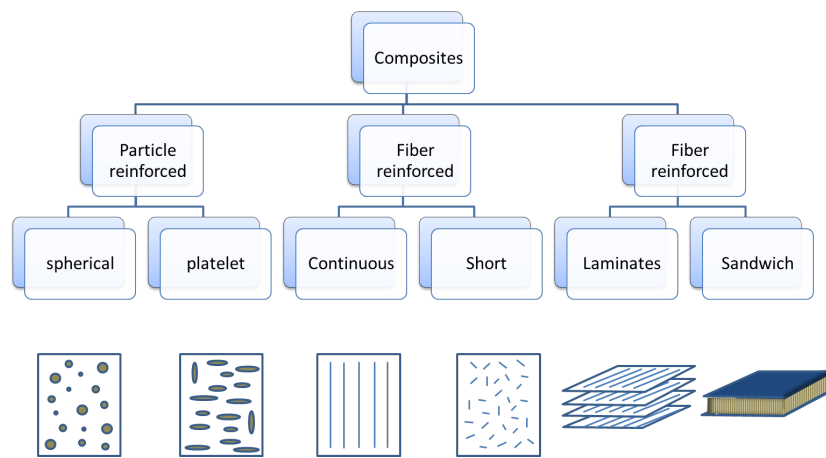


Figure 2.1: Schematic of the classification of composite materials on the basis of the reinforcement type; schematic examples of structural composite (on the right).

matrix toughness, with a consequent reduction in stiffness; it is the case of rubber particles into a glassy polymer matrix [9].

Reinforcement with platelets or flakes is a type of reinforcement used to gain two-dimensional stiffening [10]. Platelet size and aspect ratio are very important, as they affect the platelet/matrix load transfer, hence the mechanical behavior of the composite itself. Beyond platelet-reinforced composites, flakes are also used in hybrid composites, together with a fibrous reinforcement.

Fibers represent the most spread type of reinforcement, especially for structural composites. Their widespread use for structural applications is mainly due to the consistent improvement they bestow to the matrix material. Their shape also contributes to further increase their mechanical performance (*e.g.* the stiffness) with respect to the bulk material, thanks to the fiber's small diameter, which strongly reduces the probability of the presence of critical defects, and to the alignment or preferential orientation of molecular crystal structures [11]. Reinforcing fibers belong to three main categories: *i*) inorganic, *ii*) carbon, and *iii*) polymeric.

2.2.1.1 Fiber Reinforcement: Inorganic Fibers

Inorganic fibers, such as glass, boron, alumina, and silicon carbide are mostly isotropic. The most used ones for FRP are glass fibers, also known as fiberglass. Though their high density, compared to the other types of fibers, the low tensile modulus, the low fatigue resistance, and the poor adhesion properties, they show other advantages, such as low cost, high tensile strength, chemical resistance and insulating properties, which justify the large use of this material as reinforcement. Among the fiberglass, the most widely used for structural applications are E-glass and S-glass, with a slightly different chemical composition; the former are generally cheaper, but with lower properties, the latter are used for applications with higher requirements, since they have a higher quality, in particular higher thermal stability and the highest tensile strength among the industrial fibers, and a higher price as well. Beyond these fibers, there is also another type, C-glass, with higher corrosion resistance. Glass fibers are produced by rapidly drawing molten glass down to get fine filaments, of the order of ten microns ($10 \mu\text{m}$) in diameter. The confined diameter size considerably reduces the probability of finding any defects of a size, comparable to those found in bulk glass. Glass fibers are often subject to surface treatments to

increase the resistance to corrosive environments, and the compatibility with the matrix.

Among inorganic fibers, boron f. are also very common. They are produced, in diameter size ranging from 100 to 200 μm , by chemical vapor deposition (CVD) on a tungsten filament, heated up to 1260 °C, from the reduction of boron trichloride (BCl_3) with hydrogen. These fibers are generally chosen for their high tensile strength, though their elevated cost.

A good combination of high stiffness and strength with resistance to elevated temperature and environmental corrosion, is given by inorganic ceramic fibers, like alumina Al_2O_3 or silicon carbide (SiC). The former are obtained by wet spinning, and the latter ones, by CVD or controlled pyrolysis of a polymeric precursor.

2.2.1.2 Fiber Reinforcement: Carbon Fibers

Carbon fibers are used for applications with high requirements, since they provide the best combination of high stiffness and strength. Recently they are produced in different types, varying the degree of microstructural orientation, thus the strength and tensile modulus. The chemical structure of carbon fibers accounts for their elevated strength and modulus and their marked anisotropy, showing considerably higher mechanical properties in the longitudinal direction with respect to the transversal one; in particular, the graphitic form, with carbon atoms arranged in crystallographic planes. Indeed, carbon atoms are covalently bonded in the graphite basal plane, bestowing high longitudinal rigidity and strength, whereas van der Waals interactions, between neighboring planes, are responsible of the lower transversal modulus.

Carbon fibers are well known for their mechanical performance; moreover, the high fatigue resistance and the low density of these fibers make them suitable for manufacturing lightweight structures. Some drawbacks are the high electrical conductivity, the low impact resistance, and above all, the elevated cost, which limits the large use of these fibers for commercial applications, restricting it to the aerospace field, where weight saving is a priority. The manufacturing process of carbon fibers consists of pyrolysis of a precursor, such as polyacrylonitrile (PAN), followed by hot-stretching and chemical surface treatment to improve their compatibility with the matrix in a composite. Resulting fibers have diameters ranging from 5 to 10 μm .

2.2.1.3 Fiber Reinforcement: Polymeric Fibers

Polymeric or organic fibers include fibers obtained from liquid crystalline polymers, such as aramid fibers (*i.e.* Kevlar), and fibers obtained by extended chain flexible polymers, such as ultra high molecular weight polyethylene (UHMWPE). Highly oriented aramid fibers are produced by wet-spinning polymer liquid solutions, containing highly-ordered chain domains. The most common type of organic fibers are aramid f., which have high tensile properties but low resistance in compression. In fact, the compressive strength is one-eighth of the respective tensile value.

Aramid fibers are also strongly anisotropic. When embedded into a resin matrix, aramid fibers confer high toughness and impact resistance to the final composite. Hence, owing to their resistance to impact damage, they are often combined with other fiber types, to get hybrid composites. UHMWPE fibers are produced by gel-spinning and, thanks to their low density, they have the highest specific strength. The main disadvantages are the low melting point, which limits their use at temperatures higher than 80 – 90 °C, the creep ratio, and the poor adhesion with polymer matrices. Then, besides the excellent mechanical properties, such as the elevated strength and the elastic modulus comparable to that of glass and aluminium, these fibers differ from the inorganic ones because they are not brittle.

Fibers are generally produced in continuous rowing. However, in composite materials they can be used as continuous or discontinuous fibers, depending on the application of the final composite. Continuous fibers can be used as unidirectional reinforcement, bestowing high anisotropy to the composite, or bidirectional, such as in textiles (*i.e.* woven, noncrimp, braided). Short fibers, which constitute short fiber composites (*i.e.* SFC), can be aligned, bestowing anisotropic features to the composite, or random oriented, leading to nearly isotropic composites. Generally, short fibers increase the elastic modulus of a composite, though to a lower extent than fibers; hence, they are used for applications with less-demanding requirements, or when the chosen manufacturing process is not suitable for long fibers. A literature survey with the typical properties of some commercial reinforcing fibers is given in Table 2.1.

Most of the above described reinforcement types can also be produced in nano-size, resulting in a further increase of certain mechanical properties. The idea of confining the reinforcing materials to the nano-scale comes from nature, where the components (*i.e.* building blocks) of many composite materials generally have a characteristic nano-size, which influences the performance of the whole material.

Table 2.1: Typical properties of some commercial reinforcing fibers (adapted from [12]).

Material	Density $10^3(\text{kg}\cdot\text{m}^{-3})$	Fiber Diameter (μm)	Young's modulus (GPa)	Tensile strength (GPa)
Inorganic fibers				
Silica (E-glass)	2.5	10	70	1.5-2.0
Silica (S-glass)	2.6	10	90	4.6
$\alpha\text{-Al}_2\text{O}_3$	3.9	20	385	1.8
SiC (monofilament)	3.1	100	400	3.5
Carbon fibers				
HS-(PAN precursor)	1.8	5.5	295	5.6
Organic fibers				
Aramid (Kevlar)	1.5	12	130	3.6
Polyethylene (UHMW)	0.97	38	175	3.0

2.2.2 The matrix

The use of matrix in composites is not to merely hold on the fibers, but it has several important functions: first of all, it binds the fiber together ensuring their alignment; it isolates the fibers from each other, so they can act separately, preventing or slowing down the cracks growth through sequences of fibers, and leading to higher strength values and less brittle materials; it protects the reinforcement from mechanical damage (*e.g.* abrasion) or environmental attack (*e.g.* oxidation); it can increase the toughness, in case of a good interfacial bond strength. Being the reinforcement, especially a fibrous one, the main load-bearing component, the principal role of the matrix is to ensure a correct load transfer from the composite into the reinforcement, enabling the composite to withstand a complex stress state, including compression, tension, bending and shear stresses [12].

Matrices may be based on polymer, metals or ceramics. The choice of the matrix depends on the chosen application, the properties required by that application, the chosen reinforcement, to meet compatibility requirements, and the manufacturing process. Ceramic or metal matrixes are used in case of particle or platelet reinforced composites, whereas in case of FRC, polymers

are generally preferred. Indeed, FRC are generally known as FRP, due to the large use of polymer matrices.

2.2.2.1 Polymer Resins

Polymer matrices, used to make structural composites, belong to two main classes: *thermoplastics* and *thermosets*.

Thermoplastics are characterized by few or no chemical cross-links, hence they are processed by simply increasing the temperature. During their processing those polymers are subject to thermal degradation, which prevents them to be re-processed many times, although no chemical reaction is involved in the molding procedure. Also, their high viscosity affects the processing method, making them more suitable for SFC. The most common types of matrices, adopted for SFC, are polypropylene (PP), polycarbonate (PC), nylons (PA), polyethyleneterephthalate (PET), polybutyleneterephthalate (PBT), and polyphenylene sulfide (PPS). Recently, high-performance thermoplastic matrices, such as polysulfone (PSU), polyethersulfone (PES), polyarylenesulfide (PAS), polyetheretherketone (PEEK), polyamideimide (PAI), polyetherimide (PEI), and thermoplastic polyimide (TPI), have been used for long-fiber composites [11].

Thermoset resins are largely used for long-FRC, in particular polyester and epoxy. The former are the most spread in industry, due to their low cost, the thermomechanical properties and the high durability. Epoxy resins are also largely used, thanks to the good affinity, in terms of adhesion, with most of the high-performance fibers, low post-curing shrinkage, insulating properties, resistance to chemical attack. Also, they have a broad range of properties, which can be achieved by combining the epoxy base-resin with a proper curing agent, and a small amount of catalyst. Unsaturated polyester (UP) resins are generally obtained by dissolving a polyester in a reactive monomer (*i.e.* styrene), which contains carbon-carbon double bonds, such as styrene. The role of the reacting diluent is to reduce the polyester viscosity, facilitating its processing; also, it acts as a cross-linking agent by reacting with unsaturation points of polyester molecules. Small quantities of peroxide or aliphatic azo compounds, used as catalysts, are added to initiate the curing reaction. As the temperature increases, those compounds decompose into free radicals, and their decomposition rate strongly affects the curing time.

Vinyl ester resins are obtained by dissolving unsaturated vinyl ester resins in a reactive monomer (*i.e.* styrene), like for UP resins. Styrene reacts at the unsaturation points of vinyl ester resin, forming cross-links. Compared to the UP resin, vinyl ester have a lower susceptibility to chemical attacks and a lower cross-link density, which leads to a higher capability of deformation (*i.e.* higher strain at break). However, as a drawback, they have a considerable volumetric shrinkage, in the range 5-10 %.

Epoxy resin are obtained from low molecular weight organic liquids, which contains a number of epoxide groups, known as oxirane rings or glycidyl groups. The epoxide groups have a cyclic structure, which consists of one oxygen and two carbon atoms. The epoxy liquid is mixed with diluents and flexibilizer fillers, to reduce the viscosity and increase the impact response of the final resin, respectively. The curing process is initiated by curing agents (*e.g.* aromatic or aliphatic amine, and anhydrides), or catalysts (*e.g.* Lewis acids or bases). The former are added in large quantity to the liquid epoxy, so that they are part of the final polymerized resin. The latter are considerable more reactive than the former ones, so they are added in small amounts, to allow the epoxy for homopolymerization. Indeed the epoxy rings open and react with each others. A literature survey with the typical properties of some commercial polymer resins is given in Table 2.2.

Table 2.2: Typical properties of some commercial polymer resins (adapted from [11]).

Resin type	Density $10^3(\text{kg}\cdot\text{m}^{-3})$	Tensile modulus (GPa)	Tensile strength (MPa)	Strain at break (%)
<i>Thermoplastics</i>				
Phenolics	1.30	3.5	50-55	1.7
Polyimide	1.31	3.2	55	1.5
<i>Thermosets</i>				
Epoxy	1.2-1.3	2.75-4.10	55-130	1-8
Unsaturated polyester (UP)	1.10-1.40	2.10-3.45	34.5-103.5	1-5
Vinyl Ester	1.12-1.32	3.0-3.5	73-81	3.5-5.5

2.2.2.2 Metal Matrices

Metal matrices generally include either a metal or an alloy, used as a matrix for Metal Matrix Composites (MMC), which are usually reinforced with ceramic particles. The selection of the suitable matrix alloys for MMC depends on the application the material is designed to. MMC are generally designed to improve the strength-to-weight and stiffness-to-weight ratios of the original components, by maintaining the properties of ductility, which are characteristic of the metal matrices. Generally light metal alloys are widely used as matrices, because they are easy to process, by powder sintering, ensuring a fast solidification, without any segregation problem, typical of conventional solidification. Examples of matrices are: conventional cast alloys (*e.g.* G-AlSi7), conventional wrought alloys (*e.g.* TiAl6V4), and special alloys (*e.g.* Al-Cu-Mg-Ni-Fe-alloy). For functional materials, to maintain high conductivity and ductility, non-alloyed or low-alloyed non-ferrous or noble metals are used [13].

2.2.2.3 Ceramic Matrices

Among the most common types of ceramic matrices, there are alumina, silicon carbide, zirconia. These are widely used alone as technical ceramics, but also combined with a reinforcement (*e.g.* monocrystalline whiskers or platelets, or multi-strand fibers) to increase the fracture toughness. Indeed, Ceramic Matrix Composites (CMC) ensure a consistent improvement of elongation, crack resistance and thermal shock resistance, compared to the pure ceramic material [14].

2.2.3 The interface and the sizing

The interface has a crucial role in load transfer between the reinforcement and the matrix, and consequently, on the mechanical properties of the composite itself. Also, it strongly affects the damage behavior of the composite, since it is generally considered to be a weak point, where the damage usually originates.

The interface is strictly influenced by the nature of the components, in particular by their physical, chemical and mechanical properties, and by the shape of the reinforcement, which affect the load transfer between the reinforcement and the matrix. It was noted that, the higher the fiber stiffness the poorer the resistance of the composite to shear forces in the plane of a laminate (*i.e.* the lower the interlaminar shear strength, ILSS). Therefore, many attempts were made to improve the characteristics of the interface, and consequently the ILSS. In particular, surface treatments, either chemical, such as polymer-coating or electrolytic oxidation, or physical, such as CVD. The electrolytic treatment was largely used in the past, becoming the most

common method. However, the surface of the fibers were overtreated (i.e. heavily oxidized) by the manufacturers, who did not control the process; this led to well wetted fibers by the resins, but brittle composites, with negative consequences on the use of carbon fibers for aeronautical components [12].

The interface between two components is not a mere boundary between two rather different materials, especially when chemical reactions occur when putting them together. The surfaces of the two components can be affected by chemical and physical modifications, resulting in a region of molecular dimensions (i.e. tens of μm) with new properties, different those of the major components. This region is called *interphase* and its control has become a major concern to manufacturers of commercial composite materials. Indeed, in manufacturing of FRP a special attention is paid to the interphase and to the treatments to improve the fiber-matrix adhesion. An established method is the *sizing*, a chemical treatment consisting of applying a size coating to the fiber surface after drawing, to increase the compatibility with the matrix. An example of size coating used for glass fibers is silane-coupling agent [7].

2.2.4 The Manufacturing Techniques

A large number of processing routes is available for composites, and selecting the right process for the product is crucial for its success. Generally, the design stage includes a fundamental analysis of the range of the manufacturing processes available and their advantages, disadvantages and limitations. Several factors influence the process selection: the number of parts required, the matrix and reinforcement types, the shape, the size and complexity of the product, the cost per unit part, the dimensional accuracy and tolerances, the finishing of the product, the mechanical properties (e.g. strength, stiffness), the post processing/assembly techniques. The most common techniques are: wet lay-up, spray lay-up, pultrusion, filament winding, and resin transfer molding (RTM).

2.2.4.1 Wet Lay-up

This technique is widely used but, since it is a manual technique, it is recently substituted by other techniques, due to health and safety risk related to the harmful resin curing vapors. It consists in manually placing the reinforcement into the mold, forcing the resin between the fibers, by means of brushes or rollers, and then curing, generally at room temperature. In case of a complex mold shape, layers of small pieces of mat are cut to fit and placed in sequence, until reaching the required thickness. The liquid resin is poured over the fiber and rolled to ensure complete wetting of the fiber and removal of air bubbles. Vacuum assisted wet lay-up can prevent the presence of voids, caused by air trapping, in the laminate: in this case, vacuum is applied to the part after lay-up, by sealing the part with a plastic film (bagging material) and extracting the air by means of a vacuum pump. In wet lay-up, to facilitate the component release, the mold cavity is coated with releasing agents (e.g. polyvinyl alcohol, non-silicon wax). To improve the surface finishing, a gel coat, which produces a resin rich layer, is placed onto the mold surface, ensuring a smooth surface for aesthetic and environmental protection purposes. Moreover, to further improve surface finish and corrosion resistance, a surface veil, with an embedded fabric for reinforcement or mixed with resin, is used.

The costs of this technique are moderate, since it is mainly manual and neither specific tools nor highly skilled labor are needed, but its application is limited to a small scale production. However, the low control on fiber orientation, resin content and impregnation do not make it suitable for components with high strength requirements.

2.2.4.2 Spray Lay-up

This technique has been designed for SFC, in particular for chopped glass fibers. It is a fast and low cost technique, where a specifically designed gun supplies the resin whilst chopping the continuous fibers, and the resin/fiber mix is then sprayed into a mold. However, due to the low viscosity required in the gun, the spray lay-up allows only for low fiber content. Low viscosity (*i.e.* low molecular weight resins) and highly reactive resins, such as vinyl ester, polyester, epoxy and phenolic, are used. Beside the fast application, other advantages are a good wetting of the fibers and low resin voids compared to the hand lay-up. Drawbacks are the low control of uniformity and thickness, and of resin content, which in turns lead to an increase in weight, and highly exothermal curing reaction, with consequent damage of the mold and the molded part.

2.2.4.3 Pultrusion

Pultrusion is a continuous process designed for large scale production of components with a constant cross section. Although the significant costs of machine for processing, the high productivity and energy-efficiency and the flexibility (*i.e.* the possibility of realizing different types of profiles, by changing the dies) allow for a large use of this technique for manufacturing of composites bar and profiles. This process consists in pulling the reinforcement, previously saturated with a thermoplastic or thermosetting resin, through a heated die, which gives the shape of the profile to be manufactured. The pultruded material -in exiting the die- is automatically cut to the required length.

Generally the pultruded components are characterized by a marked anisotropy, with fibers oriented in the pulling directions. With this technique, a high fiber volume fraction can be achieved, allowing pultruded parts to be used in structural applications.

2.2.4.4 Filament Winding

Filament winding is a manufacturing technique to realize cylindrical structure. It consists in wrapping the resin impregnated fibers around a rotating mandrel, with a convex shape (*e.g.* cylindrical, conical, or spherical), while a carriage moves horizontally, laying down fibers in the desired pattern. The layers of fibers are applied until reaching the required thickness of the laminate. The mandrel rotating speed and the traversing speed determine the fiber winding angle, making it possible to control the orientation of each layer. Once the winding is complete, the curing process is initiated, either by heating the mandrel while it is still on the machine, or by removing it and placing the part in an oven.

Although the significant cost of the mandrel, this technique is widely used for manufacturing high performance pipes, since it ensures a fast and cost-effective production, with a good control of the resin content.

2.2.4.5 Resin Transfer Molding - RTM

In the resin transfer molding (RTM) the dry reinforcement and resin are combined in the mold to form the finished structural component. The fiber reinforcement may be pre-pressed and pre-shaped before placing into the mold cavity. Resin materials, previously machine-mixed, are injected under pressure into the mold. Once the mold cavity is filled, the resin inlet is closed to initiate the curing process.

There are different resin injection types, including:

- Vacuum Assisted Resin Injection (VARI), where the molds are generally vented and the impregnation process occurs with the aid of a partial vacuum, allowing for a reduction of resin voids, especially in large size laminates or components with a complex shape. Variations of the VARI are the Vacuum Infusion (VI), designed for high quality components, since a complete vacuum is applied to reduce to minimum the amount of voids; in this case the composite is molded using a one side rigid mold to provide support and define the geometry, and a thin flexible membrane over the fibers, with outer atmospheric pressure keeping the fibers tight against the rigid mold surface (see Figure 2.2); the Vacuum Assisted RTM (VARTM), where vacuum is applied to the exit vent of the molding tool; the Seeman Composite Resin Infusion Molding Process (SCRIMP), a method of vacuum-assisted RTM producing high-quality composite parts from a wide range of fibers and resin combinations.
- Structural Reaction Injection Molding (SRIM), which is high pressure rapid dispensing process designed for low viscosity resins, such as polyurethanes.
- Resin Film Infusion (RFI), which involves a single mold and a vacuum bag. Dry fabrics are laid up, interleaved with layers of semi-solid resin film, supplied on a release paper. The lay-up is vacuum bagged to remove air through the dry fabrics, then heated to reduce the viscosity of the resin allowing to flow into the air-free fabrics, and then after a certain impregnation time, to cure.

Laminates obtained by RTM methods are characterized by high fiber content, low voids and good surface finish, also depending on the chosen combination of fiber and matrix. Also, the risk of hazardous vapors due to resin curing are limited, being the resin contained within the mold. Due to the high molding pressure and high temperature to withstand, the molds are generally expensive and unsuitable for low volume or prototype manufacture. RTM is mostly used for small components, whilst for larger parts RIM is preferred.

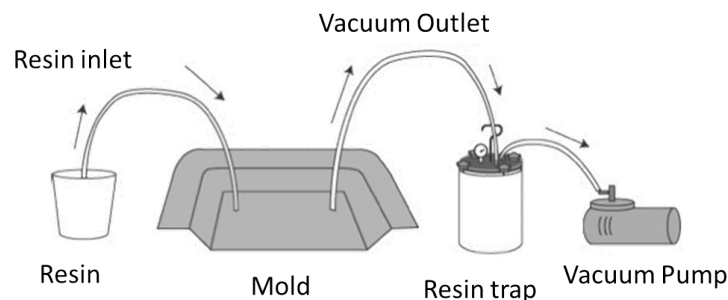


Figure 2.2: Schematic representation of the Vacuum infusion process.

2.2.5 The Applications

The success of composites is mainly due to the high mechanical properties-to-weight ratio compared to conventional materials, which makes them a better option, and to their versatility, being designed to carry out particular loads. The possibility for engineers to exercise high control over their mechanical properties, makes them very attractive materials. In fact, composites are considered to be engineered materials, since they are designed to adapt to a specific use.

Applications of composites are mainly in the aerospace and automotive fields, due to the high technical requirements, but also in building constructions, and marine applications. In aerospace, where the lightweight is a fundamental requirement, composites are largely used: for instance, the Airbus A380, introduced in 2006, is made of 25% wt. of FRP. Examples of composite components in Airbus A380 are: the tail cone, the vertical and the horizontal stabilizers, the spoilers, the outer wings. Indeed, since their first use, they allowed a consistent weight reduction compared to Aluminium and other conventional materials, beyond reducing the corrosion-related problems; in fact, in the last 40 years, thanks to the use of composites, the aviation industry has reduced fuel burn and CO₂ emissions by 70%, and noise by 75%.

Recently, the need of limiting the environmental impact of transportation means, by reducing the CO₂ emissions, as required by the economic politics of many European and non-European countries, has boosted the research to produce new composite and sandwich composite material structures, to be used in the automotive field. Research in the composite field has led to new materials, or improvement in existing materials, that can meet demanding criteria of flexural and torsional stiffness, crashworthiness, fatigue resistance and corrosion and fire resistance. Beyond reducing the weight of automotive components, these materials have been demonstrated to lead to reduced environmental impact, when a Life Cycle Cost approach is adopted. For these reasons, an increasing number of mechanical components for automotive industry are currently made of composite materials, instead of the traditional ones, reaching a good balance between the costs, the weight reduction and the performance improvement.

In the last decades, due to the high development of composite field, allowing a price reduction of these materials, their use has spread out to a more commercial one, including sportive items and electronic devices. Also, the possibility of tailoring composites to meet specific requirements has made them very attractive materials in the biomedical field, replacing conventional biomaterials (*e.g.* metals, polymers and ceramics) for implants and tissue engineering.

2.3 Bio-Inspired Composites

The 'composite' concept is not a human invention. Indeed, nature is the largest producer of composite materials. Wood, bone, dentin, cartilage, skin, nacre, all of them are examples of natural composites. Wood is a mainly polymer composite material made of cellulose fibers and a resinous matrix (*i.e.* the polysaccharide lignin). Bone, teeth, mollusc shells, instead are all ceramic-polymer composites, made of hard ceramic reinforcing phases embedded into natural organic polymer matrices. As largely described in Chapter 1, these biocomposites, also known as biominerals, are characterized by a hierarchical structure, consisting of a highly controlled organization at different levels and providing the material with multifunctional properties.

Nature makes a much better job of design and manufacture than man does, though man can study the natural systems and get inspiration from them, harnessing the ideas of nature and even limiting its shortcomings. For instance, by observing the structure of wood, man was able to overcome two major disadvantages of natural wood (*e.g.* the constrained size, limited by the transverse dimension of a tree, and the anisotropy, between the properties in axial and radial directions), by designing a wood-inspired composite material, called *plywood*. Wood has a hierarchical structure that shows many similarities to the one of bone, making it a good potential candidate for implantation [15]. Indeed, whereas bone is a ceramic-polymer composite, wood is predominantly a polymer composite. Both of them are considered natural structural materials, both characterized by a significant porosity and a hierarchical structure. Also, the microstructure of either materials is characterized by a repeating cylindrical feature,

called osteon in bone and tracheid in wood. Plywood is a manufactured wood panel made from thin layers of wood veneer. It is one of the most widely used wood products, thanks to its flexibility, low cost, workability, possibility of recycling, and the simple manufacturing process. Plywood is used instead of plain wood because of its resistance to cracking, shrinkage, splitting, and twisting, high degree of strength, versatility. Indeed, it exists in different types (*e.g.* softwood, hardwood, aircraft, marine, decorative plywood, *etc.*) designed for different applications. Figure 2.3 shows the microstructure of wood and that of plywood.

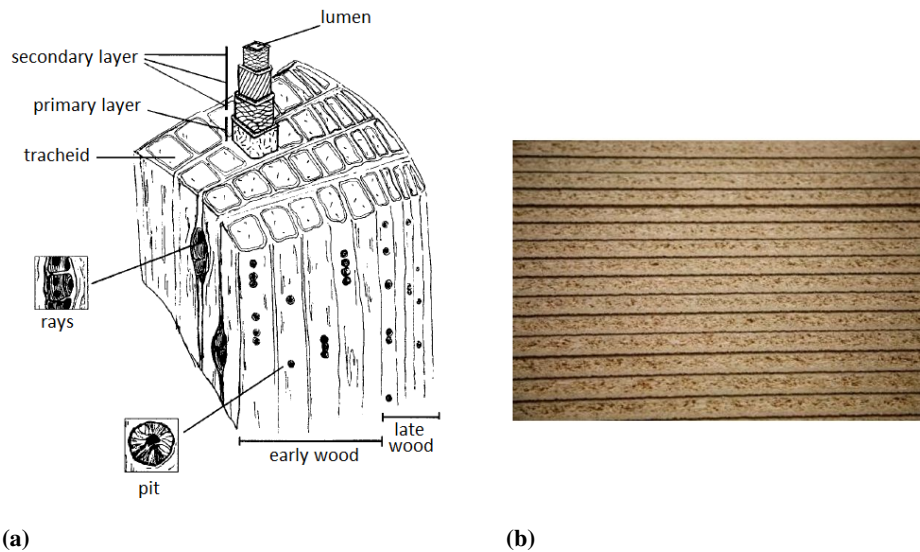


Figure 2.3: Comparison between the internal structure of wood and that of plywood. (a) Microstructure of wood, showing the primary and secondary layers in the tracheid and the pores aligned with the long axis in each cell (reproduced from [15]). (b) Structure of a commercial plywood.

Other examples of artificial composites, inspired to natural materials, are metal-metal (*e.g.* Ni-Al) or metal-ceramic nanocomposite structures, designed for shock-loading applications, so aimed to be stiff and tough. The inspiration of such composites from natural materials (*e.g.* bone and nacre) arises from the improved characteristics (*i.e.* strength and fracture toughness) of these materials, as compared to their constituents with inferior properties [16]. These improved properties are supposed to arise from the hierarchical arrangement.

2.4 Outline

Thanks to research in biomimetics, strong and stiff man-made nanocomposites mimicking nacre and bone have been developed; however, the microstructure of such composites has yet to achieve the order of detail and accuracy of the sophisticated hierarchy of biological materials. Man has still to face many challenging problems in the biomimicking synthesis (*e.g.*, control of the size, geometry, alignment of nanostructures, and higher levels of hierarchy) [17]. Besides materials synthesis and manufacturing, theoretical and numerical analyses, describing biomimetic composites at multiple length scales, represent major scientific and engineering challenges and opportunities. However, in order to realize an accurate design of multiscale

hierarchical materials, an integrated approach with concurrent experiments and computer simulations should be used. Also, the strong dependence of mechanical properties on the hierarchical organization of natural materials, makes it necessary to adopt a multiscale approach, especially in modeling and simulations, allowing to reach very small length scales, difficult to be reached with laboratory tools.

In this work, the concepts of biomimetics and biological materials, described in Chapter 1, and the concept of synthetic composite materials, described in this chapter, provide the basis for the development of a new synthetic and bio-inspired material. An integrated numerical-experimental approach is used, and described in the following chapters (Chapter 3-7). Chapter 8 provides a critical discussion of the results, along with new perspectives on future work.

Bibliography

- [1] R. Christensen, *Mechanics of Composite Materials*. Malabar, FL, USA: Kreiger Publishing Company, 1979.
- [2] H. Hahn and S. Tsai, *Introduction to Composite Materials*. Taylor & Francis, 1980.
- [3] S. Tsai, *Composites design*. Think Composites, 1988.
- [4] R. Jones, *Mechanics Of Composite Materials*. Taylor & Francis, 1998.
- [5] I. Daniel and O. Ishai, *Engineering Mechanics of Composite Materials*. Oxford University Press, USA, 2005.
- [6] S. Ahmed and F. R. Jones, "A review of particulate reinforcement theories for polymer composites," *Journal of Materials Science*, vol. 25, no. 12, pp. 4933–4942, 1990.
- [7] S. M. Kulkarni and K. Kishore, "Effects of surface treatments and size of fly ash particles on the compressive properties of epoxy based particulate composites," *Journal of Materials Science*, vol. 37, no. 20, pp. 4321–4326, 2002.
- [8] R. Rikards, K. Goracy, A. K. Bledzki, and A. Chate, "Prediction of mechanical properties of composites with recycled particles," *Mechanics of Composite Materials*, vol. 30, no. 6, pp. 563–574, 1994.
- [9] J. N. Sultan and F. J. McGarry, "Effect of rubber particle size on deformation mechanisms in glassy epoxy," *Polymer Engineering & Science*, vol. 13, no. 1, pp. 29–34, 1973.
- [10] C. H. Hsueh, "A two-dimensional stress transfer model for platelet reinforcement," *Composites Engineering*, vol. 4, no. 10, pp. 1033–1043, 1994.
- [11] C. Migliaresi and A. Pegoretti, *Fundamentals of Polymeric Composite Materials Integrated Biomaterials Science*, pp. 69–117. Springer US, 2002.
- [12] B. Harris, *Engineering composite materials*. Institute of Metals, 1986.
- [13] K. U. Kainer, *Metal Matrix Composites. Custom-made Materials for Automotive and Aerospace Engineering*. Weinheim: WILEY-VCH Verlag GmbH & Co. KGaA, 2006.
- [14] I. W. Donald and P. W. McMillan, "Ceramic-matrix composites," *Journal of Materials Science*, vol. 11, no. 5, pp. 949–972, 1976.
- [15] K. A. Gross and E. Ezerietis, "Juniper wood as a possible implant material," *Journal of Biomedical Materials Research Part A*, vol. 64A, no. 4, pp. 672–683, 2003.
- [16] N. C. Broedling, A. Hartmaier, M. J. Buehler, and H. Gao, "The strength limit in a bio-inspired metallic nanocomposite," *Journal of the Mechanics and Physics of Solids*, vol. 56, no. 3, pp. 1086–1104, 2008.
- [17] B. Ji and H. Gao, "Mechanical principles of biological nanocomposites," *Annual Review of Materials Research*, vol. 40, no. 1, pp. 77–100, 2010.

Part II

Numerical simulations

Chapter 3

Introduction to Atomistic Modeling of Materials

Atomistic modeling provides a fundamental description of the materials behavior. Atomistic simulation, which represents the numerical implementation, is a powerful tool to investigate the material properties along with deformation and failure mechanisms. Atomistic simulation includes molecular statics (MS), molecular dynamics (MD), and Monte Carlo (MC) statistical methods. This chapter aims to give an introduction to molecular dynamics modeling and simulation approaches. A brief description of the background, the basic principles, numerical algorithms, boundary conditions, statistical ensembles, energy minimization, and data post-processing of atomistic simulations is given.

3.1 Introduction

Materials properties are strictly dependent on their atomistic structure and its evolution under different chemical and physical conditions (*i.e.* corrosive environment, loading conditions). To understand the mechanisms of material deformation and failure, an in-depth investigation of the evolution of atomistic configuration with loading and time is crucial. However, being the atoms size on the angstrom scale, it is difficult and sometimes impossible to conduct direct experimental observation, hence making numerical simulation of materials at the atomistic scale essential. Molecular dynamics (MD) studies the atomic dynamic behavior at the subnanoscale; molecular statics (MS) is a special case of MD, used to perform static lattice calculations of systems at zero Kelvin temperature, hence with a negligible kinetic energy. Atomistic simulation can also be conducted statistically, by means of Monte Carlo (MC) methods, involving investigation of random processes for deformation and failure [1].

Molecular dynamics first appeared in the late 1950s, but due to the computer limitations its application was limited to simple case studies [2,3]. With the coming of new powerful computers, since 1980s, MD methods have become widely accepted and used in science and engineering fields. The ever increase in power computing, the continuous innovation in computational algorithms, and the increasing interest toward miniaturization, have led to a large use of MD to various engineering fields. Also, its interdisciplinary feature makes it possible to be applied to different branches of science, such as physics, chemistry, biology, mechanics and materials science, allowing one to visualize and observe the phenomena in detail at the atomic scale, getting information which can not be obtained in experiments. These characteristics make atomistic simulation adapt to explore natural phenomena and to develop new materials and technology.

3.2 Modeling and Simulations

Modeling and simulations refer to two different aspects of the same concept: the former is used to indicate a mathematical model to describe a physical situation, whereas the latter represents the numerical implementation of that model. Models are often simplification or schematization of real problems or physical phenomena [4]. Indeed, the main challenge of modeling is to provide a comprehensive, but simple physical representation of the system to be modeled; the main task of simulations, instead, is to choose the appropriate numerical technique to quickly solve a problem and to develop a proper strategy to reduce the computational effort.

3.3 Classical Molecular Dynamics

Classical molecular dynamics consists in determining the trajectories of molecules and atoms by numerically solving the Newton's equations of motion, with appropriate initial and boundary conditions, for a system of particles, whose interactions are described by a proper force field, while satisfying macroscopic thermodynamical (ensemble-averaged) constraints, leading to atomic positions, velocities, and accelerations as a function of time [1, 4, 5].

According to MD, atoms are described by a simple point representation, characterized by the atomic positions $\mathbf{r}_i(t)$, atomic velocities $\mathbf{v}_i(t)$ and accelerations $\mathbf{a}_i(t)$. Atoms are considered as particles obeying the Newton's laws of mechanics, where the initial velocities are generally determined from a Maxwell-Boltzmann distribution at the desired temperature. A schematic of the atom point representation and the dynamics of the system (*i.e.* force and interactions) is given in Figure 3.1.

MD methods are governed by the system's Hamiltonian, where the total energy, H , is the sum of two contributions (Eq. 3.1): the kinetic energy, $K = K(\mathbf{p})$, function of the velocities or linear momenta of the particles (Eq. 3.2), and the potential energy, $U = U(\mathbf{r})$, depending on the position vectors (Eq. 3.3).

$$H = K + U \quad (3.1)$$

$$K = \frac{1}{2} \sum_{i=1}^N m_i \mathbf{v}_i^2 \quad (3.2)$$

$$U(\mathbf{r}) = \sum_{i=1}^N U_i(\mathbf{r}) \quad (3.3)$$

The dynamics of the systems, thus of each particle included in the system, is governed by the Newton's law $\mathbf{F}_i = m_i \mathbf{a}_i$, where the force, acting on each particle can be expressed as function of the gradient of the potential energy:

$$m_i \frac{d^2 \mathbf{r}_i}{dt^2} = - \frac{dU(\mathbf{r})}{d\mathbf{r}_i} \quad (3.4)$$

Eq. 3.4 is a system of coupled second-order nonlinear partial differential equations, for a coupled system N -body problem. Due to the complicated nature of this function, there is no ana-

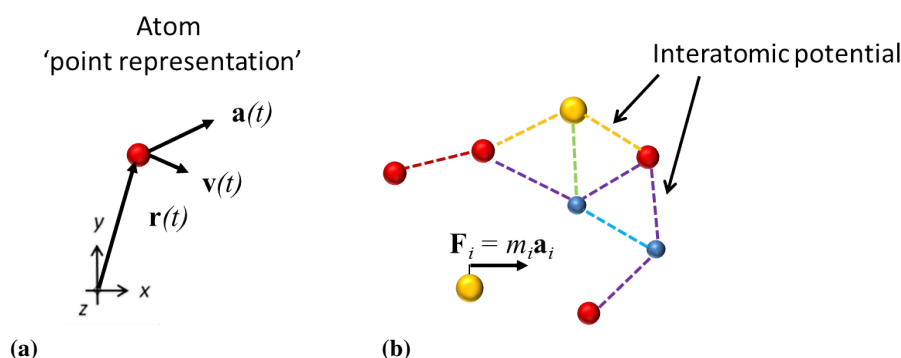


Figure 3.1: (a) Atom point representation in classical molecular dynamics. (b) Schematic representation of the dynamics of the system, governed by the Newton's law; particle-particle interactions are highlighted with color dashed lines (different colors aim to show the different interaction forces depending on the bond type).

lytical solution to the equations of motion, for $N > 2$; hence, they must be solved numerically.

An MD simulation scheme can be summarized as follows:

- Definition of a model for the interaction between system constituents (atoms, molecules), called *interaction potential* or *force field*.
- Definition of an integration scheme, which propagates particle positions and velocities from time t to $t + \delta t$. The time-step δt is chosen so as to guarantee stability of the integrator.
- Definition of a statistical ensemble, where thermodynamic quantities like pressure, temperature or the number of particles are controlled.

A brief description of each point follows.

3.3.1 Interatomic Potentials

The models for the determination of the potential function, U , and its related force field of the atomistic system is the key for atomistic simulation. These models are referred to as "interatomic potentials" or "force fields" models, where the first term is used in the physics community and the latter is more accepted in the chemistry community. The main task of interatomic potential is to provide an analytical or numerical expression to describe the energy landscape of a large particle system. Beyond the structural information of the system, the interatomic potential is considered a fundamental input in a numerical simulation [1, 4].

Having the interatomic potential and forces their origin at the subatomic level, the atom structure must be considered in the definition of a potential. Generally, most of the materials are characterized by different types of chemical interactions, which need to be taken into account in the definition of a force field:

- Covalent bonds, found in the C-C bonds of organic molecules, and occurring due to the overlap of electron orbitals.

- Metallic bonds, found in metals.
- Ionic bonds, also known as electrostatic or Coulomb interactions, typical of ceramic materials (*e.g.* Al_2O_3 or SiO_2).
- Hydrogen-bonds, found in water and in many polymers and proteins.
- van der Waals (vdW) interactions, also known as weak or dispersive intermolecular interactions.

To accurately describe the interatomic potential of a material, we need mathematical expressions to describe how the potential energy stored in a bond changes within the geometry and the position of atoms.

Various potentials with different accuracy levels have been developed and are available in the literature. The choice of the most appropriate potential strictly depends on the applications and on the material. Interatomic force fields are derived from quantum mechanics (QM) calculations (*i.e.* density functional theory methods - DFT) [6], semi-empirically (tight-binding potentials) [7], by using empirical values in quantum mechanics representation, or empirically, by considering the summation of the energy contributions associated with different types of bond interactions as given in Eq. 3.5:

$$U = U_{\text{Electrostatic}} + U_{\text{Covalent}} + U_{\text{vdW}} + U_{\text{H-bonds}} + \dots \quad (3.5)$$

Empirical and semi-empirical potentials are widely used for modeling the mechanical properties of materials, allowing to simulate large particle systems. The challenge is to find a proper mathematical expression to accurately approximate these terms for a specific material. Among the most common empirical potential there are: the pair potential, such as the Lennard-Jones [8], the simplest and least computational expensive potential, and the multibody potentials [9], such as the Embedded Atom Method (EAM), the reactive potentials, such as ReaxFF [10], and a class of potentials used for biological materials [11], such as CHARMM, AMBER, DREIDING, GROMOS, characterized by a similar description of the interatomic forces. Since a CHARMM-based force field is adopted in the simulations described in Chapters 4-5, a more detailed description is given below.

3.3.1.1 CHARMM force field

CHARMM force field is widely used to describe the behavior of biological materials and polymers, proteins in particular. This force field describes the energy landscape as a summation of different harmonic and anharmonic terms, representing the covalent, ionic, van der Waals and hydrogen-bonding interactions. The bonds between atoms are modeled by harmonic springs, hence all the bonds, except of H-bonds, cannot be broken and new bonds cannot be formed. Another approximation regards the charges, which are fixed, and the equilibrium angle, which does not depend on stretching. The mathematical formulation of the CHARMM force field is the following:

$$U_{\text{system}} = U_{\text{bond}} + U_{\text{angle}} + U_{\text{torsion}} + U_{\text{Coulomb}} + U_{\text{vdW}} + (U_{\text{H-bonds}}) \quad (3.6)$$

Most of the terms, in particular the first three in Eq. 3.6 describing the covalent bond interactions, are harmonic terms, hence valid for small deformation from the equilibriums configuration of the bond. The calculation of Coulomb interactions requires a computational effort,

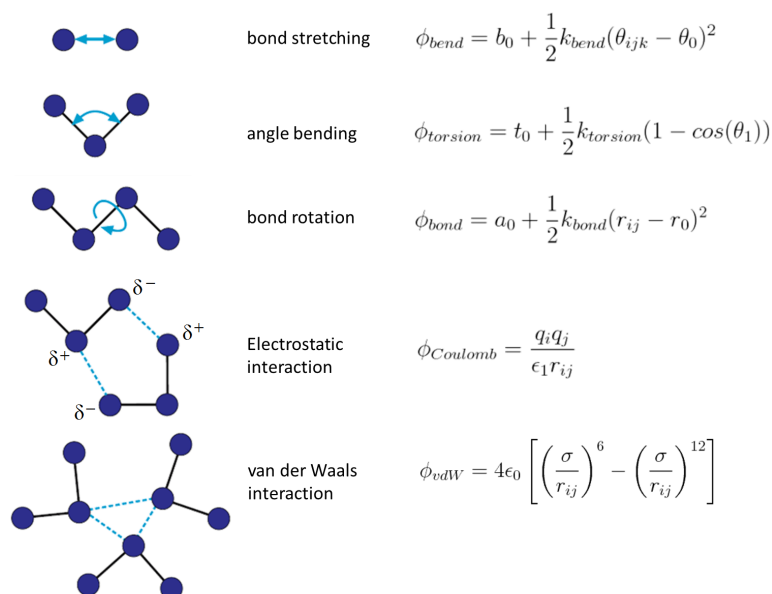


Figure 3.2: Schematic representation and mathematical formulation of each term included in the potential expression of the CHARMM force field (H-bonds are included in the vdW-terms) - adapted from [4].

being long range interactions. The vdW terms are modeled using Lennard-Jones 6-12 terms. H-bonds are often included in the vdW-terms. The main drawback of this potential is the limited transferability of the single terms expressions, being different for different chemistry. Indeed, chemistry is captured through atom typing, by assigning different tags to different atom types. This limits the transferability of the potential expression, but provides an accurate description of the energy landscape. Figure 3.2 shows a schematic representation and the mathematical formulation of each term included in the potential expression, given by Eq. 3.6.

The parameters in this force field are generally determined from quantum chemical simulation models by force field training. CHARMM and other force field for proteins also include simulation models to describe water molecules (*e.g.* TIP3P, TIP4P, SCP, SCP/E) [4].

3.3.2 Numerical Algorithms

Numerous numerical algorithms have been developed for integrating the equations of motion. Generally the criteria used to choose the most appropriate algorithm are the following: *i)* it should conserve energy and momentum, *ii)* it should be computationally efficient, *iii)* it should permit a long time step for integration [5]. The most common algorithms are: the Verlet algorithm, the Leap-Frog algorithm, the Velocity Verlet, and the Beeman's algorithm. The Leap-Frog and the Velocity Verlet are the most widely used in commercial MD codes [1, 4].

3.3.3 Thermodynamical Ensembles

An ensemble is a collection of all possible systems with different microscopic states but an identical macroscopic or thermodynamic state. There exist different ensembles with different characteristics.

Microcanonical ensemble (NVE). It represents a thermodynamic state characterized by a fixed number of atoms, N , a fixed volume, V , and a fixed energy, E .

Canonical Ensemble (NVT). The number of atoms, N , the system volume, V , and the temperature, T , remain constant during the simulation.

Isobaric-Isothermal Ensemble (NPT). It is characterized by a fixed number of atoms, N , a fixed pressure, P , and a fixed temperature, T .

Grand canonical Ensemble (μ VT). The thermodynamic state for this ensemble is characterized by a fixed chemical potential, μ , a fixed volume, V , and a fixed temperature, T .

Simple algorithms are used to modify the equations of motion to obtain a specific thermodynamic ensemble (*e.g.* by controlling the temperature by means of a thermostat (thermal bath), in the *NVT* case, or also the pressure, by means of a barostat, in the *NPT* case). During the integration of the equations of motion, molecular dynamics samples the microscopic configurations, providing a series of microscopic states, which corresponds, after an average procedure to the proper macroscopic state.

3.3.4 Energy Minimization

Energy minimization is an approach consisting in minimizing the potential energy of the system, by leading it to the zero temperature. From a physical point of view, it corresponds to the process of cooling down a material to the zero Kelvin. This process is generally performed at the beginning of a simulation, to get a stable structure before any loading or excitation are applied, or several times during a simulation to mimic a quasistatic experiment, though neglecting the effect of the temperature. During this minimization process, defect distribution in the material can be found.

Energy minimization can be performed through different algorithms. The most common are the conjugate gradient (CG) algorithm, which quickly converges, and the steepest descent algorithm, which does not converge as quickly as CG, but may be more robust in some situations.

3.3.5 Boundary conditions

The treatment of boundary conditions is a delicate issue in atomistic modeling. Indeed, due to the limited size of atomistic models, a large amount of atoms are located on the surface, hence having completely different surrounding conditions and forces from the bulk atoms. These surface effects are generally undesired when simulating a bulk material. To overcome this problem of surface effects, it is common to adopt periodic boundary conditions, which eliminate boundary effects, but have limitations in the simulation of nonequilibrium states. For nonequilibrium state problems instead, free or mixed boundary conditions are preferred [1].

Period boundary conditions (PBCs) allows a domain reduction and analysis of a representative substructures only. Particles in only one box are modeled explicitly, and the box is then replicated to infinity in all three Cartesian directions. Particles in all the boxes move simultaneously and each particle interacts with other particles in the box and with particles images in nearby boxes. In this case, interactions also occurs through the boundaries, and no surface effects occur. A schematic example of the concept of PBCs is given in Figure 3.3.

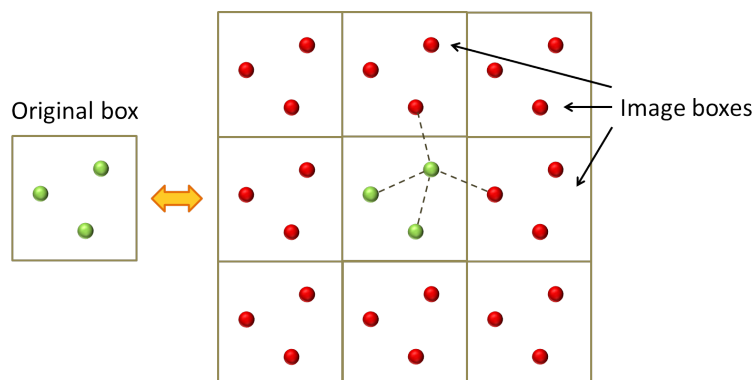


Figure 3.3: Schematic example of the concept of periodic boundary conditions.

Free boundary conditions instead, are used when studying surface phenomena. Fixed boundary conditions are used for uniaxial loading simulations or shearing problems, in which one boundary should be fixed to investigate the relative deformation.

3.3.6 Steered Molecular Dynamics

Steered molecular dynamics (SMD) simulations, or force probe simulations, is a particular type of MD, where forces are applied, generally to specific atoms of a protein, to deform its structure, by pulling it along desired degrees of freedom. These experiments can be used to reveal structural changes in a protein at the atomic level. SMD is often used to simulate particular phenomena such as mechanical unfolding or stretching [4].

Like experimental mechanical tests, SMD can be applied in two modes: force control, by applying a constant force, or velocity control, by applying a constant pulling velocity.

3.4 Parallel Computing

MD simulations require a significant computational effort. Indeed, the increase in computational power has largely contributed to the use of molecular dynamics tool to analyze small systems and structures. In particular, parallel computing has significantly reduced the computational time. Parallel computing consists in a large number of small computers working at the same time ("in parallel") on different parts of the same problem; information between these computers is then shared by message-passing-interface (MPI) procedures.

Parallel molecular dynamics is efficiently implemented in message-passing environment, thanks to effective developed algorithms to carry out the summation of N interacting particles. Generally, if the particle-particle interactions are short-ranged the computational burden can be reduced, so as to linearly scale the execution time with the number of particles. There are different classes of fast parallel algorithms. Plimpton described three classes of parallel algorithms, which are suitable for short-range MD force fields: so-called atom-, force-, and spatial-decomposition algorithms. Briefly, atom-decomposition methods assign a subset of atoms permanently to each processor, force-decomposition methods assign a subset of pairwise force computations to each processor, and spatial-decomposition methods assign a sub-region of the simulation box to each processor [12].

During the last years several programs were designed for parallel computers. Among them, those that are partly available free of charge are: Amber, CHARMM, NAMD, NWChem and

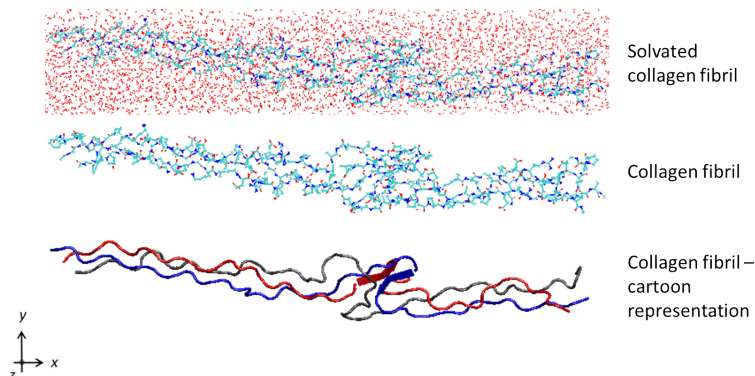


Figure 3.4: Different types of representation of a collagen fibril, plotted with VMD [14].

LAMMPS. In this thesis work, simulation are carried out using LAMMPS [13].

3.5 Post-processing Methods

Large-scale atomistic simulations produce a large amount (*i.e.* terabytes) of data. Therefore, it is necessary to have tools to handle and filter the data, allowing the user to interpret and understand the results of simulations.

Visualization softwares, allowing one to visualize complex structures and their evolution during a simulation, have revealed to be very useful tools for the post-processing. The most common visualization softwares are Visual Molecular Dynamics (VMD) [14] and AtomEye [15], enabling one to render complex molecular geometry with different color schemes. These programs are particularly useful for the visualization of organic structures, highlighting important structural features of biological molecules, hence providing a powerful key to understand complex dynamical process. An example of different graphical representations of the same protein is given in Figure 3.4.

3.6 Advantages and Limitations

The increasing interest toward nanomaterials and nanotechnology has pushed to study the mechanical properties of materials at nanoscale, leading to an increased use of nanomechanical testing, *in vivo*, *in vitro*, and *in silico*. The first two expressions are referred to experiments performed on living organisms and in laboratory, respectively, whereas the last refers to mechanical testing performed via computer simulations. *In silico* research is widely increasing in different science fields, since it is thought to have the potential to speed the rate of discovery, reducing the need for expensive lab work and, in biological cases, for time consuming clinical trials.

Molecular dynamics is one of the most accepted and diffused methods to perform *in silico* research, with the possibility of reaching very small scales (\AA -nm). This can be considered an advantage, but at the mean time a drawback as well, since it is sometimes very difficult to have an experimental comparison at such scales. Moreover MD allows to study deformation under high strain rate or extreme conditions, which are difficult to be simulated via other simulation techniques (*e.g.* finite element method, mesoscale dislocation dynamics).

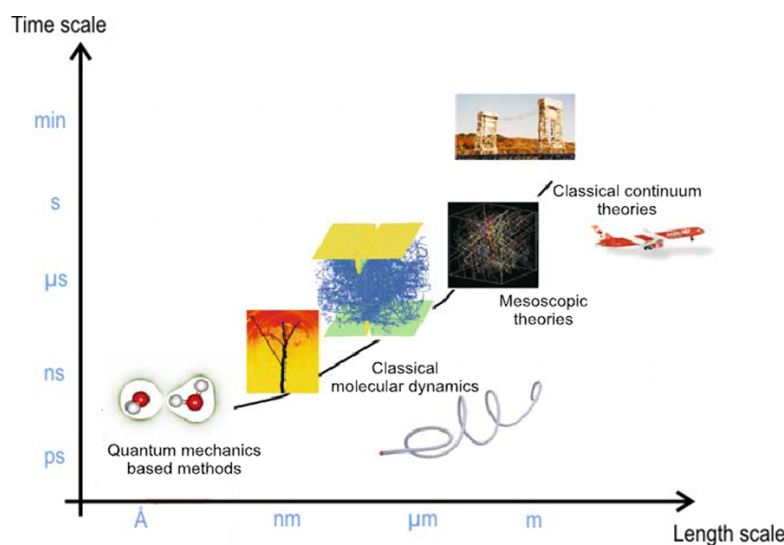


Figure 3.5: Simulation tools corresponding to different length- and- time scales [4].

The main drawbacks of molecular dynamics are related to the length and time-scale limitations, due to the computational tools available today. MD can be computationally intensive due to complexity of force field expressions, the large number of atoms belonging to the system to be simulated, and time-step where to perform numerical integration.

To model macroscopic dimensions of materials, we need to consider systems with size of approximately an Avogadro number of atoms (10^{23} atoms), which corresponds to 1 mole. However, the computational burden related to numerical simulations, data analysis, visualization and storage, can not be handled by the current computing systems. Hence, whether it is possible, simplified systems of thousands of atoms are studied.

Many materials phenomena are multi-scale phenomena; hence, to provide a fundamental understanding, simulations should capture the basic physics of single atoms, reaching scales of thousands of atomic layers by implementing the numerical models on large computational systems.

However, to provide a comprehensive description of the mechanical behavior of a specific material, different aspects and scale have to be investigated. This requires the use of different simulation approaches, appropriate for each specific length scale. An overview of different simulation tools corresponding to different length- and- time scales is given in Figure 3.5.

3.7 Applications

Molecular dynamics is used in many fields of science. Materials defects and structures have been subject of atomistic analyses for many years; in particular, the study of crystal defects and structural stability of many materials has a great importance in many technological fields. MD is also used to get an in-depth understanding of fracture mechanisms for many materials, considering the effects of size confinement and the crack speed propagation [16–19]. Surface and interface phenomena, such as surface roughening and diffusion, surface tension friction and adhesion, are also largely studied by means of MD [20, 21]. Those effects are particularly important for nanomaterials, characterized by a high surface-to-volume ratio. The study of aggregates made up of different kinds of atoms is of great technical significance for the design of

new alloys and different technological applications. The limited length scale makes it necessary to use a nanoscale simulation technique, such as the molecular dynamics, to determine the aggregate structure. MD can also be used to study macromolecules, such as proteins and nucleic acids (DNA, RNA), that are polymers made of covalently bonded small molecules or monomers (*i.e.* amino acids or nucleotides).

MD simulation can be used to study the biochemical and thermomechanical processes that affect the properties and functions of biological cells. It can be used to study the transportation processes of pharmaceutical molecules, which is important in the design of drug delivery systems. Indeed, numerical simulation may accelerate the research and development of new drugs, also reducing the costs.

MD simulation is also widely used in biomedicine and materials science, to study proteins (*e.g.* collagen, chitin, elastin) or biological materials (*e.g.* bone, spider silk) and to provide the basis for a bottom-up design of new biomaterials for tissue engineering.

Due to the large area of applicability of molecular dynamics, many simulation codes for molecular dynamics have been developed by many groups.

3.8 Outline

The idea of atomistic simulation is to simulate a system at atomistic scale from atomic interactions. This is necessary to get a deep understanding of the structure property relationship. For hierarchical materials, characterized by a specific organization at each length-scale, different techniques are used to get an insight into the structure property relationship. This is the case of bone, where both investigations of mechanical properties at the 'materials level' and at the 'structural level' are necessary to have a deep knowledge and to achieve a complete understanding of the mechanical properties of this material [22].

In the following chapters, we present a study of the bone material from the atomistic viewpoint. In Chapter 4 we carry out atomistic simulations to provide a fundamental description of the behavior of the bone building blocks, the HAP mineral platelets and collagen fibrous matrix. We also investigate, in Chapter 5, the effects of the characteristic nanosize on its mechanical behavior, and in particular on fracture behavior. The aim is to look into possible toughening mechanisms, acting at this scale, by studying the mechanical behavior of the bone atomistic structure, in view of a possible implementation into a new proposed bio-inspired design.

Bibliography

- [1] J. Fan, *Multiscale Analysis of Deformation and Failure of Materials*. Wiley, 2011.
- [2] B. J. Alder and T. E. Wainwright, “Studies in molecular dynamics. i. general method,” *The Journal of Chemical Physics*, vol. 31, no. 2, pp. 459–466, 1959.
- [3] A. Rahman, “Correlations in the motion of atoms in liquid argon,” *Physical Review*, vol. 136, no. 2A, pp. A405–A411, 1964. PR.
- [4] M. J. Buehler, *Atomistic Modeling of Materials Failure*. Springer US, 2008.
- [5] G. Sutmann, *Classical Molecular Dynamics*, pp. 211–254. Julich: NIC Series, 2002.
- [6] M. Springborg, *Density-functional methods in chemistry and materials science*. Wiley, 1997.
- [7] R. Car and M. Parrinello, “Unified approach for molecular dynamics and density-functional theory,” *Physical Review Letters*, vol. 55, no. 22, pp. 2471–2474, 1985. PRL.
- [8] P. Allen and D. Tildesley, *Computer simulation of liquids*. Clarendon Press, 1987.
- [9] M. W. Finnis and J. E. Sinclair, “A simple empirical n-body potential for transition metals,” *Philosophical Magazine A*, vol. 50, no. 1, pp. 45–55, 1984.
- [10] A. C. T. van Duin, S. Dasgupta, F. Lorant, and W. A. Goddard, “Reaxff: A reactive force field for hydrocarbons,” *The Journal of Physical Chemistry A*, vol. 105, no. 41, pp. 9396–9409, 2001.
- [11] A. D. Mackerell, “Empirical force fields for biological macromolecules: Overview and issues,” *Journal of Computational Chemistry*, vol. 25, no. 13, pp. 1584–1604, 2004.
- [12] S. Plimpton, “Fast parallel algorithms for short-range molecular dynamics,” *Journal of Computational Physics*, vol. 117, no. 1, pp. 1–19, 1995.
- [13] LAMMPS, “<http://lammps.sandia.gov>.”
- [14] W. Humphrey, A. Dalke, and K. Schulten, “Vmd: Visual molecular dynamics,” *Journal of Molecular Graphics*, vol. 14, no. 1, pp. 33–38, 1996.
- [15] J. Li, “Atomeye: an efficient atomistic configuration viewer,” *Modelling and Simulation in Materials Science and Engineering*, vol. 11, no. 2, p. 173, 2003.
- [16] M. J. Buehler, F. F. Abraham, and H. Gao, “Hyperelasticity governs dynamic fracture at a critical length scale,” *Nature*, vol. 426, no. 6963, pp. 141–146, 2003.
- [17] M. J. Buehler, H. Yao, H. Gao, and B. Ji, “Cracking and adhesion at small scales: atomistic and continuum studies of flaw tolerant nanostructures,” *Modelling and Simulation in Materials Science and Engineering*, vol. 14, no. 5, p. 799, 2006.
- [18] D. K. Dubey and V. Tomar, “Microstructure dependent dynamic fracture analyses of trabecular bone based on nascent bone atomistic simulations,” *Mechanics Research Communications*, vol. 35, no. 1-2, pp. 24–31, 2008.

- [19] T. Zhang, X. Li, S. Kadkhodaei, and H. Gao, “Flaw insensitive fracture in nanocrystalline graphene,” *Nano Letters*, vol. 12, no. 9, pp. 4605–4610, 2012.
- [20] Q.-X. Pei, Y.-W. Zhang, and V. B. Shenoy, “Mechanical properties of methyl functionalized graphene: a molecular dynamics study,” *Nanotechnology*, vol. 21, no. 11, p. 115709, 2010.
- [21] Z. Qin, A. Gautieri, A. Nair, H. Inbar, and M. J. Buehler, “Thickness of hydroxyapatite nanocrystal controls mechanical properties of the collagen-hydroxyapatite interface,” *Langmuir*, vol. 28, no. 4, pp. 1982–1992, 2012.
- [22] J. Y. Rho, L. Kuhn-Spearing, and P. Zioupos, “Mechanical properties and the hierarchical structure of bone,” *Medical Engineering & Physics*, vol. 20, no. 2, pp. 92–102, 1998.

Chapter 4

Atomistic Modeling of Collagen-Hydroxyapatite Nanocomposites

This chapter discusses the mechanical behavior of collagen-hydroxyapatite nanocomposites from an atomistic perspective. The aim is to define the key mechanisms, governing the interaction between the two components, and affecting the global behavior of the composite system. This study is carried out with a molecular dynamics approach, a method widely used for the analysis of small-scale systems, allowing a thorough understanding of the mechanics of hierarchical materials from the bottom up. In particular, this chapter is focused on the mechanics of collagen-hydroxyapatite nanocomposites under shearing loading, to understand which are the mechanisms and the factors responsible of the remarkable behavior of such materials.

4.1 Introduction

The research and technology is emerging now to understand the mechanisms governing the remarkable mechanical properties of natural materials, by modeling across scales, relating the basic mechanisms of the fundamental features that compose natural composites, such as bone, to the functionality and development of large-scale tissues and materials.

Collagen and hydroxyapatite are the main building blocks of bone and of the most common type of biomineralized materials [1–5]. The small scale phenomena, governing the mechanics of bone and bone-like materials at nanoscale, have significant effects on the large scale behavior these materials [3]. In particular, toughness, which is a fundamental property of natural composites, has been shown to be linked across multiple length scales [6], and associated to different mechanisms, characteristic of each hierarchical level, contributing to the overall mechanical response. The mechanical properties of bone are also related to the characteristic size of its main features at different hierarchical levels. In particular at small scale, the confined size of its building blocks has been shown to lead to higher mechanical properties [7]. Although bone has been largely studied in the literature, the behavior of collagen-HAP nanocomposite is still object of research. Models have been developed in the literature, to describe the load transfer, between the collagen and the matrix; for instance, the tension-shear model, where the mineral platelets carry most of the tensile load and the protein matrix transfers the load between the platelets by shear [8–13]. However, the interactions at the protein-mineral interface are still object of study. In particular, the molecular scale interactions between the collagen and the HAP, which control

the deformation and the load response of the whole system are still not clear. It has been shown that an important role in enhancing these interactions is played by the platelet shape of the HAP, characterized by a high surface to volume ratio, ensuring a large interface area with the collagen protein and improved mechanical properties [14–16]. Also, weak intermolecular bonds at interface (*i.e.* hydrogen bonds and van der Waals interactions) are thought to have a key function in deformation response; indeed, they continuously break and reform, allowing molecular slip, thus collagen-hydroxyapatite to be deformed as an integrated system under stress.

Full atomistic techniques have been shown to be essential for understanding such nanoscale mechanisms, though limitations in computational power restrict their applicability to meso and macroscale phenomena, where other techniques, often relying on atomistic information, are used (*i.e.* coarse grain modeling).

Breakthroughs in science, and in particular in biomimetic research, might come from emulating such nanoscale systems in nature; hence, is it interesting to see how those breakthroughs might come back to change the ways we design and engineer new materials. In this chapter, we present a full atomistic study of a simplified collagen-hydroxyapatite nanocomposite, to investigate how the two components interact and deform under loading, and to define the mechanisms responsible of the remarkable mechanical properties of this hierarchy, in view of mimicking such mechanisms in the design of a *de-novo* biomimetic material.

4.2 Background

4.2.1 Collagen-Hydroxyapatite Nanocomposites

Bone is generally considered a composite material, made of brittle mineral crystals of hydroxyapatite (HAP) embedded in an organic collagen matrix, hence showing intermediate properties between the two components. The mechanical properties of such nanocomposite system have been shown to be affected by several factors: mineral content [13], mineral thickness [17], mineral platelet shape [14–16], microporosity [13], and mineral-protein arrangement [18]. Indeed, mineral content and microporosity are two complementary concepts generally defined through BMD (bone mineral density), which is the most common parameter to define bone quality. In particular, the considerable toughness of bone and bone nanocomposites, has been shown to be due to the multiple energy absorbing mechanisms, occurring at the interface [10, 19]. According to the literature, the interface region is strictly dependent on the platelet shape [14–16] and collagen-HAP arrangement [18], both ensuring a maximum interface area. Molecular mechanisms, which characterize the mineral-polymer interactions in bone nanocomposites, have been investigated by Bhowmik *et al.* [20], by steered molecular dynamics simulation. Using the same molecular dynamics approach, Bhowmik *et al.* also investigate the influence of the interfacial interactions between the bone organic and mineral phases on the bone mechanical behavior, and the role played by water in these interactions, and in turn on the bone mechanical response.

From large literature studies it results that a crucial role in the collagen-hydroxyapatite composite behavior is played by the adhesion forces between the mineral and the protein; which are weak enough to allow slip under large load, preventing failure of the collagen backbone, but also strong enough to provide considerable strength and toughness.

Table 4.1 summarizes some mechanical properties of collagen, HAP, and collagen-HAP nanocomposites from literature experiments and simulations.

Table 4.1: Mechanical properties of collagen, HAP, and collagen-HAP nanocomposites from literature experiments and simulations.

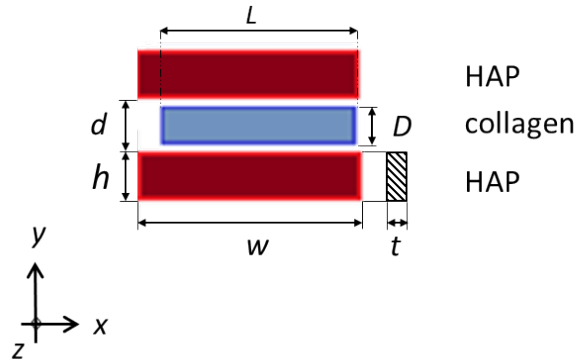
Material	Test method	Tensile modulus (GPa)	Extensibility (%)	Tensile strength (GPa)
Tropocollagen molecule	experiment [21]	0.35-12	30	
Tropocollagen molecule	simulation [22]	1.8-4	50	13
HAP	experiment [23]	114		
HAP	simulation [24]	120.6	10-16	7.4-9.6
HAP-collagen nanocomposite	simulation [17]	30.16-31.87		19.37-21.41

4.3 Materials and Methods

4.3.1 Atomistic Model

The model is a composite sandwich model consisting of two outer layers of HAP and one internal layer of collagen matrix. The two slabs of hydroxyapatite are aligned with the c -axes of the HAP crystal (*i.e.* along the [100] direction) parallel to the collagen main axis; the HAP basal plane (001) corresponds to the x - y plane. For HAP we consider a hexagonal (HCP) crystal, with $x = [100]$, $y = [010]$, and $z = [001]$. The two HAP layers have the same geometry and dimensions: width $w \approx 19.2$ nm, height $h \approx 1.6$ nm and out-of-plane thickness $t \approx 2.8$ nm. The collagen fibril has a diameter $D \approx 1.5$ nm and length $L \approx 14.9$ nm. All the above mentioned parameters are kept fixed during all the simulations. The y -distance between the two layers of HAP, from now on called 'interlayer distance', is variable. The values of interlayer distance are clearly indicated in Table 4.2. Figure 4.1 shows the model with parameters such as height, width, thickness, diameter, length, and interlayer distance; a snapshot of a sandwich structure is given in Figure 4.2, with the structure of the basic features highlighted.

The computational model is designed to shed light on the general behavior and deformation of a composite system containing a single tropocollagen molecule and two crystals of hydroxyapatite; hence, it is meant to be simple and not an accurate representation of the actual bone nanostructure. However, it allows us to perform a systematic study of bone nanomechanics from a fundamental point of view.

**Figure 4.1:** Geometry and dimensions of the sandwich models used for steered molecular dynamics simulations.

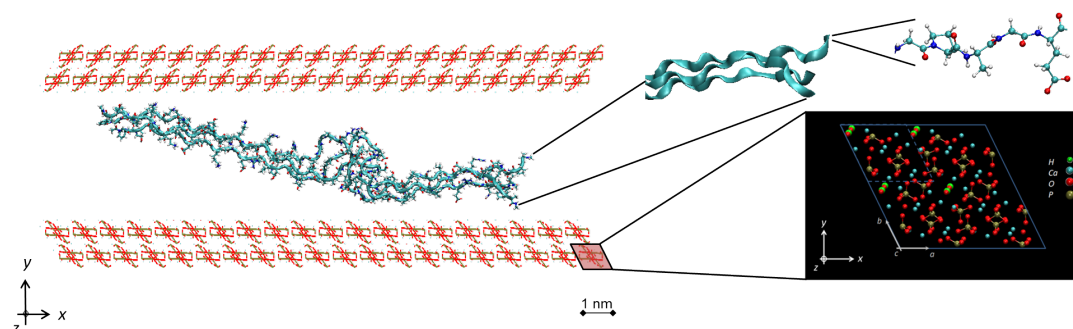


Figure 4.2: Snapshot of the sandwich model, showing the basic structures of the collagen molecule and the HAP unit cell.

4.3.2 Crystal Geometry

We generate the hydroxyapatite crystal unit cell by using Materials Studio 4.4 (Accelrys, Inc.). It is a hexagonal unit cell (HCP lattice) with 44 atoms and the following lattice parameters: $a = 9.4214 \text{ \AA}$, $b = 9.4214 \text{ \AA}$, $c = 6.8814 \text{ \AA}$, $\alpha = 90^\circ$, $\beta = 90^\circ$, $\gamma = 120^\circ$ [17]. The samples are created by replicating the unit cell 20 times in the x directions, two times in the y direction, and four times in the z directions. We focus on the interaction with the (010) plane, which is the most common in the morphology of biological materials due to the collagen-driven growing effect during the biomineralization process. Also, it has electrostatic characteristics on its surfaces, showing a negative charge on the OH-rich surface and a positive charge on the Ca-rich surface; (100) is the most stable and has geometrical and chemical similarity to the (010) plane, whereas the (001) is neutral [17,25,26]. A more detailed description of the HAP crystal is given in 5. In this study we consider the interaction between the collagen and the OH-rich surface of the (010) plane, as it ensures a stronger adhesion than the Ca-rich one [17]. This is due to OH-groups, which provide more donors and acceptors for the H-bond formation with the collagen protein.

4.3.3 Protein Model

We use collagen molecules, previously equilibrated by Chang *et al.* (40 ns *NPT* equilibrium) [27,28]. To generate the collagen molecules, the authors used the real sequences of type I α -1 and type I α -2 chains of *mus musculus* (wild type mouse), taken from the National Center for Biotechnology Information protein database (<http://www.ncbi.nlm.nih.gov/protein>). The collagen molecule (*i.e.* heterotrimer) includes two α -1 chains and one α -2 chain. The entire α -1 and α -2 chains consist of 1014 residues with repeated G-X-Y triplets, excluding the C-terminal and N-terminal sequences. To reduce the computational costs, a specific section with a length of 57 residues (from the 403rd to 459th residues) is considered to generate the heterotrimer collagen molecule, ensuring that the amino acid composition (by %) of the segment is similar to the composition of the complete collagen molecule. The sequence of the modeled segment is given in [27]. The collagen molecules are created by inputting the sequences of three chains into the software THEBuScr (Triple-Helical collagen Building Script) [29], which allows one to build a triple-helical molecule, consisting of three staggered chains, based on any specified amino acid sequence.

4.3.4 Hydroxyapatite Force Field Parametrization

We use an extended CHARMM force field as reported in [17], where the authors included the parameters - derived from quantum mechanics calculations [30] - for hydroxyproline (HYP), a nonstandard amino acid typical of collagen and not present in other proteins, and added non-bonded parameters, calculated by using a Born-Mayer-Huggins model [14,31]. The bond, angle and dihedral parameters are based on quantum-mechanics calculations and experimental data. The force field has been validated in earlier works [14, 17, 18, 31, 32]. The choice of adopting this force field is motivated by the fact that it has been shown to correctly model the behavior of collagen and HAP-collagen systems.

4.3.5 Steered Molecular Dynamics Simulations

We perform steered molecular dynamics (SMD) simulations by using the LAMMPS code [33]. We use a modified CHARMM force field to describe the overall strain energy of the system: Lennard-Jones and Coulombic interactions are computed with an additional switching function that ramps the energy and force smoothly to zero between an inner (8 Å) and outer cutoff (10 Å) [33]. This cutoff range is selected to include one unit lattice over the thickness. An additional $1/r$ term is also included in the Coulombic formula, making the Coulombic energy varying as $1/r^2$, which is an effective distance-dielectric term. This represents a simple model for an implicit solvent with additional screening and it is designed to be used in simulations of biomolecules without explicit water solvent [33]. We also investigate the effect of water. In this case, we use the VMD software [34] to solvate the structure, including it in a larger water box of TIP3 water molecules. The structure in explicit solvent is then included in a large simulation box with fixed (non-periodic) boundary conditions.

The model is geometrically optimized through energy minimization, by using two different algorithms, the conjugate gradient and the steepest descent methods. Afterwards we clamp the left edge of the bottom HAP layer and relax the structure under an *NVE* ensemble for 2 ns. We use a Langevin thermostat to set the temperature to 300 K. Once the structure is fully relaxed (confirmed through the root-mean square deviation convergence to a constant value), we perform SMD simulations: we constraint the left edges of the two HAP layers and apply load to the right-end part of the collagen, by pulling the center of mass of the terminal α -carbon atoms of the tropocollagen molecule via a virtual spring, with an elastic constant $k_{spring} = 8000 \text{ kJ}\cdot\text{mol}^{-1}\cdot\text{nm}^{-2}$. The pulling velocity is set to 0.01 Å/ps (1 m/s), similar to that used in previous studies [17,35]. The simulation setup is given in Figure 4.3a. To investigate the effects of pulling speed, we perform additional simulations by applying the load at velocities of 1 Å/ps (100 m/s). A time step of 0.5 fs is used in all dynamical simulations. The final solvated system contains ≈ 50000 atoms (with a water box of size of 25.5 nm · 9.3 nm · 3.9 nm).

To investigate the effect of confinement on the mechanics of HAP-collagen nanocomposites, we build a confined structure with a reduced initial interlayer distance. Then, after relaxing the systems under an *NVE* ensemble for 2 ns, and leading to 300 K, by using a Langevin thermostat, we compact the structure by moving down the HAP top layer, with a velocity of 1 (m/s); then we apply the load, as described above for the other structures. Also in the confined case we perform simulations both in dry and wet cases. The simulation setup for the confined case is given in Figure 4.3b. The final solvated system contains ≈ 60000 atoms (with a water box of size of 25.8 nm · 7.8 nm · 5.2 nm).

All the simulations are carried out on the FERMI supercomputing system of CINECA (Italy), a new system based on IBM BG/Q architecture. A sample input script for LAMMPS is

given in Appendix A, while a sample script for atom definition is shown in Appendix B.

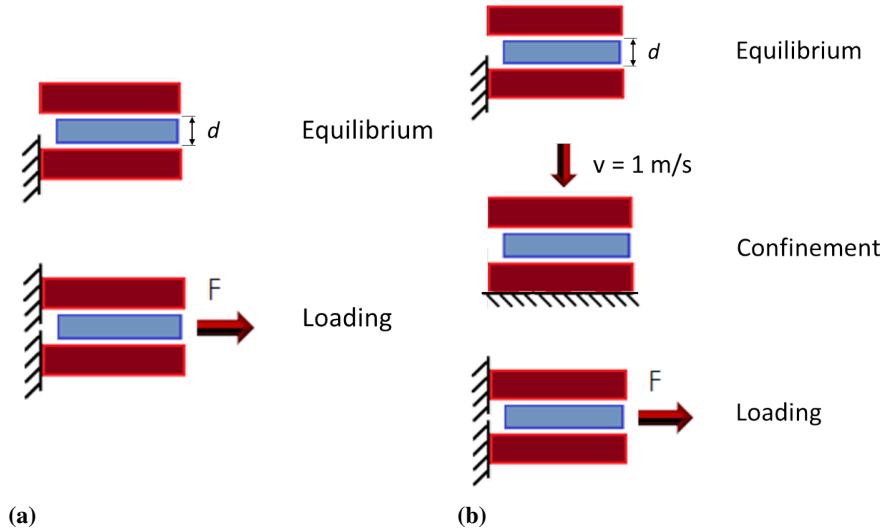


Figure 4.3: Simulation setup. (a) Simulation scheme followed for the initial case: boundary and loading conditions during the equilibrium and loading phase. (b) Simulation scheme followed for the confined case: boundary and loading conditions during the equilibrium, the confinement and the stretching phase.

4.3.6 Data Post-processing

For the analysis of the data we use the software Visual Molecular Dynamics (VMD) [34], to visualize the simulation trend, to print the snapshots of the tests, and to compute the H-bonds. We count the hydrogen bonds within a donor-acceptor distance of 3.5 Å and an angle cutoff of 30°. To analyze the mechanical response of the composite system under the applied loading conditions, we use MATLAB (Mathworks, Inc.). We use force-displacement data to determine the mechanical properties (*i.e.* stiffness, maximum force, tensile and shear strength *etc.*). The displacement is calculated as the shift of the SMD loading point dx . The stiffness is calculated by using a linear fitting to the force-displacement data, in the initial linear region. The tensile strength is calculated as the maximum force recorded during a simulation, divided by the collagen cross-section. This value may be representative of the strength of a collagen fibril, with the effect of the side HAPs, result that can be directly compared with those calculated by Qin *et al.* in [17]; also, this value might be correlated with the strength of a mineralized collagen fibril. Moreover, by considering the loading conditions of the performed *in silico* shear tests similar to the case of a double lap joint subjected to tensile loading, as described by the standard [36], we calculate the shear strength as defined in [36]: maximum force divided by the overlap area. We calculate the overlap area by considering the projection of the collagen (approximate to a cylinder) on the HAP layers.

4.4 Results

Figure 4.4 shows the final equilibrated structures, before and after the 'compression' phase. The confined structures have an interlayer distance of 25% and 40% less than the initial one, in vacuum and water cases respectively. The values of interlayer distance are given in Table 4.2, along with the mechanical properties determined from the simulations.

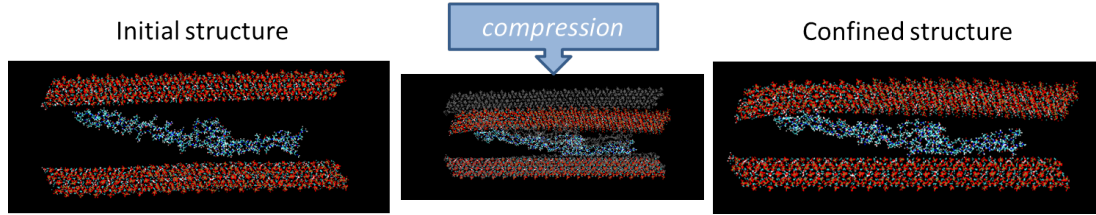


Figure 4.4: Snapshots of the initial structure (left), after equilibrium, and the confined one (right), after "compression". The central snapshot represents the confinement phase: the HAP top layer before confinement is represented in gray color, whereas the same layer after confinement is shown in red color.

Table 4.2: Geometric and mechanical properties of HAP-collagen nanocomposites determined from the simulations described in Section 4.3.5.

Structure	Condition	Interlayer distance (nm)	Test method	Maximum force (N) $\cdot 10^{-8}$	Tensile strength (GPa)	Shear strength (GPa)	Stiffness (N/m)
Initial	Dry	2.6	Shear test	5.91	33.42	0.81	3.48
Initial	Water	4.1	Shear test	6.81	38.56	0.93	3.81
Confined	Dry	1.9	Shear test	7.60	42.99	1.04	4.95
Confined	Water	2.5	Shear test	7.20	40.76	0.98	5.13

We calculate the tensile strength (given in Table 4.2) to have a direct comparison with the results (also given in Table 4.1) of the simulations in [17], where a system similar to a single lap joint is studied. The results show a direct stiffening effect, given by the second layer of HAP, and leading to an increase in strength, which is twice the value calculated in [17].

The force-displacement curves resulting from the simulations are given in Figure 4.6 and Figure 4.7, also showing the effect of solvent and the effect of confinement, respectively. The curves are characterized by an initial linear region, and a following 'bumpy' region until failure occurs. Deformation mechanisms, occurring during simulations, includes three phases:

1. The first, characterized by the atomic interactions (*i.e.* electrostatic, vdW, and H-bonds interactions) between the collagen chains and between the chains and the HAP surface. In this phase, the deformation is mainly due to the stretching of the intermolecular bonds between the chains, with a likely breakage of the cross-links between chains.
2. Then, chain unfolding and uncoiling occurs with the breakage of intermolecular vdW bond and H-bonds, which initially stabilize the collagen triple helical structure.
3. Finally chains start sliding on the HAP surfaces, in a discontinuous way owing to the progressive breakage of H-bonds, which serve as 'sacrificial bonds', increasing the en-

ergy dissipation before the failure the backbone of the macromolecules and of the entire structure occurs.

Snapshots of the above mentioned deformation mechanisms are shown in Figure 4.5. The

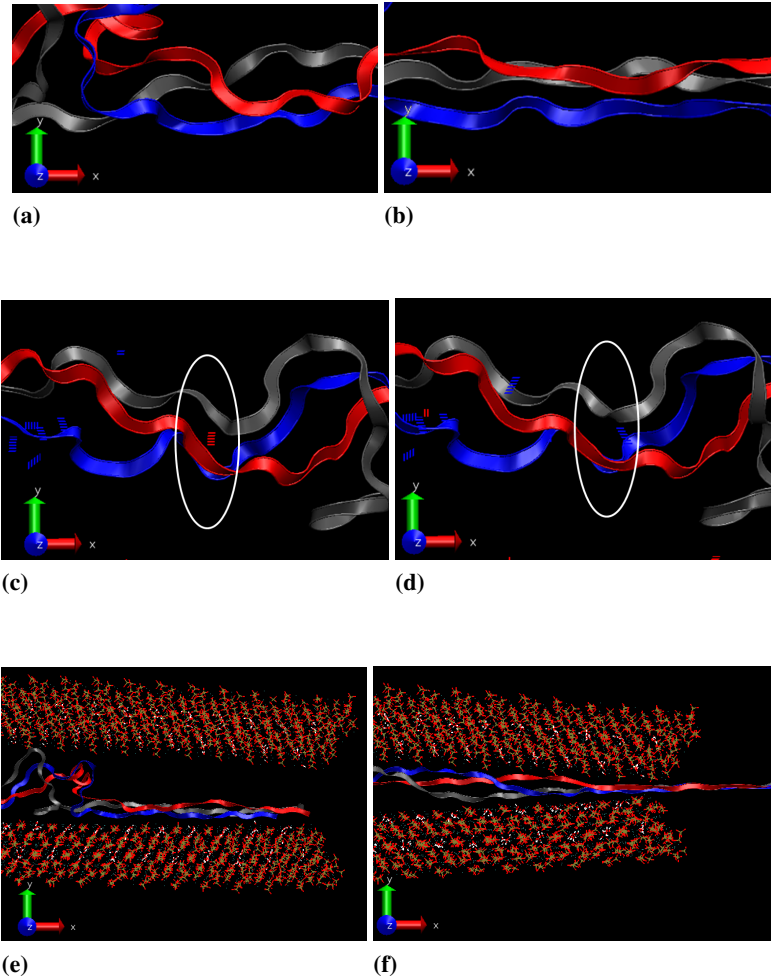


Figure 4.5: Snapshots showing various mechanisms of deformation during the tests. (a)-(b) Chain unfolding. (c)-(d) Hydrogen bond formation and breaking (in the first snapshot, panel (c), H-bond is highlighted with red lines; in the second snapshot corresponding to the following frame, panel (d), the previous H-bond is broken and a new one, highlighted with blue line, is formed. (e)-(f) Chain sliding and stretching.

mechanism of sacrificial bonds is one of the key toughening mechanisms of bone nanocomposites and is largely described in the literature [6, 37–39]. Figure 4.8 shows the trends of the number of H-bonds during the simulations for all the studied cases. The plots show the density of H-bond (*i.e.* number of H-bonds normalized on the equilibrated length of the tropocollagen molecule) with respect to the shear displacement during the tests. Both the intramolecular (*i.e.* between the tropocollagen chains), Figure 4.8a-4.8c, and intermolecular (*i.e.* between the tropocollagen chains and the HAP surface) H-bonds, Figure 4.8b-4.8d, are shown. We observe a decreasing number of intramolecular H-bonds, due to unfolding and uncoiling of collagen

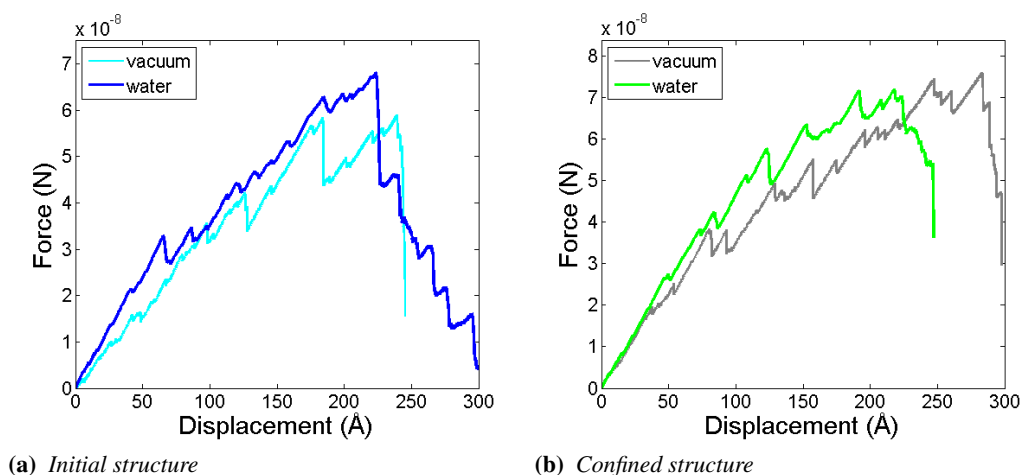


Figure 4.6: Force-displacement. (a) Comparison between the vacuum and the solvated case: initial structure. (b) Comparison between the vacuum and the solvated case: confined structure.

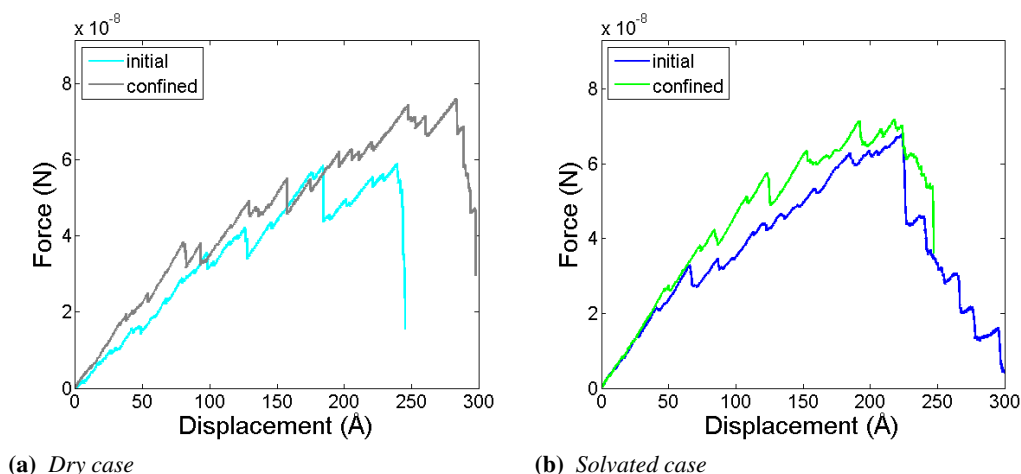


Figure 4.7: Force-displacement. (a) Comparison between the initial structure and the confined one: vacuum case. (b) Comparison between the initial structure and the confined one: solvated case.

chains, via intramolecular H-bonds breaking, followed by chain stretching and alignment in the load direction (see Figure 4.8a-4.8c). The difference between the number of H-bonds relative to the initial linear region, in the force-displacement curve, and the second bumpy region is significant. The trends for vacuum and water cases, and for initial and confined structures, are similar.

In Figure 4.8b we observe an initial increasing number of intermolecular H-bonds, followed by a bumpy region. These bonds contribute to the interaction force. By comparing the graphs in Figure 4.8a and Figure 4.8b, we can better explain the deformation mechanisms as follows,

confirming what is stated above: initially chain unfolding and uncoiling, via H-bonds occur; then, continuous H-bonds formation and breaking (*i.e.* sacrificial bonds) between the collagen and the HAP surface take place, increasing the energy required to failure; this corresponds to the bumpy region, in the force-displacement graph (*i.e.* for displacements larger than 100 Å). This trend is clear for the dry case, given in Figure 4.8b, but in solvated case; in the latter, the deformation mechanism, observed through the software VMD, is similar, but less clear from the graph in Figure 4.8d, due to the H-bond formation with water molecules as well. Indeed, the presence of water, which interacts with both collagen and HAP, reduces the direct coupling between the protein and the mineral. This concept has also been shown in previous studies [19].

We investigate the effect of water on the global mechanical properties, as it gives a more realistic perspective of the mechanics of such nanocomposites, being water one of the fundamental components of bone. The principal effect of water is to increase the mechanochemical properties. This is due to the interaction of both the collagen and the HAP with the water molecules. Results are summarized in Table 4.2 and graphically shown in Figure 4.6.

The effect of confinement is also studied, showing an improved overall mechanical behavior, in terms of stiffness and strength, as the interlayer distance is reduced (see Figure 4.7). This is due to the stronger interactions (*e.g.* higher number of H-bonds) between the protein and the mineral (see Figure 4.8). In the the studied cases, and in particular in the confined ones, large interactions between the collagen and both the HAP surfaces occur, owing to 'kinking configuration' of the collagen (heterotrimer), which allows interactions with both top and bottom surfaces.

We also carry out additional simulations (with a pulling velocity of 1 Å/ps (100 m/s)) to study the effects of pulling speed. As expected, we find a stiffening effect, leading to a more brittle system; hence, we conclude that the adhesion strength is highly sensitive to the pulling rate.

In all the cases, failure occurs by breaking the tropocollagen molecule, being the weakest component, instead of interface failure. This is important for understanding the rupture mechanisms in bone-like composites.

4.5 Remarks

In this chapter, we present a study of collagen-hydroxyapatite nanocomposites, from a fundamental point of view. We find that the presence of water, which mediates the interactions between the protein and the mineral acting as a lubricant, increases the interface shearing properties and the overall mechanical performance of the composite system. Also, the size effect significantly increases the performance of the whole structure. Indeed, according to previous studies [7, 38], it is not only the building blocks that make bone so resilient. At an atomistic and molecular scale, the size effect plays a main role in determining the mechanical behavior of bone, leading to new phenomena, which do not occur at larger levels.

Another important result of this study is the crucial role played by the intermolecular hydrogen bonds, in determining the resistance against slip. These bonds, present both in the collagen helix and between the collagen and the hydroxyapatite, act as sacrificial bonds, and their continuous formation and breaking, acting as an energy dissipation medium, lead to an increase in the composite toughness.

Our results may provide details on the mechanism of load transmission inside collagen fibrils and fibers, and mineralized tissues, which is essential for the development of constitutive

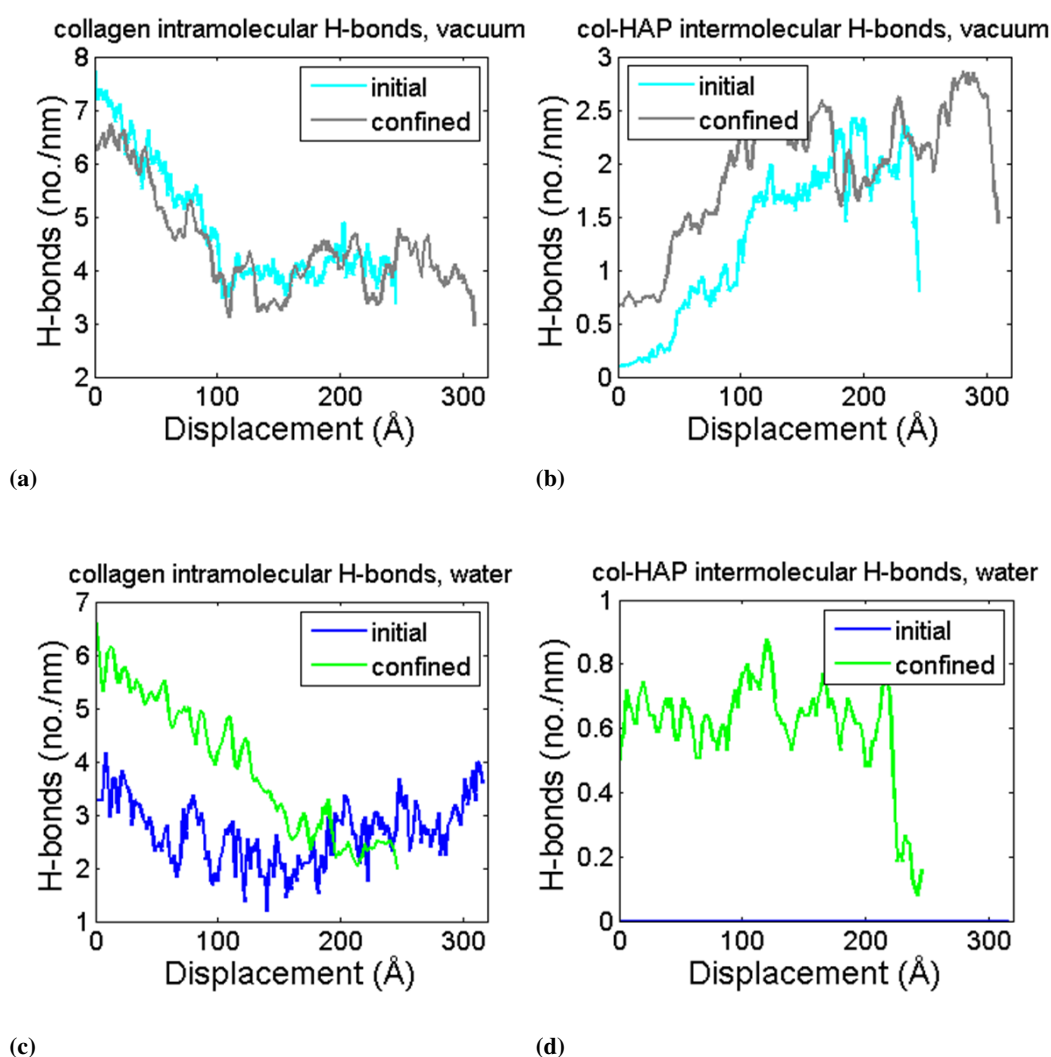


Figure 4.8: Number of hydrogen bonds during the tests. (a) Number of intramolecular H-bonds as a function of the displacement in dry condition for both initial and confined structures. (b) Number of intermolecular H-bonds as a function of the displacement in dry condition for both initial and confined structures. (c) Number of intramolecular H-bonds as a function of the displacement in solvated condition for both initial and confined structures. (d) Number of intermolecular H-bonds as a function of the displacement in solvated condition for both initial and confined structures.

models of collagenous tissues at larger hierarchical levels. Moreover, these models might have many applications, ranging from tissue engineering studies to the development of bio-inspired materials.

In this study, the understanding of the mechanisms and the nature's secrets governing the interaction and the behavior of collagen-hydroxyapatite nanocomposites can shed light in the design of the bone-inspired composite presented in Chapter 6-7, leading to an improvement in the initial proposed design.

Bibliography

- [1] P. Fratzl, H. S. Gupta, E. P. Paschalis, and P. Roschger, "Structure and mechanical quality of the collagen-mineral nano-composite in bone," *Journal of Materials Chemistry*, vol. 14, no. 14, pp. 2115–2123, 2004.
- [2] L. C. Wu, J. Yang, and J. Kopecek, "Hybrid hydrogels self-assembled from graft copolymers containing complementary beta-sheets as hydroxyapatite nucleation scaffolds," *Biomaterials*, vol. 32, no. 23, pp. 5341–53, 2011.
- [3] D. Sen and M. J. Buehler, "Structural hierarchies define toughness and defect-tolerance despite simple and mechanically inferior brittle building blocks," *Scientific Reports*, vol. 1, 2011.
- [4] B. Alexander, T. L. Daulton, G. M. Genin, J. Lipner, J. D. Pasteris, B. Wopenka, and S. Thomopoulos, "The nanometre-scale physiology of bone: steric modelling and scanning transmission electron microscopy of collagen-mineral structure," *Journal of the Royal Society Interface*, vol. 9, no. 73, pp. 1774–86, 2012.
- [5] E. Hamed and I. Jasiuk, "Elastic modeling of bone at nanostructural level," *Materials Science and Engineering: R: Reports*, vol. 73, no. 3-4, pp. 27–49, 2012.
- [6] M. E. Launey, M. J. Buehler, and R. O. Ritchie, "On the mechanistic origins of toughness in bone," *Annual Review of Materials Research*, vol. 40, no. 1, pp. 25–53, 2010.
- [7] H. Gao, B. Ji, I. Jager, E. Arzt, and P. Fratzl, "Materials become insensitive to flaws at nanoscale: Lessons from nature," *Proceedings of the National Academy of Sciences*, vol. 100, no. 10, pp. 5597–5600, 2003.
- [8] H. Gao, *Application of fracture mechanics concepts to hierarchical biomechanics of bone and bone-like materials Advances in Fracture Research*, pp. 101–137. Springer Netherlands, 2006.
- [9] M. J. Buehler, H. Yao, H. Gao, and B. Ji, "Cracking and adhesion at small scales: atomistic and continuum studies of flaw tolerant nanostructures," *Modelling and Simulation in Materials Science and Engineering*, vol. 14, no. 5, p. 799, 2006.
- [10] H. S. Gupta, W. Wagermaier, G. A. Zickler, D. Raz-Ben Aroush, S. S. Funari, P. Roschger, H. D. Wagner, and P. Fratzl, "Nanoscale deformation mechanisms in bone," *Nano Letters*, vol. 5, no. 10, pp. 2108–2111, 2005.
- [11] B. Ji and H. Gao, "Mechanical properties of nanostructure of biological materials," *Journal of the Mechanics and Physics of Solids*, vol. 52, no. 9, pp. 1963–1990, 2004.
- [12] B. Ji and H. Gao, "A study of fracture mechanisms in biological nano-composites via the virtual internal bond model," *Materials Science and Engineering: A*, vol. 366, no. 1, pp. 96–103, 2004.
- [13] S. P. Kotha and N. Guzelsu, "Tensile behavior of cortical bone: Dependence of organic matrix material properties on bone mineral content," *Journal of Biomechanics*, vol. 40, no. 1, pp. 36–45, 2007.

- [14] R. Bhowmik, K. S. Katti, and D. Katti, "Molecular dynamics simulation of hydroxyapatite-polyacrylic acid interfaces," *Polymer*, vol. 48, no. 2, pp. 664–674, 2007.
- [15] D. Dubey and V. Tomar, "Role of molecular level interfacial forces in hard biomaterial mechanics: A review," *Annals of Biomedical Engineering*, vol. 38, no. 6, pp. 2040–2055, 2010.
- [16] D. K. Dubey and V. Tomar, "Understanding the influence of structural hierarchy and its coupling with chemical environment on the strength of idealized tropocollagen-hydroxyapatite biomaterials," *Journal of the Mechanics and Physics of Solids*, vol. 57, no. 10, pp. 1702–1717, 2009.
- [17] Z. Qin, A. Gautieri, A. Nair, H. Inbar, and M. J. Buehler, "Thickness of hydroxyapatite nanocrystal controls mechanical properties of the collagen-hydroxyapatite interface," *Langmuir*, vol. 28, no. 4, pp. 1982–1992, 2012.
- [18] D. K. Dubey and V. Tomar, "Role of the nanoscale interfacial arrangement in mechanical strength of tropocollagen-hydroxyapatite-based hard biomaterials," *Acta Biomaterialia*, vol. 5, no. 7, pp. 2704–2716, 2009.
- [19] H. Gupta, J. Seto, W. Wagermaier, P. Zaslansky, P. Boesecke, and P. Fratzl, "Cooperative deformation of mineral and collagen in bone at the nanoscale," *Proceedings of the National Academy of Sciences*, vol. 103, p. 17741, 2006.
- [20] R. Bhowmik, K. S. Katti, and D. R. Katti, "Influence of mineral-polymer interactions on molecular mechanics of polymer in composite bone biomaterials," *MRS Online Proceedings Library*, vol. 978, 2006.
- [21] Y.-L. Sun, Z.-P. Luo, A. Fertala, and K.-N. An, "Stretching type ii collagen with optical tweezers," *Journal of Biomechanics*, vol. 37, no. 11, pp. 1665–1669, 2004.
- [22] M. Buehler, "Atomistic and continuum modeling of mechanical properties of collagen: elasticity, fracture, and self-assembly," *Journal of Materials Research*, vol. 21, no. 8, pp. 1947–1961, 2006.
- [23] R. S. Gilmore and J. L. Katz, "Elastic properties of apatites," *Journal of Materials Science*, vol. 17, no. 4, pp. 1131–1141, 1982.
- [24] W. Y. Ching, P. Rulis, and A. Misra, "Ab initio elastic properties and tensile strength of crystalline hydroxyapatite," *Acta Biomaterialia*, vol. 5, no. 8, pp. 3067–3075, 2009.
- [25] M. J. Olszta, X. Cheng, S. S. Jee, R. Kumar, Y.-Y. Kim, M. J. Kaufman, E. P. Douglas, and L. B. Gower, "Bone structure and formation: a new perspective," *Materials Science and Engineering: R: Reports*, vol. 58, no. 3-5, pp. 77–116, 2007.
- [26] R. Astala and M. J. Stott, "First-principles study of hydroxyapatite surfaces and water adsorption," *Physical Review B*, vol. 78, no. 7, p. 075427, 2008.
- [27] S.-W. Chang, S. Shefelbine, and M. Buehler, "Structural and mechanical differences between collagen homo- and heterotrimers: Relevance for the molecular origin of brittle bone disease," *Biophysical Journal*, vol. 102, no. 3, pp. 640–648, 2012.

- [28] S.-W. Chang, B. P. Flynn, J. W. Ruberti, and M. J. Buehler, "Molecular mechanism of force induced stabilization of collagen against enzymatic breakdown," *Biomaterials*, vol. 33, no. 15, pp. 3852–3859, 2012.
- [29] J. K. Rainey and M. C. Goh, "An interactive triple-helical collagen builder," *Bioinformatics*, vol. 20, no. 15, pp. 2458–2459, 2004.
- [30] S. Park, R. J. Radmer, T. E. Klein, and V. S. Pande, "A new set of molecular mechanics parameters for hydroxyproline and its use in molecular dynamics simulations of collagen-like peptides," *Journal of Computational Chemistry*, vol. 26, no. 15, pp. 1612–1616, 2005.
- [31] S. Hauptmann, H. Dufner, J. Brickmann, S. M. Kast, and R. S. Berry, "Potential energy function for apatites," *Physical Chemistry Chemical Physics*, vol. 5, no. 3, pp. 635–639, 2003.
- [32] J. W. Shen, T. Wu, Q. Wang, and H. H. Pan, "Molecular simulation of protein adsorption and desorption on hydroxyapatite surfaces," *Biomaterials*, vol. 29, no. 5, pp. 513–532, 2008.
- [33] S. Plimpton, "Fast parallel algorithms for short-range molecular dynamics," *Journal of Computational Physics*, vol. 117, no. 1, pp. 1–19, 1995.
- [34] W. Humphrey, A. Dalke, and K. Schulten, "Vmd: Visual molecular dynamics," *Journal of Molecular Graphics*, vol. 14, no. 1, pp. 33–38, 1996.
- [35] A. Gautieri, S. Vesentini, A. Redaelli, and M. J. Buehler, "termolecular slip mechanism in tropocollagen nanofibrils," *Journal of Materials Research*, no. 7, pp. 921–925, 2009.
- [36] ASTM, "Astm d 3528-96 - standard test method for strength properties of double lap shear adhesive joints by tension loading," 2008.
- [37] B. Smith, T. Schaffer, M. Viani, J. Thompson, and N. Frederick, "Molecular mechanistic origin of the toughness of natural adhesives, fibres and composites," *Nature*, vol. 399, p. 761, 1999.
- [38] G. E. Fantner, T. Hassenkam, J. H. Kindt, J. C. Weaver, H. Birkedal, L. Pechenik, J. A. Cutroni, G. A. G. Cidade, G. D. Stucky, D. E. Morse, and P. K. Hansma, "Sacrificial bonds and hidden length dissipate energy as mineralized fibrils separate during bone fracture," *Nature Materials*, vol. 4, no. 8, pp. 612–616, 2005.
- [39] R. O. Ritchie, M. J. Buehler, and P. Hansma, "Plasticity and toughness in bone," *Physics Today*, vol. 62, no. 6, pp. 41–47, 2009.

Chapter 5

Fracture Mechanics of Hydroxyapatite Crystals

This chapter is extracted from "Fracture mechanics of hydroxyapatite single crystals under geometric confinement", accepted for publication in December 2012 [1]. Geometric confinement to the nanoscale, a concept referring to the characteristic dimensions of structural features of materials at this length scale, has been shown to control the mechanical behavior of many biological materials, and such effects have also been suggested to play a crucial role in enhancing the strength and toughness of bone. Here we study the effect of geometric confinement to the nanoscale on the fracture mechanism of hydroxyapatite crystals that form the mineralized phase in bone. This is a full atomistic study that aims to provide a fundamental description of the mechanical behavior of HAP as bone building block, in view of investigating possible toughening mechanisms, acting at this scale. The analysis of scale-related toughening mechanisms, to be replicated in the design of a new bone-inspired tough material as described in Chapter 6, may be helpful in the biomimetic research.

5.1 Introduction

Hydroxyapatite (HAP) is the main component of many biological hard tissues, such as dentine, enamel, and bone. It is considered, together with the collagen matrix, as the main building block of bone [2–7]. It plays a critical role in determining the stiffness and the strength, since it carries most of the tensile load due to the higher elastic modulus and strength compared to the collagen matrix. The combination of two distinct materials, with a staggered arrangement of HAP brittle platelets embedded in a soft collagen matrix, is believed to lead to materials with high mechanical properties. Indeed, bone and bone-like materials show a good combination of mechanical properties (*i.e.* strength, toughness, *etc.*), providing support for many organisms, owing largely to their hierarchical structure [4–6, 8–10]. For instance, bone's resistance to fracture results from a multitude of deformation and toughening mechanisms, which occur at many scales, from the nano- to the macroscale [2, 5, 6, 10–12].

Earlier work has suggested that the remarkable behavior of bone and bone-like materials - with great toughness in spite of brittle mineral components - is due to the nanometer confinement of its HAP building blocks [13]. This concept has been supported by the tension-shear model, which describes the load transfer between the mineral and protein phase. Here, the mineral platelets carry most of the tensile load and the protein matrix transfers the load between the platelets by shear [8, 14–17]. In a series of papers the path of load transfer in a biological

composite, such as bone, has been simplified [16, 17] to a one-dimensional serial spring system, which consists of mineral elements (subjected to tension) spread among protein elements (subjected to shear). Indeed, earlier work has found that the rigidity and strength of bone and biocomposites depend on the tensile strength of mineral and on the shear strength of the protein. According to [17] large tensile strain can cause the formation of microcracks near the end of mineral platelets. However, those cracks generally do not play a critical role in the structural integrity of biocomposites, in contrast to what generally occurs in engineering materials, where cracks are associated to loss of stiffness and strength (*e.g.* according to damage mechanics theory). It has also been shown that the platelet shape of the HAP crystals has an important role, because of the high surface to volume ratio, which ensures large interaction with the collagen protein and enhanced mechanical properties [18–20].

In this chapter we study the mechanical behavior of HAP single crystals focusing on fracture; in particular, we investigate how the presence of a crack-like defect affects the mechanical properties of such crystals. In order to systematically analyze the effect of geometric confinement on the HAP crystal, several cases are considered and *in silico* mechanical tests are performed by varying the sample height. We analyze the mechanical behavior, by observing the failure mode and by examining the stress field, to confirm earlier suggestions of a size-induced flaw-tolerant state in biological materials [13].

This work covers a full-atomistic study to directly investigate the confinement phenomena in a HAP single crystal. We emphasize that this study is not supposed to provide a model of bone. Instead it aims to provide us with insight into the fracture behavior of individual HAP crystals at the nanoscale. Also, this study may explain the mechanical stability of the reinforcing HAP platelets in bone and provide an understanding of the toughening mechanisms acting in bone at subnanoscale, which can be mimicked in the design of the new bone-inspired tough material described in Chapter 6.

5.2 Background

5.2.1 Hydroxyapatite

Apatites are calcium-phosphate minerals that are found in several different forms (as long as the base of apatite calcium and phosphorus exist together). The most common forms of apatite ($\text{Ca}_5(\text{PO}_4)_3\text{X}$) are cloroapatite, fluoroapatite and hydroxyapatite, where each one takes the name from the replacing anion (*i.e.* chlorine, fluorine, and hydroxide) [21]. Hydroxyapatite (HAP) is the main mineral component of bone and teeth and exists in two forms: monoclinic and hexagonal (HCP), where the latter is the one most commonly found [22]. The hexagonal structure of HAP has the formula $\text{Ca}_{10}(\text{PO}_4)_6(\text{OH})_2$, and is characterized by two units per cell ($Z = 2$), each one containing 44 atoms.

The hexagonal crystal contains three types of Ca ions: Ca type I, Ca type II, and Ca type III, with three, six and four oxygen atoms as first neighbors, respectively. OH group is linked to three Ca type III ions in a triangular planar arrangement on the a - b plane, with the hydroxyl in the center. Two ions of Ca type I and two of Ca type II are present in the cell in a octahedral arrangement. The unit cell also contains six phosphate groups, all equivalent by the symmetry. The two OH groups are oriented along the c -axis, and create internal channels [21, 23]. A representation of the HAP unit cell used here is depicted in Figure 5.1. We recognize two main planes, the basal plane (a - b plane) perpendicular to the c -axis, and the side plane (c -plane) parallel to the c -axis [24]. The (001) plane is the most stable one, with a surface energy of 1.043 J/m^2 [25] and it also shows ferroelectricity due to the orientation of the OH groups. This

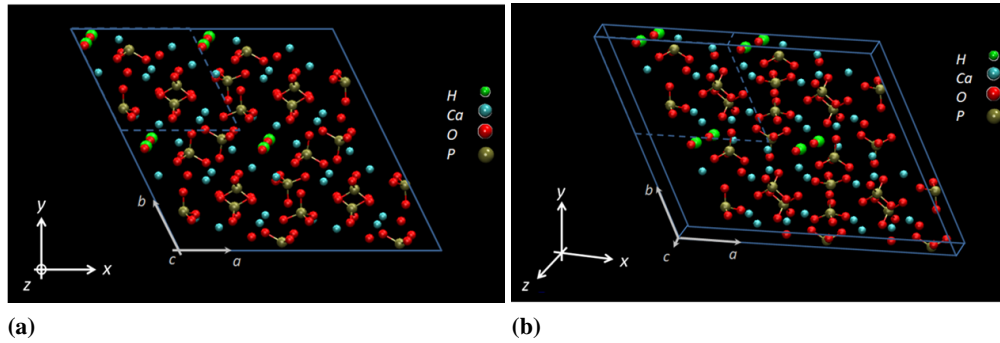


Figure 5.1: VMD "atom representation" of Hydroxyapatite (HAP) unit cell. Each atom is represented with a different color: H (green), Ca (blue), O (red), P (gray). The HAP unit is highlighted with a dashed line; the size of H atoms is increased to make them visible and to show the alignment of OH groups along the c -direction. Both the crystal axes (abc) and the coordinate axes (xyz) are shown. (a) View parallel to the (001) plane. (b) Three-dimensional view of the model.

plane has an important role in bone, since HAP crystallites are preferentially aligned with (001) orientation along the collagen fibril main axis [26]. The prismatic Ca-rich plane (010) is the plane that is most reactive with water, and it is of particular interest due to the growth directing effect of the collagen matrix. Also, it has electrostatic characteristics on its surfaces, showing a negative charge on the OH-rich surface and a positive charge on the Ca-rich surface. The (100) plane, instead, has geometric and chemical properties similar to the (010) plane [27, 28].

HAP in bone is deposited as elongated crystals incorporated into the collagen matrix during the mineralization process, and HAP crystals grow until reaching few nanometers [5, 29]. Large sized single crystals can be found in nature at a millimeter size (in non-living systems). Such crystals have been used for experimental studies to assess the mechanical properties (*i.e.* by nanoindentation) referred to the side and to the basal plane, confirming its anisotropy [24]. In [24] the mechanical properties of HAP crystals were determined by means of nanoindentation tests, and it was found that crystals are more resistant to microcrack events on the side, which is useful in bone, while the hardest and stiffer face (*i.e.* basal) is usually exposed (*e.g.* in teeth), to minimize mass loss from abrasion.

5.2.2 Geometric confinement

Geometric confinement is a concept that is linked to the characteristic dimensions of a material's micro-nanostructure. In many instances, components of biological materials have a characteristic size at the nanoscale, which bestows particular mechanical properties on those materials. Here, we refer to the case when the material's structure shows geometric features at the nanometer length-scale.

Earlier theoretical studies predicted that there exists an intrinsic length scale, depending only on the material and on the geometry, which controls the mechanical behavior in small crystals under geometrically confined conditions, leading to a flaw-tolerant state [13]. In this state, a material with a defect is expected to behave as one without a defect, reaching its theoretical strength, and the stress field will be homogenous without a stress concentration zone at the crack tip.

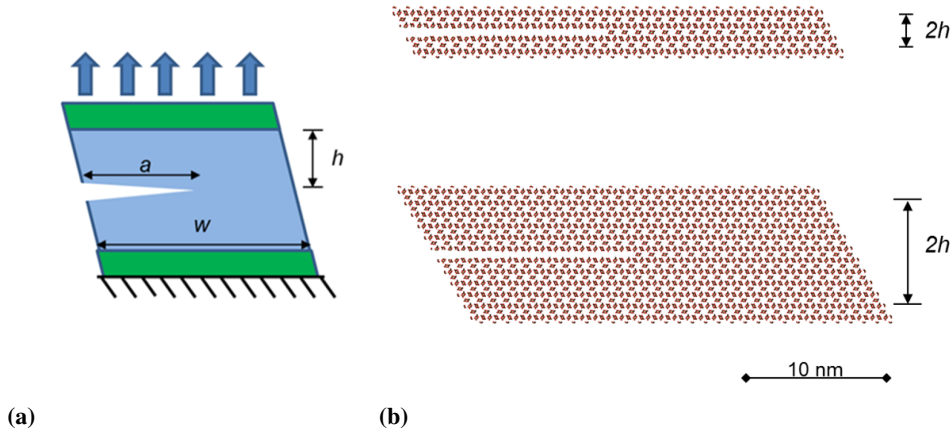


Figure 5.2: Geometry, dimensions and loading and boundary conditions of a cracked slab. (a) Model used for our atomistic study of fracture of HAP. Different samples are created by varying the sample height, 'h', whereby the width, 'w', and the crack length, 'a', are fixed for all cases. The dimension 'h' is considered as half of the height of the sample, excluding the fixed boundary regions (i.e. green-colored). The crack extends over half of the platelet width. (b) Snapshots of two samples.

In addition to studies on biominerals and other biological materials, it is possible to find, in the literature, other recent studies of flaw insensitive materials. Indeed, the phenomenon of flaw tolerance has been demonstrated to occur also in crystalline solids as shown by [30], in a series of *in-situ* TEM experiments, performed on Al strips with an edge crack. Kumar *et al.* experimental work revealed the absence of any measurable stress concentration at the notch tip. Furthermore, in [31] a numerical study on nanocrystalline graphene identified the presence of a critical length scale, below which a flaw-independent fracture behavior occurs.

5.3 Materials and Methods

5.3.1 Atomistic Model

The model is a thin slab of hydroxyapatite with a sharp crack on the basal plane (001), corresponding to the x - y plane, and the crack main axis along the [100] direction. We consider a hexagonal (HCP) crystal, with $x = [100]$, $y = [010]$, and $z = [001]$. The initial crack extends over half of the sample in the x direction. The crack opening angle is $\alpha \approx 2^\circ$, the crack length $a \approx 15.1$ nm, the sample width $w \approx 30.1$ nm and the out-of-plane sample thickness $t \approx 2.1$ nm are kept fixed during all the simulations, whereas the sample height (considered as y dimension) varies from 2.5 to 9.6 nm. Figure 5.2a shows the model with parameters such as height, width, and crack length; snapshots of two samples with different height are shown Figure 5.2b. It is noted that the platelets in bone are generally tens of nm in width and length and 2-3 nm in thickness [5, 29].

5.3.2 Crystal Geometry

The hydroxyapatite crystal unit cell is generated by using Materials Studio 4.4 (Accelrys, Inc.). It is a hexagonal unit cell with 44 atoms and the following lattice parameters: $a = 9.4214 \text{ \AA}$, $b = 9.4214 \text{ \AA}$, $c = 6.8814 \text{ \AA}$, $\alpha = 90^\circ$, $\beta = 90^\circ$, $\gamma = 120^\circ$ [28]. The samples are created by replicating the unit cell 32 times in the x directions, three times in the z direction, and n times in the y directions; n varies from 4 to 14 to study the effect of constraining the size of the hydroxyapatite crystal on its fracture. The HAP samples are created by systematically increasing the height by two unit cells in the y -direction.

5.3.3 Hydroxyapatite Force Field Parametrization

We use an extended CHARMM force field as reported in [28], where the authors added non-bonded parameters, calculated by using a Born-Mayer-Huggins model [18, 32]. Instead, the bond, angle and dihedral parameters are based on quantum-mechanics calculations and experimental data. The force field has been validated in earlier works [18, 28, 32–34]. The choice of adopting this force field is also motivated by the fact that it has been shown to correctly model the behavior of collagen and HAP-collagen systems, as shown in Chapter 4, in spite of its shortcomings. We note that the strength and modulus of a single HAP crystal show a relatively large difference (about four times) compared to those obtained by Ching *et al.* [35], who reported a study of an orthorhombic HAP cell by using Density Functional Theory.

5.3.4 Molecular Dynamics Simulations

The LAMMPS code [36] is used to perform molecular dynamics simulations of the strip crack problem. In this study a modified CHARMM force field is used to describe the overall strain energy of the system. Lennard-Jones and Coulombic interactions are computed with an additional switching function that ramps the energy and force smoothly to zero between an inner (8 \AA) and outer cutoff (10 \AA) [36]. This cutoff range is selected so as to include one unit lattice over the thickness. Moreover, an additional $1/r$ term is included in the Coulombic formula; thus, the Coulombic energy varies as $1/r^2$, which is an effective distance-dielectric term. This represents a simple model for an implicit solvent with additional screening and it is designed to be used in simulations of biomolecules without explicit water solvent [36]. The sample is included in a large simulation box with non-periodic boundary conditions. The model is geometrically optimized through energy minimization, by using two different algorithms, the conjugate gradient and the steepest descent methods. Afterwards the bottom of the strip is clamped and the structure is relaxed under an NVE ensemble for 100 ps. Once the structure is fully relaxed (confirmed through the root-mean square deviation convergence to a constant value of $\approx 2 \text{ \AA}$), quasi-static loading is applied. Loading consists of several increments, each followed by energy minimization. The loading-minimization cycles are run until failure occurred. A time step of 0.5 fs is used in all dynamical simulations. A schematic of the sample with the applied loading conditions is given in Figure 5.2a. A sample input script for LAMMPS is given in Appendix A, while a sample script for atom definition is shown in Appendix B.

5.3.5 Data Post-processing

The data analysis is performed by using Visual Molecular Dynamics (VMD) [37], to visualize the simulation trend and to print the snapshots of the tests. To analyze the mechanical response of the material under the applied loading conditions, MATLAB (Mathworks, Inc.) is used,

while AtomEye [38] is used to plot the stress distribution in each sample. In the post processing we use the virial stress output from the simulations, and the engineering strain to get the stress-strain response. The mechanical properties (*i.e.* stiffness, maximum strength, strain at failure, *etc.*) are calculated from the stress-strain data. The tensile modulus is calculated by using a linear fitting to the $\sigma - \varepsilon$ data for deformation up to 2%, where the behavior is generally linear. Stress maps are created by plotting the virial stresses [39,40] on each atom, by means of AtomEye [38].

5.3.6 Stress Analysis

For analysis, we consider the stress distribution ahead of the crack tip, just before the maximum stress has reached and failure occurred. The atomistic virial stress data, computed in a thin strip ahead of the crack tip, and averaged, are then fitted by using a power law of the form in Eq. 5.1:

$$y = (1 - t)e^{\beta_i x} + t \quad (5.1)$$

where t represents the asymptotic value of the stress for each sample, which is a value that indicates the stress level in the far field, for each studied case; the constant ahead the exponent, β_i , is defined in two ways (Eq. 5.2-5.3):

$$\beta_1 = \frac{y_2 - y_1}{x_2 - x_1} \cdot (t - 1)^{-1} \quad (5.2)$$

and

$$\beta_2 = \frac{1}{x_2} \cdot \ln \left(\frac{1 - t}{y_2 - t} \right) \quad (5.3)$$

x_1 and x_2 represent the x -coordinates of the first two data (in space), in each sample; y_1 and y_2 represent the corresponding stress values (*i.e.* first two stress data), in each sample. In the graph in Figure 5.6, on the y axis the longitudinal stress, normalized on the maximum value reached in each sample, is represented, whereas on the abscissa, the x -coordinate, normalized on $w/2$ (*i.e.* half of the sample width), is given. The zero x -coordinate refers to the crack tip position. The exponent is defined in two ways, through Eq. 5.2 and Eq. 5.3. In both cases, to ensure better data fitting, the first two data in space (with x_1 and x_2 as space coordinates, and y_1 and y_2 as stress coordinates) are considered.

5.4 Results

The stress-strain curves of the tested samples are depicted in Figure 5.3. In Table 5.1, an overview of the determined strength is given for all the samples.

We recognize an initial linear elastic regime, which is not affected by the sample size. In this regime, the material is slightly deformed, but no damage occurs. Also, we observe that the stiffness of the sample is not affected by the sample size (*i.e.* height), and that the slope of the stress-strain curves is similar for all cases. The linear regime is followed by a second regime that is characterized by a deviation from linearity. Here, the stress slowly increases until a maximum has been reached. This phase corresponds to a sub-critical propagation of the defect. Initially, we do not observe a clear crack propagation mechanism. As the load increases,

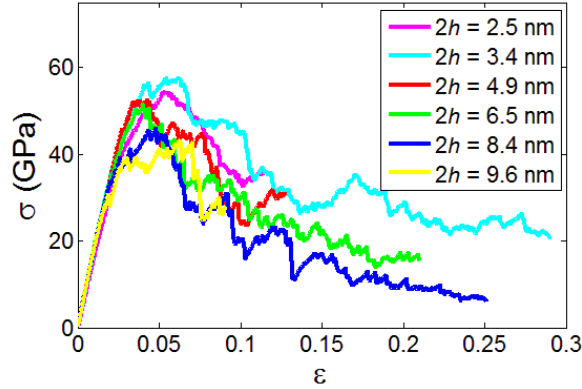


Figure 5.3: Stress-strain plot of the tested samples. The stress is the longitudinal stress σ_{yy} (i.e. in the y -direction) and the strain represents the applied tensile strain in the y -direction. The initial slope of the stress-strain curve is not affected by the size of the sample, whilst the strength decreases by increasing the sample height.

Table 5.1: Mechanical strength of the HAP samples compared to the effect of the sample height $2h$. The initial crack extends over half of the sample in the x -direction. The crack opening angle ($\alpha \approx 2^\circ$), the crack length ($a \approx 15.1$ nm), the sample width ($w \approx 30.1$ nm) and the sample thickness ($t \approx 2.1$ nm) are the same for all cases, and the sample height varies from 2.5 to 9.6 nm. The strength is determined as the maximum stress reached.

Sample size $2h$ (nm)	Strength (GPa)
2.5	54.28
3.4	57.67
4.9	52.46
6.5	51.48
8.4	45.97
9.6	43.19
9.6 ^a	54.56

^aThis represents a sample without edge crack, for comparison (providing an estimate of the theoretical strength of a defect-free material). The comparison with the other strength values shows that the strength reached for the samples in the flaw tolerant state reach the theoretical strength.

different phenomena besides crack opening occur. For small size cases, many defects emerge in different parts of the samples, which then grow until the maximum stress is reached. For larger samples, we find that failure is more localized around the crack tip region.

Beyond the maximum stress, failure occurs in different modes depending on the sample size. For small samples, it occurs more gradually and it is not characterized by a clear crack path. Damage is widespread due to the formation and interaction of many small defects over the whole volume, as shown in Figure 5.4a. The growth of these defects and their interaction lead to the global failure of the slab. By increasing the sample size, a clear crack path can be noticed, as is confirmed in Figure 5.4b, where snapshots related to the failure of samples of different sizes are shown. We emphasize the different strain levels at which snapshots are taken

in Figures 5.4a versus 5.4b; failure in the smaller sample occurs at strains in excess of 70%, whereas the crack spreads through the sample at a strain of about 10% in the larger case.

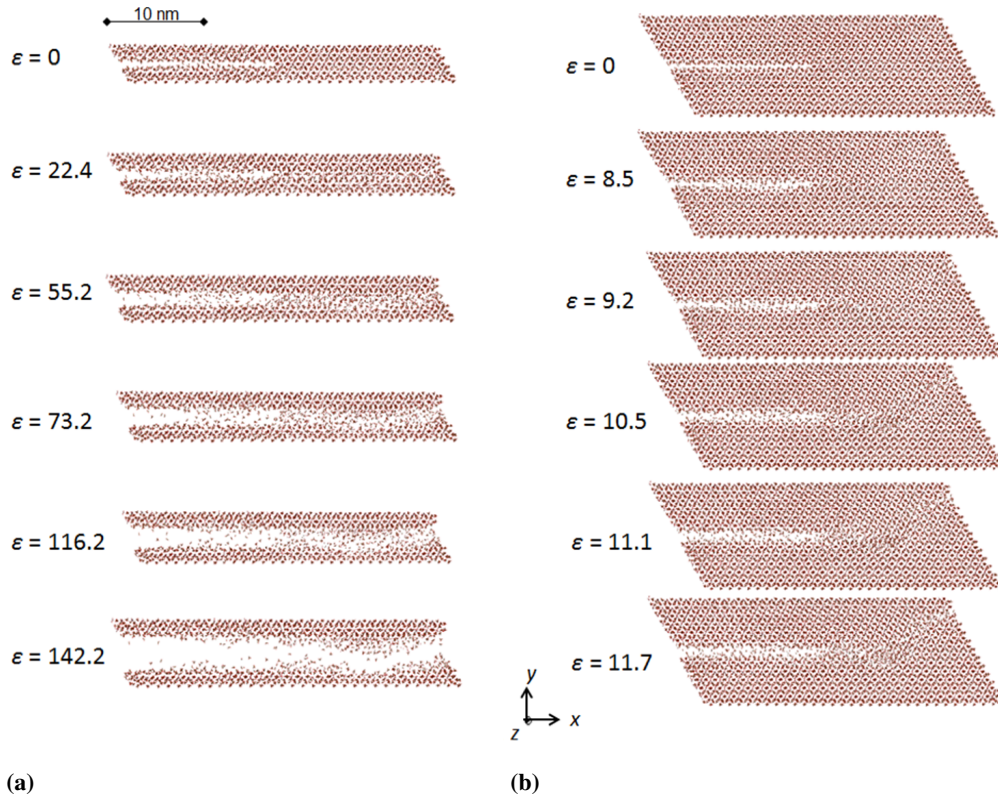


Figure 5.4: Snapshots of the failure mechanisms of two different samples at different applied percent strain (numbers given in %): (a) sample with height $2h = 2.5$ nm; (b) sample with height $2h = 8.4$ nm. The smaller sample is characterized by a more distributed mode of failure with significantly larger strain levels, while in the latter a clear crack path can be recognized, with failure occurring at relatively small applied strains.

Continuum fracture mechanics predicts that the area near the crack tip represents a region of stress concentration. Figure 5.5 shows the stress-strain curves and stress fields for two samples of different sizes, confirming that there is a clear difference between the two cases. The colors reveal the stress distribution in the middle section of each sample, referred to the critical strain ϵ^* , before failure occurred. In the smaller sample (Figure 5.5c) with $2h = 2.5$ nm, the stresses are homogeneously distributed, whereas in the larger one (Figure 5.5d) with $2h = 8.4$ nm, a concentration of higher stresses is clearly visible ahead the crack tip.

This phenomena is directly seen in Figure 5.6, where we plot the stress distribution in a thin strip ahead of the crack tip just before failure occurs. The graph shown in Figure 5.6 confirms that the small sample is characterized by a quasi-homogeneous stress distribution, whilst the larger ones are characterized by a high stressed region near the crack tip. The larger the size, the more localized the area of high stress concentration. This analysis reveals that the stress field becomes increasingly homogeneous as the size is reduced. In particular, for small samples below $2h = 3.4$ nm, the stress field is essentially homogeneous and the stress concentration disappears.

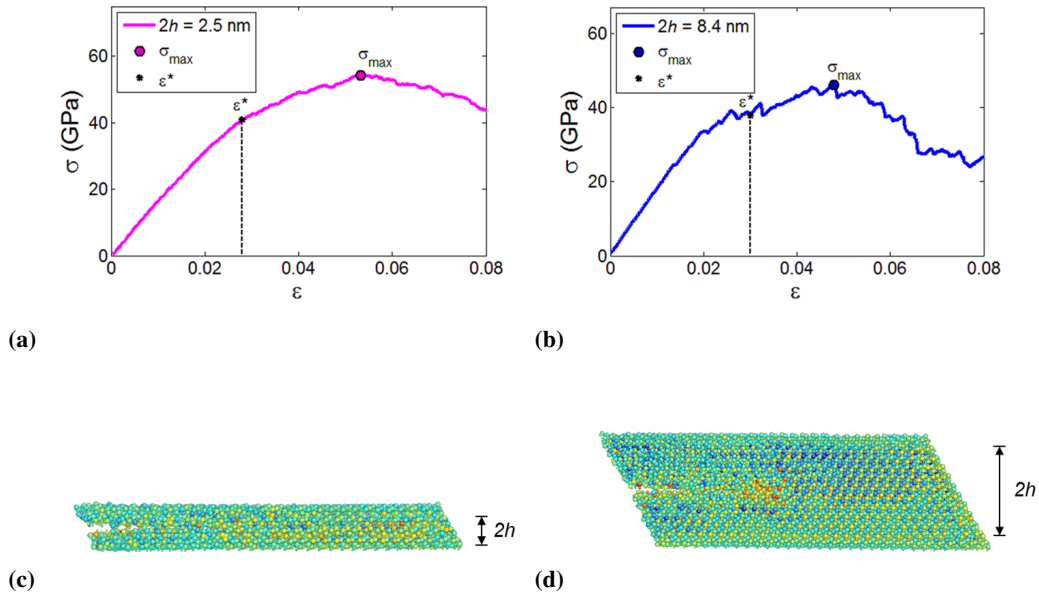


Figure 5.5: Stress-strain curve of two samples: (a) sample with height $2h = 2.5$ nm; (b) sample with height $2h = 8.4$ nm. Maps of the stress distribution for two cases: (c) sample with height $2h = 2.5$ nm; (d) sample with height $2h = 8.4$ nm. The maps show the stress field (in the middle section of each sample) at the critical strain ϵ^* , which is highlighted in the curves above. Also, the maximum stress (σ_{max}), reached before failure occurs, is highlighted in the two curves.

From the stress-strain curves depicted in Figure 5.3 we calculate the strength and find that it is clearly affected by the size. The strength, defined as the maximum stress reached during the test, is generally higher for smaller samples. Strength values of all the samples are shown in Table 5.1. On the basis of the results presented above (*e.g.* failure mode, stress field, stress distribution from the crack tip to the far field) we observe that a distinct change in the mechanical behavior occurs at around $2h = 4.15$ nm. By considering the determined values of the strength (normalized by the maximum stress achieved in the uncracked sample) as a function of the inverse of the square root of the sample size $\sqrt{h_{cri}/h}$, a bilinear trend is found (Figure 5.7). According to the results found here, we identify $2h = 4.15$ nm as a critical size. By comparing the data with the prediction of the Griffith's theory, we confirm that this theory is valid only for samples larger than the critical size, whereas for the smaller ones this theory does not hold, in agreement with the hypothesis put forth in [13]. These findings corroborate the concept that, at the nanoscale, flaw tolerance occurs in HAP crystals below a critical size.

5.5 Remarks

The results of this study, summarized in Figure 5.8 reveal that a decrease in the crystal size causes a change in the mechanical behavior and the occurrence of new deformation phenomena: *i*) a change in the failure mode, from a brittle-like crack-driven failure in larger samples to a more spread failure mode in the smaller ones, *ii*) a change in the stress field, from a heterogeneous stress field with a pronounced stress concentration at the tip of the crack to a very

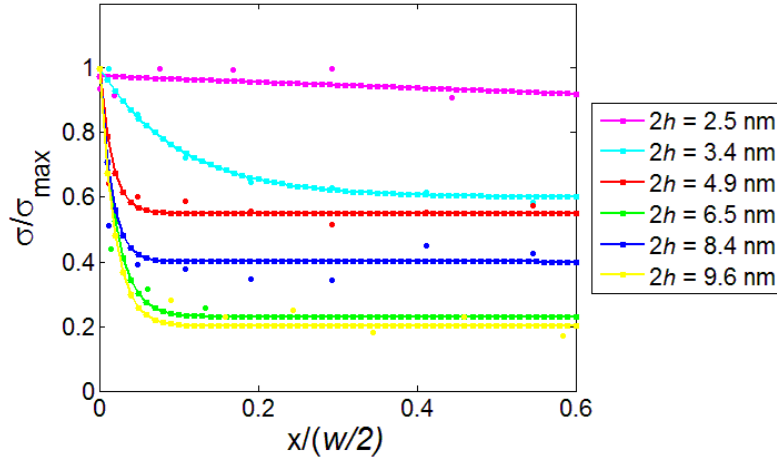


Figure 5.6: Stress field reaching from the crack tip to the far field for all samples shown in Table 5.1 and in Figure 5.3. The longitudinal stress field, averaged over a thin strip in the middle and over the entire thickness, is plotted against the x -direction (the zero x -coordinate represents the crack tip). The values on both the axes are normalized by the maximum values, respectively. The continuous lines represent power law fits to the atomistic data.

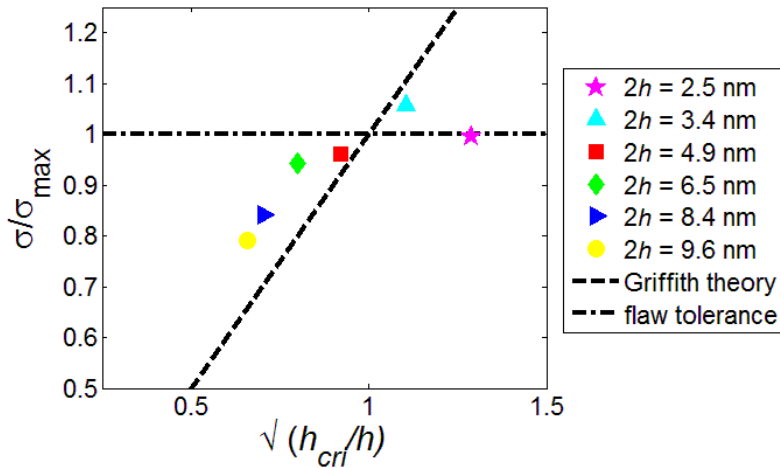


Figure 5.7: Normalized maximum strength over the normalized sample size. Comparisons with the Griffith theory prediction are given, showing a clear deviation at small length scales below the critical size $2h = 4.15$ nm.

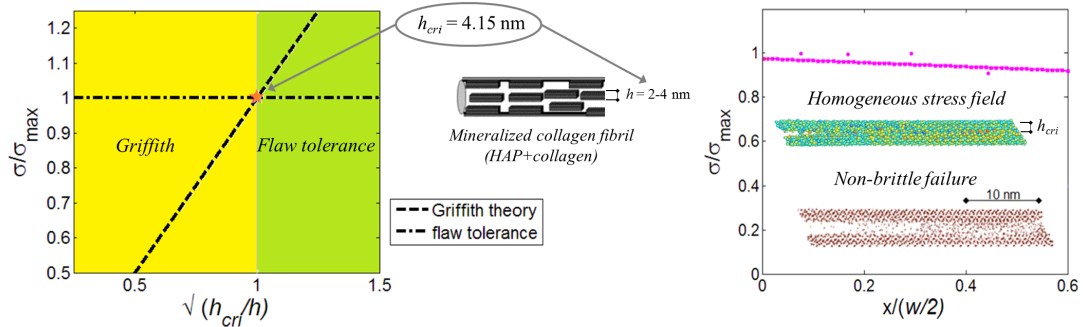


Figure 5.8: Summary of the principal findings described in Chapter 5: *flaw tolerance occurs below a certain critical size, which corresponds to the nanosize of HAP crystals in bone [5, 29, 41, 42]; HAP crystals fails in a non-brittle mode with large strain at failure and strength approaching the values of uncracked samples; the stress field, before critical crack propagation occurs, is homogeneous, showing no stress concentration at the tip of the crack.*

homogeneous stress field, *iii*) a general improvement of the mechanical properties (*i.e.* strength, strain at failure, and hence toughness modulus), approaching the values of the crystal without a crack. Our findings confirm the hypothesis put forth in an earlier paper [13] that mineral crystals become flaw-tolerant below a certain size, typically at the nanometer length-scale. Moreover, we have directly calculated the critical length scale for flaw tolerance in a HAP crystal and identified it to be around 4.15 nm (here, done for a sample aspect ratio of $2h/w = 0.138$), a value corresponding to the nanosize of HAP crystals in bone [5, 29, 41, 42]. Indeed, the concept of flaw-tolerance may explain how biological materials can gain superior mechanical properties, by arranging them in hierarchical structures with characteristic dimensions at each level. This insight may be important for a variety of applications including tissue engineering [3], the development of biocompatible composites [7] and understanding diseases related to bone and bone formation [43, 44].

Also, this concept is helpful in understanding the origin of the mechanical stability of the reinforcing HAP platelets in bone, providing an explanation of the toughening mechanisms acting at subnanoscale. These mechanisms can be mimicked in the design of new tough biomimetic materials. Indeed, nanosized hard platelets (like HAP) can be implemented in the design of bio-inspired composite materials to improve the toughness characteristic. In this thesis work, this insight may lay the groundwork for a further improvement of the design of the new bone-inspired composite, described in Chapter 6-7.

Bibliography

- [1] F. Libonati, A. K. Nair, L. Vergani, and M. J. Buehler, "Fracture mechanics of hydroxyapatite single crystals under geometric confinement," *Journal of the mechanical behavior of biomedical materials*, no. DOI: <http://dx.doi.org/10.1016/j.jmbbm.2012.12.005>, 2013.
- [2] B. Alexander, T. L. Daulton, G. M. Genin, J. Lipner, J. D. Pasteris, B. Wopenka, and S. Thomopoulos, "The nanometre-scale physiology of bone: steric modelling and scanning transmission electron microscopy of collagen-mineral structure," *Journal of the Royal Society Interface*, vol. 9, no. 73, pp. 1774–86, 2012.
- [3] S. Bhumiratana, W. L. Grayson, A. Castaneda, D. N. Rockwood, E. S. Gil, D. L. Kaplan, and G. Vunjak-Novakovic, "Nucleation and growth of mineralized bone matrix on silk-hydroxyapatite composite scaffolds," *Biomaterials*, vol. 32, no. 11, pp. 2812–20, 2011.
- [4] H. D. Espinosa, J. E. Rim, F. Barthelat, and M. J. Buehler, "Merger of structure and material in nacre and bone - perspectives on de novo biomimetic materials," *Progress in Materials Science*, vol. 54, no. 8, pp. 1059–1100, 2009.
- [5] M. E. Launey, M. J. Buehler, and R. O. Ritchie, "On the mechanistic origins of toughness in bone," *Annual Review of Materials Research*, vol. 40, no. 1, pp. 25–53, 2010.
- [6] R. O. Ritchie, M. J. Buehler, and P. Hansma, "Plasticity and toughness in bone," *Physics Today*, vol. 62, no. 6, pp. 41–47, 2009.
- [7] L. C. Wu, J. Yang, and J. Kopecek, "Hybrid hydrogels self-assembled from graft copolymers containing complementary beta-sheets as hydroxyapatite nucleation scaffolds," *Biomaterials*, vol. 32, no. 23, pp. 5341–53, 2011.
- [8] H. Gao, *Application of fracture mechanics concepts to hierarchical biomechanics of bone and bone-like materials Advances in Fracture Research*, pp. 101–137. Springer Netherlands, 2006.
- [9] E. Hamed and I. Jasiuk, "Elastic modeling of bone at nanostructural level," *Materials Science and Engineering: R: Reports*, vol. 73, no. 3-4, pp. 27–49, 2012.
- [10] D. Sen and M. J. Buehler, "Structural hierarchies define toughness and defect-tolerance despite simple and mechanically inferior brittle building blocks," *Scientific Reports*, vol. 1, 2011.
- [11] Q. Chen, C. Wong, W. Lu, K. Cheung, J. Leong, and K. Luk, "Strengthening mechanisms of bone bonding to crystalline hydroxyapatite in vivo," *Biomaterials*, vol. 25, pp. 4243–4254, 2004.
- [12] D. K. Dubey and V. Tomar, "Microstructure dependent dynamic fracture analyses of trabecular bone based on nascent bone atomistic simulations," *Mechanics Research Communications*, vol. 35, no. 1-2, pp. 24–31, 2008.
- [13] H. Gao, B. Ji, I. Jager, E. Arzt, and P. Fratzl, "Materials become insensitive to flaws at nanoscale: Lessons from nature," *Proceedings of the National Academy of Sciences*, vol. 100, no. 10, pp. 5597–5600, 2003.

- [14] M. J. Buehler, H. Yao, H. Gao, and B. Ji, "Cracking and adhesion at small scales: atomistic and continuum studies of flaw tolerant nanostructures," *Modelling and Simulation in Materials Science and Engineering*, vol. 14, no. 5, p. 799, 2006.
- [15] H. S. Gupta, W. Wagermaier, G. A. Zickler, D. Raz-Ben Aroush, S. S. Funari, P. Roschger, H. D. Wagner, and P. Fratzl, "Nanoscale deformation mechanisms in bone," *Nano Letters*, vol. 5, no. 10, pp. 2108–2111, 2005.
- [16] B. Ji and H. Gao, "Mechanical properties of nanostructure of biological materials," *Journal of the Mechanics and Physics of Solids*, vol. 52, p. 1963, 2004.
- [17] B. Ji and H. Gao, "A study of fracture mechanisms in biological nano-composites via the virtual internal bond model," *Materials Science and Engineering: A*, vol. 366, no. 1, pp. 96–103, 2004.
- [18] R. Bhowmik, K. S. Katti, and D. Katti, "Molecular dynamics simulation of hydroxyapatite-polyacrylic acid interfaces," *Polymer*, vol. 48, no. 2, pp. 664–674, 2007.
- [19] D. Dubey and V. Tomar, "Role of molecular level interfacial forces in hard biomaterial mechanics: A review," *Annals of Biomedical Engineering*, vol. 38, no. 6, pp. 2040–2055, 2010.
- [20] D. K. Dubey and V. Tomar, "Understanding the influence of structural hierarchy and its coupling with chemical environment on the strength of idealized tropocollagen-hydroxyapatite biomaterials," *Journal of the Mechanics and Physics of Solids*, vol. 57, no. 10, pp. 1702–1717, 2009.
- [21] R. Z. LeGeros, A. Ito, K. Ishikawa, T. Sakae, and J. P. LeGeros, *Fundamentals of Hydroxyapatite and Related Calcium Phosphates*, pp. 19–52. John Wiley & Sons, Inc., 2010.
- [22] J. C. Elliott, P. E. Mackie, and R. A. Young, "Monoclinic hydroxyapatite," *Science*, vol. 180, no. 4090, pp. 1055–1057, 1973.
- [23] M. Corno, R. Orlando, B. Civalleri, and P. Ugliengo, "Periodic b3lyp study of hydroxyapatite (001) surface modelled by thin layer slabs," *European Journal of Mineralogy*, vol. 19, no. 5, pp. 757–767, 2007.
- [24] S. Saber-Samandari and K. A. Gross, "Micromechanical properties of single crystal hydroxyapatite by nanoindentation," *Acta Biomaterialia*, vol. 5, no. 6, pp. 2206–2212, 2009.
- [25] M. Corno, C. Busco, V. Bolis, S. Tosoni, and P. Ugliengo, "Water adsorption on the stoichiometric (001) and (010) surfaces of hydroxyapatite: A periodic b3lyp study," *Langmuir*, vol. 25, no. 4, pp. 2188–2198, 2009.
- [26] M. J. Olszta, X. Cheng, S. S. Jee, R. Kumar, Y.-Y. Kim, M. J. Kaufman, E. P. Douglas, and L. B. Gower, "Bone structure and formation: a new perspective," *Materials Science and Engineering: R: Reports*, vol. 58, no. 3-5, pp. 77–116, 2007.
- [27] R. Astala and M. J. Stott, "First-principles study of hydroxyapatite surfaces and water adsorption," *Physical Review B*, vol. 78, no. 7, p. 075427, 2008.
- [28] Z. Qin, A. Gautieri, A. Nair, H. Inbar, and M. J. Buehler, "Thickness of hydroxyapatite nanocrystal controls mechanical properties of the collagen-hydroxyapatite interface," *Langmuir*, vol. 28, no. 4, pp. 1982–1992, 2012.

- [29] J. Y. Rho, L. Kuhn-Spearing, and P. Zioupos, "Mechanical properties and the hierarchical structure of bone," *Medical Engineering & Physics*, vol. 20, no. 2, pp. 92–102, 1998.
- [30] S. Kumar, X. Li, A. Haque, and H. Gao, "Is stress concentration relevant for nanocrystalline metals?," *Nano Letters*, vol. 11, no. 6, pp. 2510–2516, 2011.
- [31] T. Zhang, X. Li, S. Kadkhodaei, and H. Gao, "Flaw insensitive fracture in nanocrystalline graphene," *Nano Letters*, vol. 12, no. 9, pp. 4605–4610, 2012.
- [32] S. Hauptmann, H. Dufner, J. Brickmann, S. M. Kast, and R. S. Berry, "Potential energy function for apatites," *Physical Chemistry Chemical Physics*, vol. 5, no. 3, pp. 635–639, 2003.
- [33] D. K. Dubey and V. Tomar, "Role of the nanoscale interfacial arrangement in mechanical strength of tropocollagen-hydroxyapatite-based hard biomaterials," *Acta Biomaterialia*, vol. 5, no. 7, pp. 2704–2716, 2009.
- [34] J. W. Shen, T. Wu, Q. Wang, and H. H. Pan, "Molecular simulation of protein adsorption and desorption on hydroxyapatite surfaces," *Biomaterials*, vol. 29, no. 5, pp. 513–532, 2008.
- [35] W. Y. Ching, P. Rulis, and A. Misra, "Ab initio elastic properties and tensile strength of crystalline hydroxyapatite," *Acta Biomaterialia*, vol. 5, no. 8, pp. 3067–3075, 2009.
- [36] S. Plimpton, "Fast parallel algorithms for short-range molecular dynamics," *Journal of Computational Physics*, vol. 117, no. 1, pp. 1–19, 1995.
- [37] W. Humphrey, A. Dalke, and K. Schulten, "Vmd: Visual molecular dynamics," *Journal of Molecular Graphics*, vol. 14, no. 1, pp. 33–38, 1996.
- [38] J. Li, "Atomeye: an efficient atomistic configuration viewer," *Modelling and Simulation in Materials Science and Engineering*, vol. 11, no. 2, p. 173, 2003.
- [39] D. H. Tsai, "The virial theorem and stress calculation in molecular dynamics," *The Journal of Chemical Physics*, vol. 70, no. 3, pp. 1375–1382, 1979.
- [40] J. A. Zimmerman, E. B. WebbIII, J. J. Hoyt, R. E. Jones, P. A. Klein, and D. J. Bammann, "Calculation of stress in atomistic simulation," *Modelling and Simulation in Materials Science and Engineering*, vol. 12, no. 4, p. S319, 2004.
- [41] W. S and W. HD, "The material bone: structure mechanical function relations," *Annu. Rev. Mater. Sci.*, vol. 28, p. 271, 1998.
- [42] Y.-Y. Hu, A. Rawal, and K. Schmidt-Rohr, "Strongly bound citrate stabilizes the apatite nanocrystals in bone," *Proceedings of the National Academy of Sciences*, vol. 107, no. 52, pp. 22425–22429, 2010.
- [43] S. P. Pathi, D. D. W. Lin, J. R. Dorvee, L. A. Estroff, and C. Fischbach, "Hydroxyapatite nanoparticle-containing scaffolds for the study of breast cancer bone metastasis," *Biomaterials*, vol. 32, no. 22, pp. 5112–5122, 2011.
- [44] M. Vanleene, A. Porter, P.-V. Guillot, A. Boyde, M. Oyen, and S. Shefelbine, "Ultrastructural defects cause low bone matrix stiffness despite high mineralization in osteogenesis imperfecta mice," *Bone*, vol. 50, no. 6, pp. 1317–1323, 2012.

Part III

Experimental analysis

Chapter 6

Bio-inspired Composite: from Concept to Realization

In the first chapters, we reviewed the concept of biomimetic, along with its approach and applications, followed by an overview of synthetic composite materials, with a special attention to natural composites. We mainly focused on bone, as an interesting natural composite, whose properties are strongly affected by its complex hierarchical structure. In this chapter, we start with a discussion about the toughening mechanisms in bone. Then we introduce the biomimetic approach used to mimic the bone microstructure, and we describe, in detail, the entire process of realization of a new bio-inspired material, from the initial concept to the final design and manufacturing.

6.1 Introduction

Bone has been a source of inspiration for many biomimetic materials [1]. Trees and bones are constantly reforming themselves along lines of stress; this algorithm has been put into a software and used to make lightweight structures (*i.e.* beam, bridges). Also GM Opel used it to create the skeleton of the so-called bionic car, using the minimum amount of material required to get the maximum strength, thus optimizing the strength-to-weight ratio. Moreover, one of the best things nature does is to minimize the amount of materials used: nature uses five polymers to build such a great variety of structures; man, instead, uses more than 350 types of polymers, with the drawbacks of increasing pollution and recycling-related issues. In the previous chapters, we got an insight into the bone mechanical properties at the nanoscale, by studying the behavior of its basic building blocks with an atomistic approach.

In the following sections we present how, with a biomimetic approach, we attempt to learn from nature and take advice from it. Indeed, this chapter is dedicated to the description of a new biomimetic composite material, inspired to the bone structure: from its concept and design, to the manufacturing; the following chapter (Chapter 7) is focused, instead, on the mechanical characterization of the newly designed material and the comparison with a classical laminate composite.

6.2 The Approach

The approach followed to be mimicked the bone structure consists of different phases: *i)* first of all the choice of the hierarchical level to mimic, in order to reproduce the mechanical perfor-

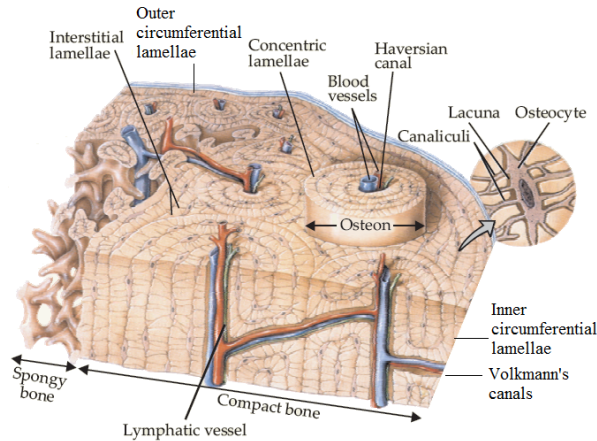


Figure 6.1: Representation of the microstructure of bone: on the left, spongy bone; on the right, the complex microstructure of cortical bone, characterized by the repeating osteon unit. Adapted from [2].

mance, *ii*) the definition of a concept, *iii*) the feasibility assessment, *iv*) the choice of materials and manufacturing technique, and *v*) the realization. In particular, the phases *ii*)-*iii*)-*iv*) are strictly connected, since the initial design is simplified to make it feasible with respect to the available manufacturing techniques. In phase *iv*) we also take a look to the costs, with the aim of proposing a cost-effective solution, compared to the other common composite materials, used in the structural field. Beside the new proposed material, a conventional composite laminate is also produced, and tested to allow a complete comparison with the bio-inspired one. We want to point out that the materials presented in this chapter, have been manually produced by one MSc student in the laboratory of the Clausthal University of Technology.

6.3 Bone Model

The hierarchical level, chosen as a model for the bone-inspired material is the level 5, described in Section 1.5.3, and characterized by the osteon or Haversian structure, shown in Figure 6.1.

6.3.1 Haversian System: Mechanical Properties

The microstructure of bone has been largely studied in the literature, to understand the role of the repeating unit (*i.e.* the osteons and their building blocks, the lamellae) on the mechanical properties of bone. In particular, Ascenzi and co-workers have largely examined the anisotropic mechanical properties of single Haversian systems, by experimental measurements under different loading conditions (*i.e.* tension, compression, bending and torsion) [3–6].

In tension, they measured the effects of the anisotropy on the elastic moduli and strength, by taking two types of samples 50 μm wide, smaller than a single osteon: *i*) the first type with the majority of lamellar orientation in the longitudinal direction, and *ii*) the second type, with adjacent lamellar orientations at sharp angles to each other [3]. Beyond determining the properties, they also claim to have microscopic evidence of failure: for instance, in tension transverse lamellae have shown to fail first and the osteon were kept together by the longitudinally oriented ones. Other literature studies [7] also confirmed that the majority of fibers is longitudinally oriented in the osteons. Results are shown in Table 6.1, where the higher values are referred to

longitudinal samples. In compression, Ascenzi *et al.* measured the effects of the anisotropy on single osteon samples, finding they were half as stiff as in tension, but comparable in terms of strength, with those in tension [4]. In bending, they found lower stiffness values but considerably higher strength values [5]. In torsion, they found that longitudinal lamellae are more resistant; however, an optimal combination of stiffness and strength has been found for torsional loadings [6].

The literature results, above discussed, showed that osteons with longitudinal lamellae are better for tension and torsion, and stronger in bending, whereas osteons with alternating lamellae are more appropriate for compression. Results are summarized in Table 6.1, where on the third column the first values (in each row) are referred to longitudinal samples, and the second values to interchanging orientational characterization of lamellae.

Table 6.1: Literature survey of mechanical properties of the Haversian system. The values included in the third column are referred to longitudinal samples (first values) and to interchanging orientation of lamellae (second values).

Study	Property	Value	Value	Test Method	Samples
Ascenzi <i>et al.</i> [3]	Elastic moduli (GPa)	12	5.5	Tensile	From cortical bone
	Tensile strength (MPa)	120	102		
Ascenzi <i>et al.</i> [4]	Stiffness (GPa)	6	7	Compressive	From isolated osteon
	Compressive strength (MPa)	110	130		
Ascenzi <i>et al.</i> [5]	Bending stiffness (GPa)	2	3	Bending	From calcified osteons
	Bending strength (MPa)	390	350		
Ascenzi <i>et al.</i> [6]	Torsional stiffness (GPa)	20	16	Torsional	From calcified osteons
	Torsional strength (MPa)	200	160		

6.3.2 Haversian System: Toughening Mechanisms

This level has revealed to play an important role in determining the bone toughness, by activating the so called *extrinsic toughening mechanisms*, which are object of large studies in the literature [2, 8], and are thought to be the source of micro- and macroscopic toughness in many biological materials. These mechanisms involve microstructural processes that inhibit the crack growth, by increasing the dissipation capacity, hence the toughness of bone. However, according to Launey *et al.* [8], the toughness of bone results from a mutual competition between extrinsic and intrinsic toughening mechanisms, predominating at scales above or below $1 \mu\text{m}$, respectively. In the range of $10\text{-}100 \mu\text{m}$, which corresponds to the osteon level, the main toughening (extrinsic) effects result from crack deflection and twisting, crack bridging by uncracked ligaments, constrained microcracking, and collagen-fibril bridging. According to Nalla *et al.* [9], these mechanisms contribute, in different measures, to a global increase in toughness of $2\text{-}5 \text{MPa}\sqrt{m}$; the largest contribution is given by crack deflection [10]. These mechanisms affect the crack growth, rather than the crack nucleation [8, 11]. Figure 6.2 shows the toughening mechanisms acting at a scale above $1 \mu\text{m}$ in bone. Crack bridging is a toughening mechanism also common among synthetic composite materials, where intact fibers act as a bridge, behind the crack tip, between the two surfaces of the crack, carrying out the load, and thus preventing the crack propagation. In bone instead, the bridging function is played by collagen fiber. Considering the architecture of bone at this level, a key-role is played by the osteon structural elements, which are supposed to be responsible of the crack growth; in particular, according

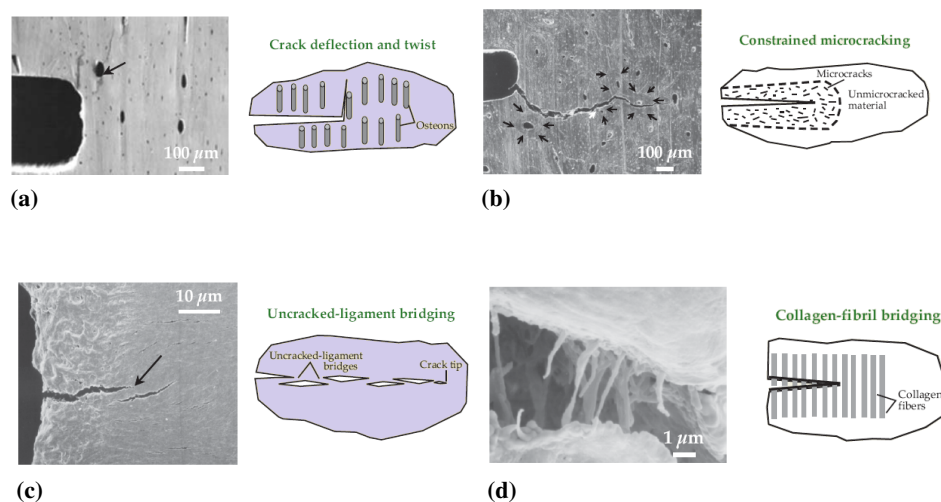


Figure 6.2: Toughening mechanisms in bone at different length scales in the 1-100 μm range [2]. (a) Crack deflection and twist: a crack, starting from a notch, encounters microcracks at the weak boundary of adjacent osteons (indicated with a black arrow); those microcracks cause energy dissipation and deviation of the growing crack from the direction of the maximum tensile stress, leading to an increase in toughness. (b) Constrained microcracking: effect of compression in the region around the main crack, preventing the crack to quickly propagate; such effect of compression is given by the presence of a large amount of small microcracks, which are naturally occurring in bone, allowing the remodeling process. (c) Uncracked-ligament bridging: an unbroken region, located between the growing crack a smaller crack, initiated ahead of it, can act as a bridge, increasing the toughness by carrying significant load. (d) Collagen fibril bridging: unbroken collagen fibrils act as a bridge between the two crack surfaces, preventing crack opening and growing.

to Nalla et al. [12], these cylindrical elements seem to control the crack path, deflecting and twisting the crack along the osteons outer boundary, consisting of cement lines, also considered as prime sites where microcracks form. Indeed, according to Ritchie et al. [2], bone is far more difficult to break than it is to split. In particular, Nalla et al. [9] reported a measurement of toughness, after only 500 μm of cracking, 5 times higher in transversal direction (*breaking*), than in longitudinal direction (*splitting*). This also confirm that bone toughness, as the other mechanical properties of bone, is affected by the characteristic anisotropy of this material. In fact, the fracture behavior of bone, at the osteon level, is characterized by different crack paths in the two directions. In the longitudinal direction, a mechanism known as *uncracked-ligament bridging* occurs: the microcracks, originated at the cement lines, are parallel to the growing crack, and they create, locally, some small regions acting as a bridge along the microcracks and allowing the load-bearing function. In the transverse direction, the microcracks originated at the cement lines have a perpendicular direction compared to the growing crack, causing crack blunting by deviating and splitting the propagating crack along the osteon main direction. In fact, when a crack is propagating perpendicular to an osteon, it will change direction when it reaches a cement line; deflection and twisting act as dissipation mechanisms, resulting in an increase in toughness. Figure 6.3 shows the process of longitudinal and transversal crack

propagation, along with a schematic representation with the osteon geometry.

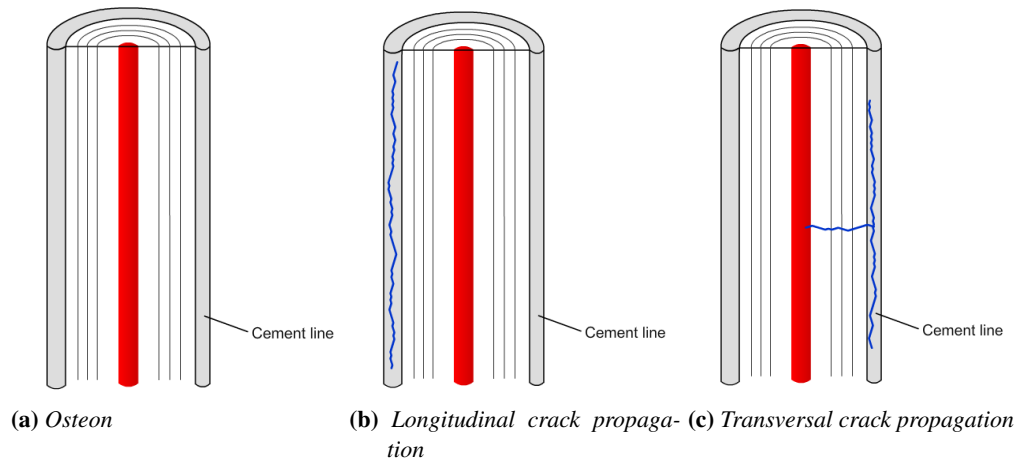


Figure 6.3: Schematic representation of the osteon cylindrical structure and examples of crack propagation in cortical bone (image available from the University of Cambridge). (a) Osteon cylindrical structure: the red line represents the Haversian canal, the concentric lines the lamellae, and the outer line (grey) is the cement line. (b) Example of longitudinal crack propagation (blue) along the cement line of an osteon cylindrical structure. (c) Example of transversal crack propagation (blue) in an osteon cylindrical structure: initial propagation orthogonal to the osteon main axis, and deviation and splitting along the cement line.

In the next sections, we will show the realization of a synthetic composite material, with an internal structure inspired to the one of bone, above described, of the level 5 of bone hierarchy. We choose this structure with the aim of replicating the fracture behavior, and improving the toughness of structural composites. Some simplifications have been introduced to overcome the problems arisen during the manufacturing process.

6.4 Concept

In this section we show the first concept of the osteon-like structure, along with the simplifications introduced, with respect to the materials and manufacturing process available in the composite field at the macroscale. Since the osteon-like composite is a synthetic material, many functions, typical of a living material like bone, cannot be provided. Hence, some simplifications are introduced during the initial design phase, by choosing only the elements, involved in the mechanical behavior, to be replicated, and neglecting those that provide biological living functions. Figure 6.1 shows the microstructure of cortical bone, also known as osteon or Haversian structure. Table 6.2 shows the structural elements of the Haversian structure and their primary function; moreover, it is also shown which functions are chosen to be replicated.

Table 6.2: Analysis of the osteon structure: definition of components along with structure and properties; definition of components to be mimicked in the osteon-like composite

Structural	Elements	Function	Model	
Circumferential system	Outer circumferential lamellae	Package	Yes	
	Inner circumferential lamellae	Bending strength	Yes	
Osteon system	Haversian canal	Primary bloody flow	No	
	Volkman's canal	Secondary bloody flow	No	
	Canaliculi	Secondary bloody flow	No	
	Lacunae	Remodeling	No	
	Osteocytes	Remodeling	No	
	Lymphatic vessels	Nutrients transportation	No	
	Concentric lamellae		Stiffness	In part
			Torsional strength	In part
		Crack deflection	In part	
	Cement lines	Crack deflection	Yes	
Interstitial system	Interstitial lamellae	Ensure compactness	Yes	

6.5 Realization of the Bone-Inspired Material

In this section, we show the final design of the new material. The choice of the materials and the manufacturing process follows.

The osteon structure is simplified for several reasons: costs, manufacturing time, feasibility reasons, compatibility with commercial materials and dimensions of commercial composite laminates.

The characteristic elements of the design of the new composite are the osteons (*i.e.* internal lamellae and cement lines), the interstitial lamellae, and the outer circumferential system. The osteons are reproduced by means of unidirectional bundles of glass fibers (UD-GF), offering resistance to torsional loadings. Rowing of UD-GF are used to mimic the internal part (*i.e.* concentric lamellae) of the osteon. This is a large simplification, since the geometry of the continuous fibers is completely different from that of concentric lamellae; nevertheless, the simplified systems aims to mimic the function of the concentric lamellae. The osteon outer boundaries, called "cement lines", are implemented in the composite by means of $\pm 45^\circ$ carbon fibers (CF) sleeves, which collect and pack the internal part of each osteon, preserving the fiber alignment. Beside offering bending strength, these tubular structures aim to reproduce one of the main properties of bone: the possibility of deflecting and twisting cracks, increasing the energy level required for the crack growth. Interstitial lamellae, which offer compactness and fill up the gaps between osteons, are reproduced by longitudinal UD-GF impregnated into an epoxy resin. The outer circumferential system, which packs the osteon architecture in the human bone, is here replicated by two external layers of non-crimp fabric (NCF), made of UD-GF. These two skins of NCF are placed at the top and bottom of the composite respectively, with the function of packing the internal tubular bio-inspired structure and offering a final flat and uniform surface to the whole composite panel. Here another simplification is introduced, replacing the circumferential structure with a flat one, both for manufacturing reasons and also to allow a larger variety of applications in the structural field as composite panels. Figure 6.4a shows the final structure, after all the above mentioned simplifications; Figure 6.4b, showing the microstructure of cortical bone, allows a direct comparison. Another significant approximation to point out is the scale difference (about one order of magnitude): the osteon size ranges

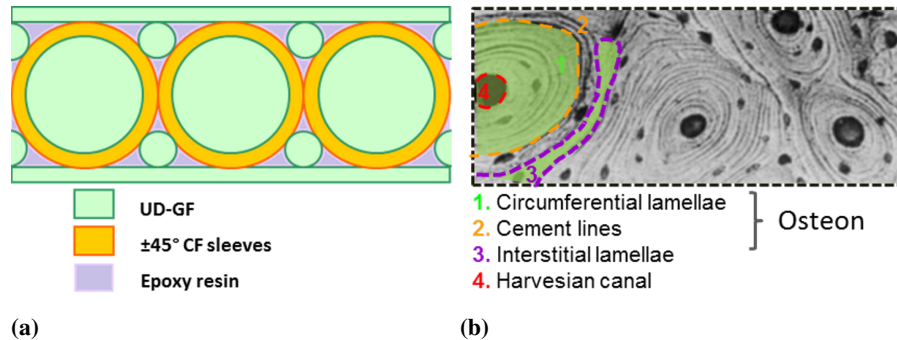


Figure 6.4: Comparison between the structure of the osteon laminate and the microstructure of cortical bone. (a) Representation of the internal structure of the osteon laminate with the designed components. (b) Microstructure of the cortical bone; the most important structural components are color-highlighted. The color corresponds to the mimicked elements in (a).

from 100-200 μm , whereas the osteon size in the bio-inspired composite is about 4-5 mm. A summary scheme, showing the mimicked structural elements and the introduced simplifications, is given in Table 6.3. Beside the bio-inspired material, another laminate is also produced for

Table 6.3: Structural components chosen to be mimicked: design and simplifications.

Osteon structural elements	Biomimetic composite structural elements	Model simplifications
Outer circumferential lamellae	(UD-GF)-NCF	Geometry (flat)
Inner circumferential lamellae	Bundles of UD-GF	Orientation (concentric to UD)
Cement lines	CF-sleeves	Fiber orientation; size
Interstitial lamellae	Bundles of UD-GF + epoxy resin	Orientation

comparative reasons, by using the same materials as reinforcement and matrix. Figure 6.5 shows a schematic example of the bio-inspired composite and that of a classical laminate. In the following, we describe the materials chosen for the new composite structure and for the comparative laminate, and the manufacturing process.

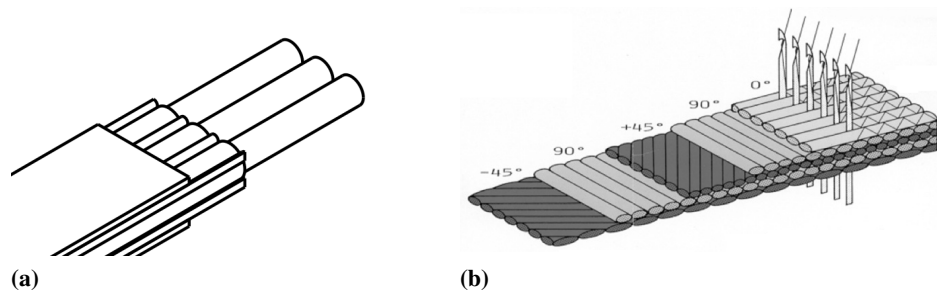


Figure 6.5: Schematic axonometric view of the two realized materials: (a) the internal structure of the osteon laminate with the designed components; (b) the internal structure of a classical laminate with a typical lay-up.

6.5.1 Choice of Materials

The materials are chosen so as to be able to reproduce the designed system and the desired characteristics. Important parameters to be considered are also: the compatibility of the materials with the most common manual lamination techniques, the availability of those materials on the market, and the limited costs. A brief description of the chosen materials follows; technical specifications for all the described materials are given in Appendix C.

6.5.1.1 Material for the Osteons

The materials chosen to replicate the osteons (*i.e.* outer boundaries or cement lines) are carbon fiber sleeves, with a nominal diameter of 5 mm and a $\pm 45^\circ$ lay-up. The woven lay-up and the fiber orientations are chosen so as to provide good torsional properties, whereas the material (carbon) allows to minimize the size of the sleeves ensuring high performance. We would point out that the fiber orientation could be affected by the weaving process, resulting in angles, varying in the $\pm 25\text{-}75^\circ$ range. A representation of the CF-sleeves is given in Figure 6.6a.

6.5.1.2 Material for the Internal Lamellae

Unidirectional glass fibers are chosen for replicating both the internal lamellae and the interstitial ones. The choice of this material is mainly due to low costs and the adaptation to different manual manufacturing techniques. A representation of the UD-GF is given in Figure 6.6b.

6.5.1.3 Material for the Outer Lamellae

To replicate the outer lamellae, two glass fibers skins are chosen to be put at the top and bottom side of the laminate, holding the internal tubular bio-inspired structure and offering a final flat and uniform surface to the whole composite panel. These layers are non-crimp fabric (NCF) made of UD-GF. Fabrics are generally chosen to improve the impregnation process, ensuring an even distribution of the resin across the laminate thickness and width. NCF are stitch-bonded material generally designed to optimally absorb mechanical forces such as pressure and tension. The chosen NCF is "plain", made of UD-GD and stitches placed orthogonally to the fibers direction, as shown in Figure 6.6c.

6.5.1.4 Materials for the Matrix

The type of matrix is chosen on the basis of compatibility with the materials chosen as reinforcement, and of the manufacturing technique initially planned to be used, which is - in the present case - the VARI (Vacuum Assisted Resin Infusion). Epoxy resins are also the most used for structural applications, as explained in Chapter 2, either for their compatibility with a large variety of reinforcement types and for their good mechanical properties.

6.5.1.5 Materials for the Comparative Laminate

For the comparative laminate, all the above described material are used, except for the carbon sleeves; these are replaced by a CF-NCF (Figure 6.6d), with a $\pm 45^\circ$ orientation, to be consistent with the osteon laminate. The volume ratio of the fibers ($\sim 53\%$) and matrix ($\sim 47\%$) is the same for both the osteon- and the comparative-laminate; also, the volume ratio of carbon ($\sim 7\%$) and glass ($\sim 46\%$) fibers is the same for the two material types.

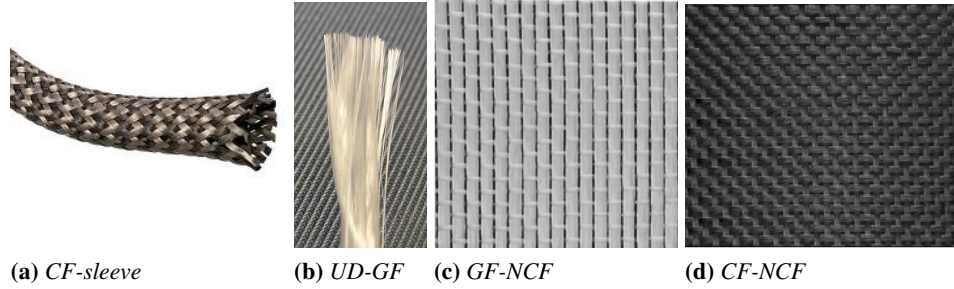


Figure 6.6: Materials used as reinforcement for the osteon laminate and for the comparative laminate. (a) carbon fiber sleeve with a diameter of 5 mm, used to replicate the osteon. (b) UD-glass fibers used for internal part of the osteon and the interstitial regions. (c) NCF made of UD-GF used for the external surfaces of the osteon laminate. (d) NCF with orthogonally oriented CF used only for the comparative laminate.

6.5.2 Manufacturing

6.5.2.1 Manufacturing of the Osteon Composite

The manufacturing phase of both materials is completely carried out in the laboratory of the Clausthal University of Technology, by an MSc student. The manufacturing process of the osteon laminate is more complicated than that of the conventional laminate, due to the assembly of elements with different shapes. In particular, the main difficulty is to correctly put the UD-glass fibers in the sleeves, preserving the fibers alignment, and to hold all the elements together. Three osteon laminates are produced, by gradually improving the manufacturing technique, in terms of lamination time and quality of the end-product. The manufacturing process consists in three main phases: 1) sizing, 2) lamination, and 3) impregnation, here briefly described.

Sizing

In this first phase, the diameter of the sleeves and the proper fiber ratio are determined. According to the producer, the CF-sleeves diameter varies in the 2.5-11 mm range, and also the fiber orientation between 25-75°; see Appendix C. Since different diameters correspond to different fiber orientation, we fix the fiber angle to 45°, and we obtain a sleeve diameter of 4.5 mm. By means of geometrical observations, we determine the correct amount of fibers for the intra- and inter-sleeves regions. We consider A_1 as the intra-osteon area, A_2 the inter-osteon area, and A_3 the sum of them, as simplified in Figure 6.7. Equations 6.1, 6.2, and 6.3 are given below:

$$A_1 = \frac{\pi d^2}{4} \quad (6.1)$$

$$A_2 = \frac{A_3 - A_1}{2} \quad (6.2)$$

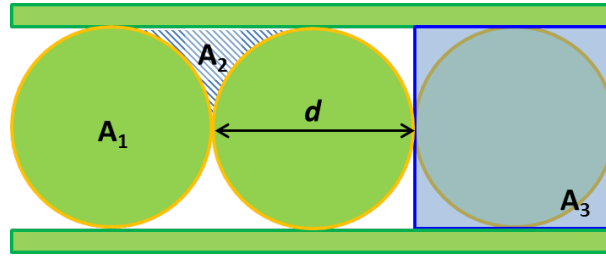


Figure 6.7: Schematic representation of the microstructure of the bone-inspired composite used for the sizing of the fibers; A_1 , A_2 , and A_3 are the three areas to be fulfilled with UD-GF.

$$A_3 = d^2 \quad (6.3)$$

By considering that the same type of fibers are used for the intra- and inter-sleeve area, we calculate the intra/inter fiber ratio, corresponding to 7:1 (see Equation 6.4).

$$r_f = \frac{A_1}{A_2} = \frac{\pi}{4 - \pi} \quad (6.4)$$

Lamination

The method, here called "Long tube sewing frame", is completely manual. It includes the sleeves cut, the filling with the UD glass fibers, the sleeves end-fixing, and the placement of stretched UD glass fibers, with the aid of a sewing frame, to simplify the lamination process and ensure the fiber and the tubes alignment and the laminate compactness; finally the stitching, and the removal of the sewing frame.

A schematic representation of the lamination is given in Figure 6.8, along with the final product, immediately before the impregnation process.

Resin impregnation

The Vacuum Assisted Resin Infusion (VARI) is initially chosen for the resin impregnation, on 110x50 mm plates, where the longer direction corresponds to the principal osteon direction. The curing time is 48 hours at room temperature. After testing three slightly different VARI methods, a new method is defined, to solve the problems arisen during the impregnation testing. The method used for the manufacturing of the osteon laminates lays in between the VARI and the RTM: the resin flow is generated by a vacuum pump, but the resin injection occurs through a mold. This method ensures a uniform impregnation, and a good surface finishing. Figure 6.9 shows the resin impregnation, the curing phase, and one of the final biomimetic laminates.

It should be stressed that, being the manufacturing technique manual, the results are not repeatable, but many defects can be introduced during the process, affecting the quality of the end-product.

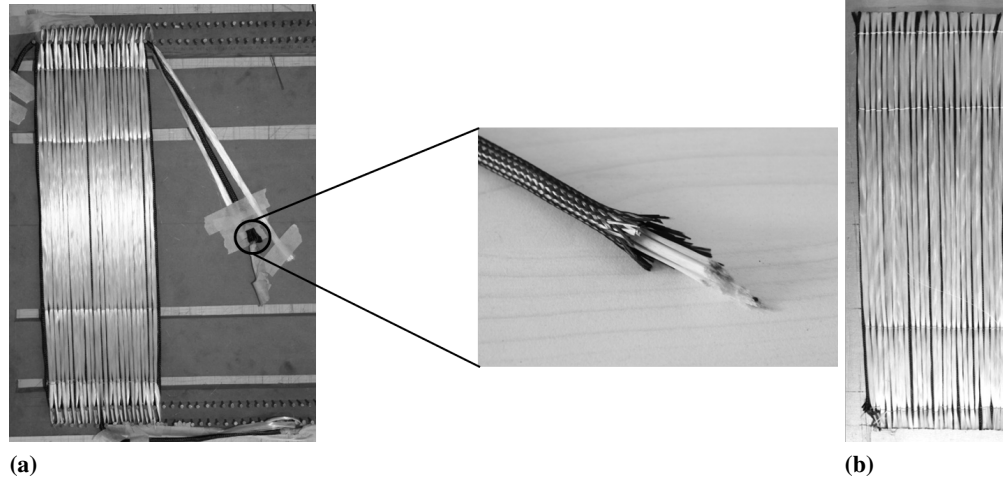


Figure 6.8: Schematic representation of the manual lamination process of the bio-inspired composite: (a) lamination and particular of the osteon-inspired tubular structure; (b) final internal structure before the impregnation process.

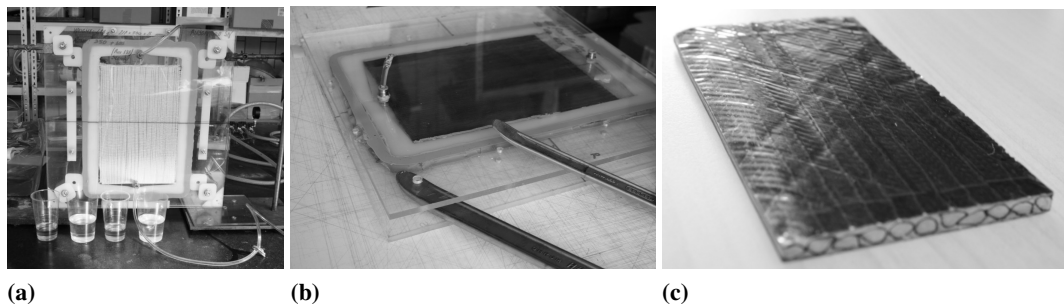


Figure 6.9: Schematic representation of the manual impregnation process of the bio-inspired composite: (a) resin impregnation with resin and hardener; (b) curing, (c) final product.

6.5.2.2 Manufacturing of the Comparative Laminate

The comparative laminate is made by a classical process of manual lamination, by using three types of fibers: 1) (UD-GF)-NCF (the same used for the osteon composite), manually placed; 2) UD-GF (the same used for the osteon composite) placed by means of filament winding; 3) ($\pm 45^\circ$ CF)-NCF. The final laminate has the following stacking sequence:

$$[\text{GF}-(0^\circ)_4, \text{CF}-(\pm 45^\circ)_2, \text{GF}-(0^\circ), \text{CF}-(\pm 45^\circ)]_s$$

UD-glass fibers are mainly placed by filament winding, ensuring a high alignment, except for the two outer layers, at the top and the bottom of the laminate, which are NCF used to ensure a flat surface and a good finishing. The carbon layers have the same orientation of those in the osteon laminate but they are in the form of flat non-crimp fabrics (*i.e.* ($\pm 45^\circ$ CF)-NCF). Figure

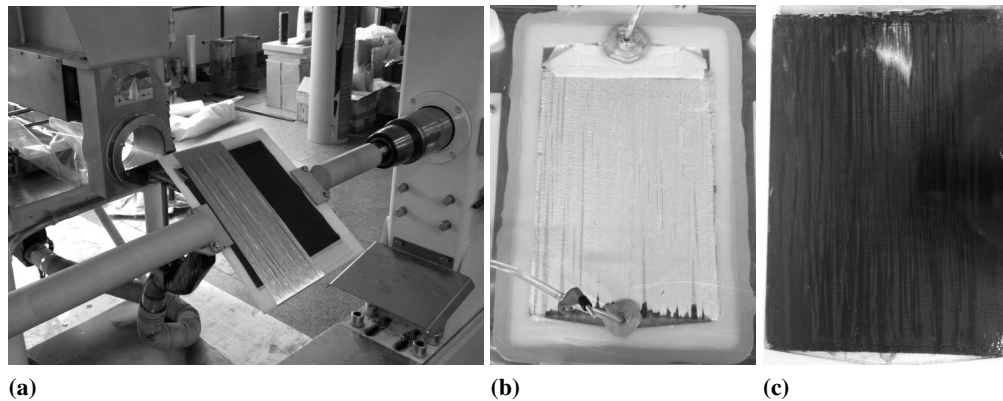


Figure 6.10: Schematic representation of the manual impregnation process of the comparative laminate: (a) resin impregnation with resin and hardener; (b) curing, (c) final product.

6.10 shows part of the lamination process (*i.e.* filament winding), the impregnation, and the final product. Table 6.4 summarizes the manufactured composites and their specifications.

Table 6.4: Technical specifications of the final bio-inspired composite plates (1-2-3) and the comparative laminates.

	Osteon composite 1	Osteon composite 2	Osteon composite 3	Comparative laminate
Thickness [mm]	5	5	5	5
Density [g/cm^3]	1.75	1.82	1.77	1.74
% Vol fiber	54	51	53	54
% Vol CF-fibers	6.4	6.4	6.5	6.3
% Vol GF-fibers	48.2	47	48.3	48.3
% Vol resin	45.4	46.6	45.2	45.4

6.6 Remarks

In this chapter we show the first concept of the osteon-like structure, along with the following simplifications, introduced to the initial design. Large simplifications consist in eliminating those features that provide living functions in bone, since we design a synthetic bio-inspired composite, and concentrating only on structural elements that provide mechanical functions. Further simplifications are introduced in the manufacturing phase, with respect to the materials and manufacturing process available in the composite field at the macroscale. Materials for the new design, and also for the comparative material, are chosen among the most common materials used in composite design for structural applications, for their cost, availability in the market and compatibility with the most common lamination techniques. We briefly describe the adopted manufacturing technique, which leads the final design to a final end product, along with the problems arisen during this phase. The validity of the proposed design is assessed in Chapter 7, by means of an experimental characterization of both the materials, the biomimetic and the conventional composite.

Bibliography

- [1] G. M. Luz and J. F. Mano, “Mineralized structures in nature: Examples and inspirations for the design of new composite materials and biomaterials,” *Composites Science and Technology*, vol. 70, no. 13, pp. 1777–1788, 2010.
- [2] R. O. Ritchie, M. J. Buehler, and P. Hansma, “Plasticity and toughness in bone,” *Physics Today*, vol. 62, no. 6, pp. 41–47, 2009.
- [3] A. Ascenzi and E. Bonucci, “The tensile properties of single osteons,” *The Anatomical Record*, vol. 158, no. 4, pp. 375–386, 1967.
- [4] A. Ascenzi and E. Bonucci, “The compressive properties of single osteons as a problem of molecular biology,” *Calcified Tissue Research*, vol. 2, no. 1 Supplement, p. 44, 1968.
- [5] A. Ascenzi, P. Baschieri, and A. Benvenuti, “The bending properties of single osteons,” *Journal of Biomechanics*, vol. 23, no. 8, pp. 763–771, 1990.
- [6] A. Ascenzi, P. Baschieri, and A. Benvenuti, “The torsional properties of single selected osteons,” *Journal of Biomechanics*, vol. 27, no. 7, pp. 875–884, 1994.
- [7] J. L. Katz, *Mechanical properties of bone.*, vol. 45, pp. 171–184. American Society of Mechanical Engineers, 1981.
- [8] M. E. Launey, M. J. Buehler, and R. O. Ritchie, “On the mechanistic origins of toughness in bone,” *Annual Review of Materials Research*, vol. 40, no. 1, pp. 25–53, 2010.
- [9] R. K. Nalla, J. H. Kinney, and R. O. Ritchie, “Mechanistic fracture criteria for the failure of human cortical bone,” *Nature Materials*, vol. 2, no. 3, pp. 164–168, 2003.
- [10] M. A. Meyers, P. Y. Chen, A. Y. M. Lin, and Y. Seki, “Biological materials: Structure and mechanical properties,” *Progress in Materials Science*, vol. 53, no. 1, pp. 1–206, 2008.
- [11] R. O. Ritchie, J. J. Kruzic, C. L. Muhlstein, R. K. Nalla, and E. A. Stach, “Characteristic dimensions and the micro-mechanisms of fracture and fatigue in ‘nano’ and ‘bio’ materials,” *International Journal of Fracture*, vol. 128, no. 1, pp. 1–15, 2004.
- [12] R. Nalla, J. Kruzic, J. Kinney, and R. Ritchie, “Mechanistic aspects of fracture and r-curve behavior in human cortical bone,” *Biomaterials*, vol. 26, p. 217, 2005.

Chapter 7

Experimental Characterization of the Bone-inspired Composite

This chapter is dedicated to the mechanical characterization of the newly designed composite material, accurately described in Chapter 6. The purpose of this chapter is to assess the mechanical properties of the bio-inspired composite in order to define its potential applications in the structural field. We also compare the mechanical behavior of the bio-inspired material with that of a conventional composite laminate, by performing an experimental characterization of both the materials. The aim of this comparative study is to provide a direct comparison with a typical laminate, used in the structural field, to establish the advantages and shortcomings of the new design with respect to a common design.

7.1 Introduction

Cortical bone, is mainly subjected to flexural and compressive loads. Hence, bone hierarchical structure is organized so as to adapt to those loading conditions and to provide additional functions. Since the biomimetic composite material is inspired to the bone structure and to its response to those loads, we need to determine the mechanical behavior of the new composite, under various loadings, in order to assess the validity of the design described in Section 6. In this chapter, we describe the mechanical characterization of the bio-inspired composite material, subjected to static loadings (tensile, compressive, flexural). Also, the fracture behavior in presence of flaw, which is considered to be the most interesting for the present case, is described. Being the two composites anisotropic, the mechanical response for both the longitudinal and transversal directions is investigated, to allow a comprehensive analysis. All the described tests are carried out in the laboratories of the Department of Mechanical Engineering of Politecnico di Milano.

To investigate whether the new design will be able to reproduce the fracture mechanisms of bone, leading to a toughness improvement with respect to conventional laminates, we also characterize the mechanical behavior of a comparative composite laminate, whose internal organization is described in Chapter 6.

7.2 Experimental Testing

In this section we present all the kinds of tests carried out on the two materials, with a brief description of each test method. All the tests are carried out on both the osteon and the comparative

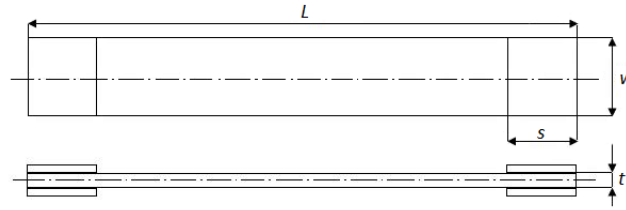


Figure 7.1: Draft showing the geometry of the specimens used for tensile and compressive tests.

laminate, which differ only for the internal structure (*i.e.* organization of the reinforcement). Both the effects of the longitudinal and the transversal direction on the mechanical response are investigated, under tensile, compressive, and flexural loading. Then, the effects of the presence of a crack, orthogonal to the main osteon or fiber direction, is studied through translamellar fracture toughness tests. All the tested specimens are cut from the plates, which are manually produced, and described in Chapter 6.

7.2.1 Tensile Tests

Tensile tests are carried out according to the standard ASTM D 3039/D3039M-08 [1], which provides a test method to determine the in-plane tensile properties of polymer matrix composite materials reinforced by high-modulus fibers. As suggested by the standard [1], the specimens are rectangular and with adhesively bonded tabs at the ends, avoiding stress concentration, due to the grips pressure, and misalignment, thus providing an even stress distribution and a correct load transfer through the grips. Tabs are bonded with Araldite[®] epoxy adhesive. A draft of the tested specimen type is given in Figure 7.1. The dimensions are shown in Table 7.1. We want to point out that some dimensions, such as the thickness, t , and the width, w , are different from those suggested by the standard: the former is due to the thickness of the carbon sleeves, whereas the width is chosen so as to include at least the entire osteons across the width, w , of each specimen. Tensile tests are carried out at room temperature in displacement control mode,

Table 7.1: Nominal dimensions of specimens for tensile tests.

Dimension	Longitudinal	Transversal
Length, L [mm]	250	175
Thickness, t [mm]	5	5
Width, w [mm]	20	25
Tab length, s [mm]	80	35

with a cross-head speed of 2 mm/min. Specimens are clamped in the grips of the machine, with a pressure of 20 MPa, and a data acquisition frequency of 5 Hz is used. Two tensile testing machines are used: 1) for the longitudinal samples, the Schenck hydraulic machine, endowed with a load cell of 250 kN; 2) for the transversal samples, the MTS Landmark ServoHydraulic machine endowed with a load cell of 100 kN. Force-strain data are determined by means of an extensometer: an MTS 634.06H with a gage length of 50 mm and a maximum extension of 25 mm for the longitudinal samples, and an MTS 634.31F-24 with a gage length of 50 mm and an extension up to 4 mm for the transversal ones. An example of the testing setup is shown in Figure 7.2a.

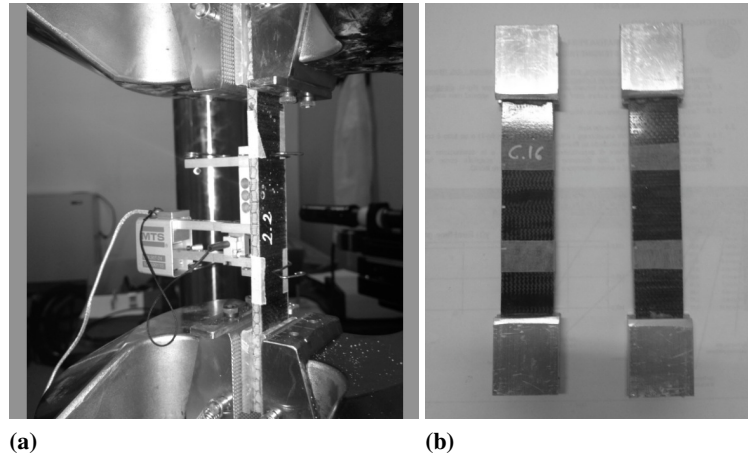


Figure 7.2: (a) *Experimental setup of a tensile test; the sample is clamped into the grips and an extensometer is placed.* (b) *Examples of specimens to be tested.*

7.2.2 Compressive Tests

Compressive tests are carried out according to the standard ASTM D3410/D 3410M-03 [2], which describes a test method to determine the in-plane compressive properties of polymer matrix composite materials reinforced by high-modulus fibers. As required by the standard [2], the specimens are rectangular and with adhesively bonded tabs at the ends, avoiding stress concentration, due to the grips pressure, and misalignment, thus providing an even stress distribution and a correct load transfer through the grips. Tabs are bonded with Araldite® epoxy adhesive. A draft of the tested specimen type is given in Figure 7.1. The dimensions are shown in Table 7.2. Also for compressive specimens some dimensions, such as the thickness, t , and the width, w , are different from those suggested by the standard: the former due to the thickness of the carbon sleeves, whereas the width is chosen so as to have at least the entire osteons in the specimen cross-section. Compressive tests are performed at room temperature in displacement

Table 7.2: *Nominal dimensions of specimens for compressive tests.*

Dimension	Longitudinal	Transversal
Length, L [mm]	155	150
Thickness, t [mm]	5	5
Width, w [mm]	15	25
Tab length, s [mm]	67.5	65

control mode, with a cross-head speed of 1.5 mm/min. Specimens are clamped in the grips of the machine, with a pressure of 20 MPa, and a data acquisition frequency of 5 Hz is used. According to the standard [2], it is recommended to endow the specimen with a lateral driving system, to improve the alignment and to avoid buckling failure. In this case, we perform the tests without the lateral guide because no buckling problem arises. The experimental setup is shown in Figure 7.3.

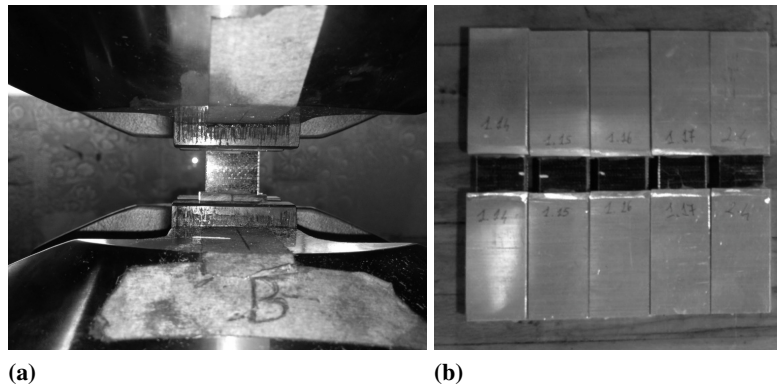


Figure 7.3: (a) Experimental setup of a compressive test with the sample clamped into the grips. (b) Samples to be tested.

7.2.3 Flexural Bending Tests

Flexural bending tests are carried out according to the standard UNI-EN ISO 14125 [3], which specifies a method for determining the flexural properties of FRP-composites under three-point and four-point loading. In [3] standard test specimens are defined, but additional parameters are included for alternative specimen sizes for use where appropriate; also, a range of test speeds is included.

In this work, the three-point-bending configuration is chosen. As required by the standard [3], the specimens are rectangular. The dimensions are shown in Table 7.3. A draft of the tested specimen type and the loading configuration is given in Figure 7.4. Tests are performed

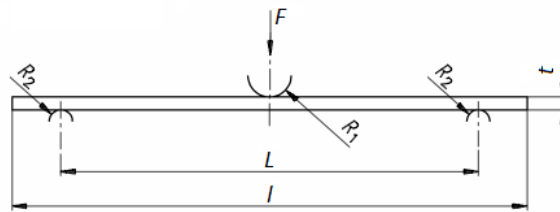


Figure 7.4: Drawing of the three-point-bending configuration.

Table 7.3: Nominal dimensions of specimens for three-point bending tests.

Dimension	Longitudinal	Transversal
Length, L [mm]	150	150
Thickness, t [mm]	5	5
Width, w [mm]	20	15
Support Span Length, l [mm]	100	100
Supporting Roll Diameter, R_1 - R_2 [mm]	5-5	5-5

at room temperature, in displacement control mode with a cross-head speed of 2 mm/min, by using a universal tensile testing machine MTS Alliance RT-100. Each specimen is supported by two bearing rolls and subjected to bending loading by applying an axial compressive load at its center, by a third bearing load induced by the cross-head displacement. The cross-head speed is constant until the deflection reaches a prefixed limiting value, or until failure occurs. The purpose of this test is to obtain force-deflection data: force data are acquired through the load cell (HBM U10M with a nominal force up to 25 kN), whereas the mid-span deflection data through a deflectometer (MTS model 632-06H-30). Data acquisition frequency is set to 5 Hz. Due to the large deflection, we apply two lateral supports to limit the transversal displacement of the load bearing rolls. The experimental setups, before and after applying the additional supports, are shown in Figure 7.5.

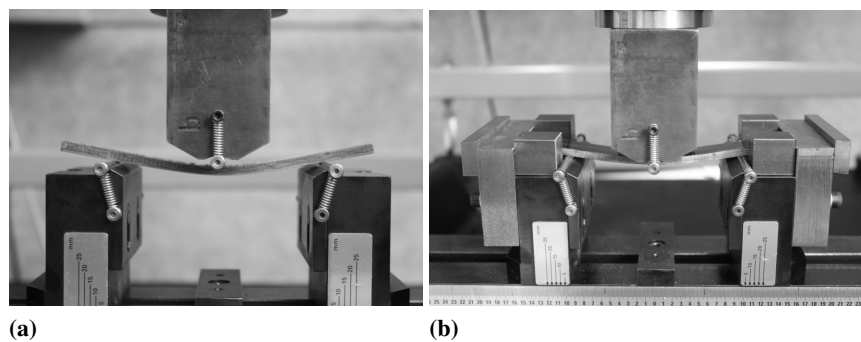


Figure 7.5: *Three-point-bending tests: experimental setup. (a) Initial setup. (b) Final setup with two lateral supports to limit the transversal displacement of the load bearing rolls.*

7.2.4 Translaminar Fracture Toughness Tests

Translaminar fracture toughness tests are carried out according to the standard ASTM E1922-04 [4], which describes a method for the determination of translaminar fracture toughness, K_{TL} , for laminated and pultruded polymer matrix composite materials of various ply orientations, using test results from monotonically loaded notch specimens. This method involves single-edge-notch, ESE(T), specimens in opening mode loading. According to [4], K_{TL} values, determined with this test, can quantitatively establish the effects of fiber and matrix variables and stacking sequence of the laminate on the translaminar fracture resistance of composite laminates. Also this type of test can serve as a method to investigate how the fracture propagate in the bio-inspired composite and in the comparative laminate, allowing a final comparison.

Specimens are cut following the geometry and dimensions suggested by the standard [4]; for this kind of test there are no requirements for the thickness. A diamond impregnated copper slitting saw is adopted to create a narrow notch. The geometry and dimensions of the tested specimens are shown in Figure 7.6. Pin-loading clevises are used to apply the load to the specimens, as shown in Figure 7.7a. A displacement gage is used to measure the displacement at the notch mouth during loading. The gage is attached to the specimen using knife edges, adhesively bonded to the specimen. Tests are performed at room temperature, in displacement control mode with a cross-head speed of 1 mm/min, by using a universal tensile testing machine

MTS Alliance RF-150, endowed with a load cell of 90 kN. Data acquisition frequency is set to 20 Hz. The experimental testing setup is shown in Figure 7.7b.

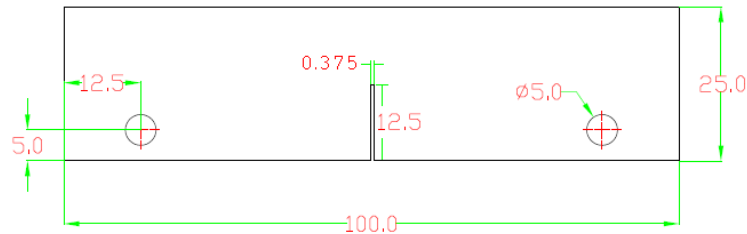


Figure 7.6: Drawing of the ESE(T) specimen for translaminal fracture toughness tests.

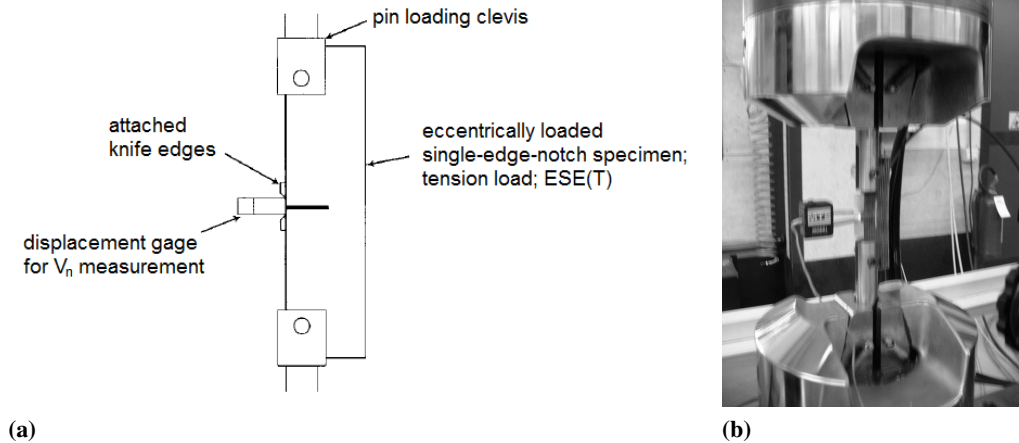


Figure 7.7: (a) Test arrangement for translaminal fracture toughness tests: load is applied through pin clevises and a displacement gage, mounted on knife edges, is used to measure the notch opening displacement (adapted from [4]). (b) Experimental setup of translaminal fracture toughness tests.

7.2.5 Interrupted Fracture Toughness Tests

Beyond translaminal fracture toughness tests, carried out according to the standard [4], we also performed interrupted translaminal fracture toughness tests. We use the specimens with the same geometry and size of those described in Section 7.2.4. Tests are performed at room temperature, in displacement control mode with a cross-head speed of 1 mm/min, by using a servohydraulic testing machine, MTS Landmark, endowed with a load cell of 100 kN. The load is not monotonically applied, as in the tests described in Section 7.2.4, but interrupted every 0.5 kN, for few minutes, to allow microscopic analyses. For the microscopic analyses an optical microscope, endowed with LEICA DFC 290 lens, is used; a computer, connected to the microscope, is used for image acquisition and also to monitor the crack propagation during the test. The experimental setup is shown in Figure 7.8.

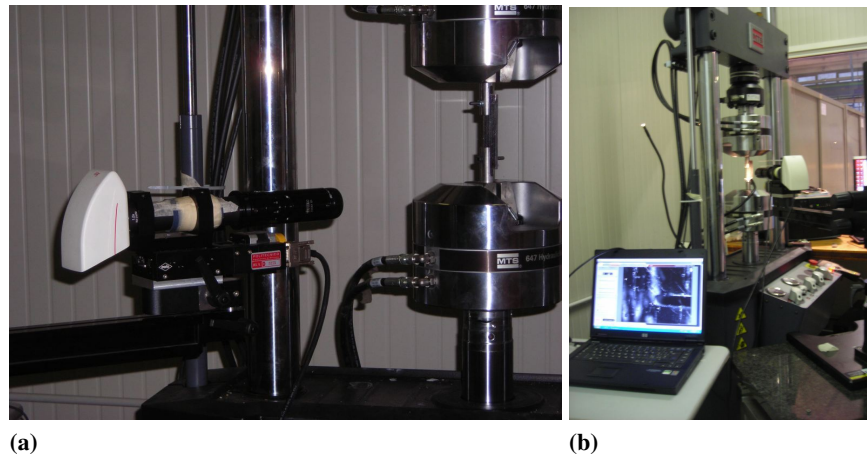


Figure 7.8: (a) Test arrangement for the interrupted translamina fracture toughness tests: an optical microscope is placed in front of the specimen surface and connected to a computer to monitor the crack growth. (b) Image acquisition, during an interrupted translamina fracture toughness test, with a computer connected to the optical microscope.

7.2.6 Microscopic Analyses

The specimens subjected to the translamina fracture toughness tests, described in Section 7.2.4, are then analyzed by means of a scanning electron microscope (SEM). The specimens are cut in the vicinity of the zone where the crack has propagated and observed with an SEM Evo 50 EP Zeiss by Oxford Instrument. The SEM has a maximum magnification of $10^5\times$ and it is endowed with a spectrometer, allowing for an energy dispersive X-ray spectroscopy (EDS), an analytical technique used for the chemical characterization of the samples. Thanks to this instrument, it is possible to obtain secondary electrons topographic-contrast images of the samples, or images with contrast between areas with different chemical compositions, by means of backscattered electrons (BSE). Sample surfaces need to be accurately prepared, cleaned and made conductive in case of non metallic materials. In this study, we clean the sample surfaces and make them electronically conductive, by sputter-coating with a conductive material (*i.e.* gold), then we observe the surface with an SEM.

7.3 Results

In the following, we present the results obtained from all the previously described tests. In each section, the results of the tests in longitudinal and transversal directions for both the materials, the bio-inspired composite and the comparative composite, are shown. We show a representative curve for each specimen type, ensuring repeatability of results, with a direct comparison between the two materials.

7.3.1 Tensile Tests

Tensile tests are basic tests that allow one to determine the elastic modulus, the tensile strength and the elongation at breakage. The elastic modulus is determined, as prescribed by the standard [1], as the slope of the stress-strain curve in the deformation range 0.1-0.3 %. Figure 7.9

shows the stress-strain curve for two longitudinal specimens: the osteon-like material and the comparative laminate. For the sake of brevity, being the results repeatable, only one representative curve for each specimen type will be given. A comprehensive comparison is then given in Table 7.4, where the average results are shown.

In the longitudinal direction, the behavior of both the materials is approximately linear. The osteon-like material shows a linear elastic region followed by a bumping region immediately before failure. In this region the load is slightly increasing and the damage is progressively spreading across the specimen volume. Failure occurs due to delamination at the osteon interface and debonding between the fibers and the matrix, either inside and outside the osteons. At the end, failure of UD glass fibers and failure of carbon sleeves occurs. In fact, the final rupture occurs at 45° for the carbon part, and orthogonally for the glass fibers (see Figure 7.10a). The tensile strength is about 800 MPa, and the elastic modulus 50 GPa, 40% more than the comparative composite. The comparative material has a linear behavior, with lower characteristics than the osteon-composite. Failure occurs mainly to delamination between the carbon layers; other damages, barely visible, affects the external layers of UD-GF (see Figure 7.10b).

In the transversal direction, the behavior of the two materials are similar, showing a consistent reduction of the mechanical properties. For the osteon structure, the behavior is linear; the transversal elastic modulus is three times less than the longitudinal one, whereas the reduction in strength is about 30 times. Damage propagates through the thickness and failure occurs at the osteon-osteon interface. In fact, this is a weak region, due to the transversal orientation of both the osteon tubes and the glass fibers. The comparative laminate shows an initial linear behavior, allowing the measurement of the transversal modulus, slightly inferior to the one of the osteon composite; then the slope slightly decreases until breakage. Also in this case, a brittle failure occurs, but at a stress level more than twice that of the osteon material. The results are summarized in Table 7.4. For some of the results, shown in Table 7.4, the standard deviation (St.Dev.)

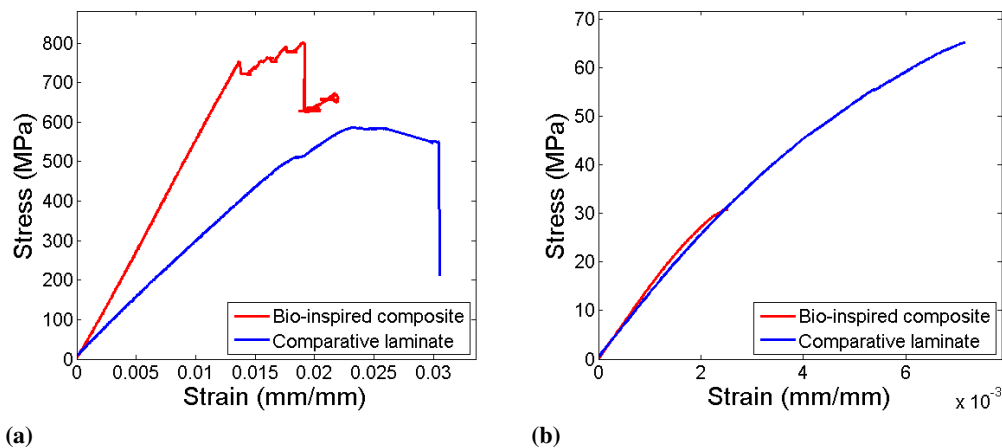


Figure 7.9: Comparison between the tensile behavior of the bio-inspired composite and that of the comparative laminate. (a) Stress-strain curve for the tensile tests on longitudinal configurations. (b) Stress-strain curve for the tensile tests on transversal configurations.

and the coefficient of variation (CV %) are not given, because the number of valid tests are not enough. In fact, in some cases, detaching of the adhesively bonded tabs or problems during testing, make the test not valid.

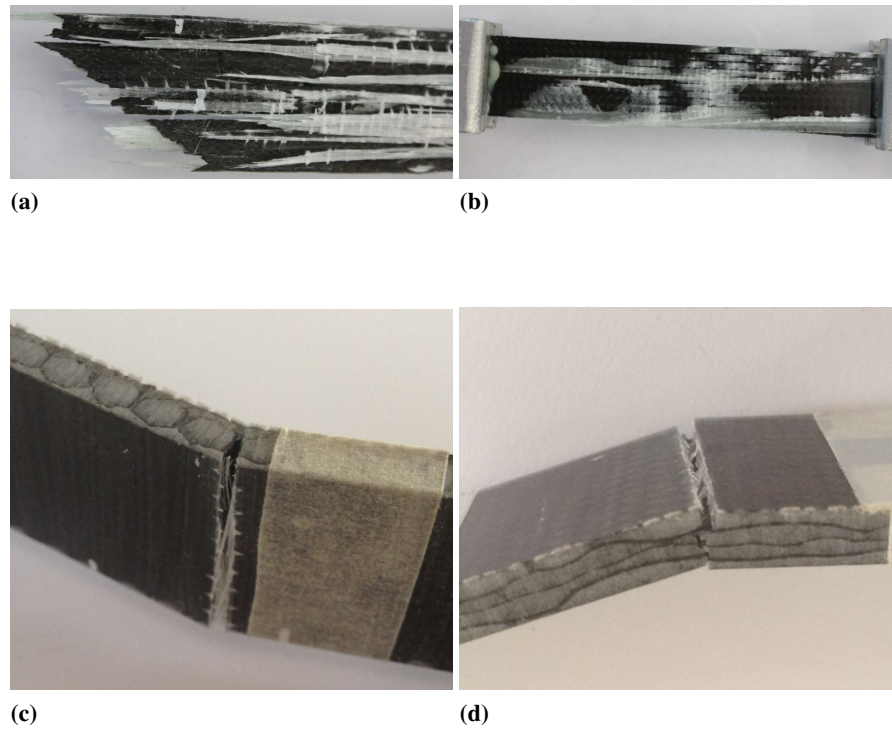


Figure 7.10: Longitudinal tensile tests: failure mode of the bio-inspired composite (a) and of the comparative laminate (b). Transversal tensile tests: failure mode of the bio-inspired composite (c) and of the comparative laminate (d).

Table 7.4: Results of tensile tests on the bio-inspired composite and on the comparative laminate, in both longitudinal and transversal directions.

		Longitudinal		Transversal	
		Bio-inspired composite	Comparative laminate	Bio-inspired composite	Comparative laminate
σ_R (MPa)	Average	797	568	28	65
	St.Dev.	53	10	3	-
	CV %	6.7	1.8	9.0	-
E (MPa)	Average	46864	33245	14558	12366
	St.Dev.	4981	-	972	-
	CV %	10	-	7	-

7.3.2 Compressive Tests

Compressive tests show a better behavior for the conventional laminate compared to the osteon composite, in both longitudinal and transversal directions.

In longitudinal compressive tests, the conventional laminate shows an average compressive strength 30% higher than that of the osteon structure. This is mainly due to the weak osteon-osteon interface. Indeed, for the osteon material, the strongest point in longitudinal tensile and flexural loading, here is the weakest point. The $\pm 45^\circ$ CF-layers have a load bearing role in compression, whereas in the osteon structure the effect of the $\pm 45^\circ$ CF-layers is reduced, due to slipping at the CF-sleeves interface. The longitudinal behavior for both the materials is shown in Figure 7.11a. Although the conventional laminate has a higher strength, the compressive stiffness, considered as the slope of the stress-displacement curves, is higher for the osteon structure. Failures occur at the osteon-osteon interface ("splitting"), in the bio-inspired structure, and for delamination between the layers in the laminate (Figure 7.12a and 7.12b). It is interesting to note that the failure mode of the bio-inspired material is similar to the splitting that occurs in human bone. Like for human bone, which is far more difficult to break than it is to split [5], also the bone-like composite seems easier to be divided than it seems to be broken, being the osteon-osteon interface the weakest part.

Similar results are obtained in the transversal direction (see Figure 7.11b), where the conventional laminate shows a higher resistance in compression compared to the osteon structure. Also in transversal direction, failure occurs at the osteon-osteon interface for the bio-inspired material and due to debonding and matrix failure in compression for the laminate. The effect of the marked anisotropy, due to the long tubular structures, is consistent also in compression. Failure modes, after transversal compressive tests, are shown in Figure 7.12c and 7.12d.

All the results of compressive tests are summarized in Table 7.5. We want to stress that more precise and reliable results can be obtained by using an appropriate lateral driving system, to improve the alignment and to avoid buckling failure, as suggested by the standard [2].

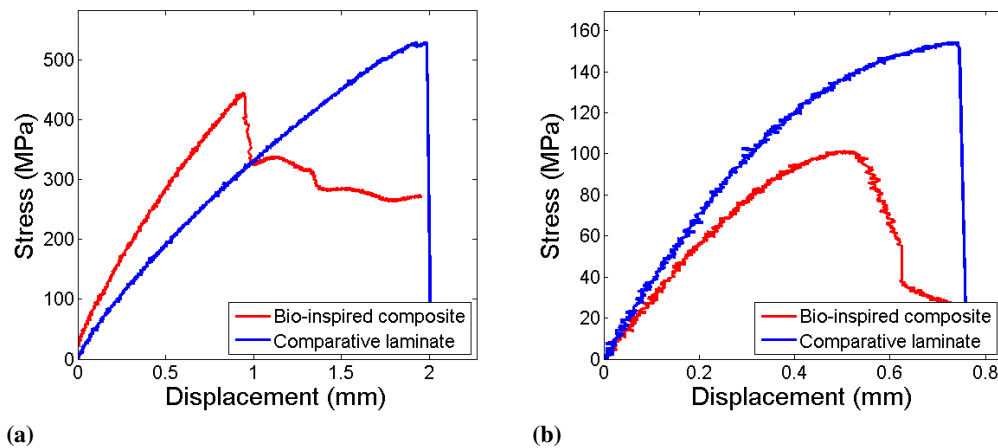


Figure 7.11: Comparison between the compressive behavior of the bio-inspired composite and that of the comparative laminate. (a) Stress-strain curve for the compressive tests on longitudinal configurations. (b) Stress-strain curve for the compressive tests on transversal configurations.

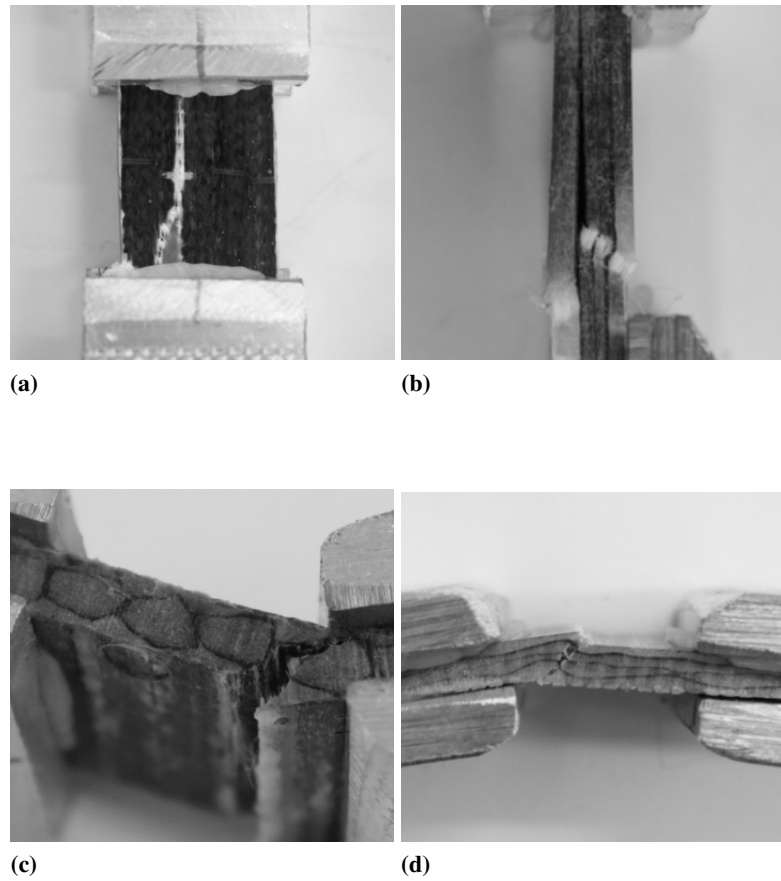


Figure 7.12: Longitudinal compressive tests: failure mode of the bio-inspired composite (a) and of the comparative laminate (b). Transversal compressive tests: failure mode of the bio-inspired composite (c) and of the comparative laminate (d).

Table 7.5: Results of compressive tests on the bio-inspired composite and on the comparative laminate, in both longitudinal and transversal directions.

		Longitudinal		Transversal	
		Bio-inspired composite	Comparative laminate	Bio-inspired composite	Comparative laminate
R_c (MPa)	Average	416	581	101	157
	St.Dev.	32.5	47.8	2.3	2.4
	CV %	7.8	8.2	2.2	1.5

7.3.3 Flexural Bending Tests

These tests are particularly important for the evaluation of the bio-inspired structure. Indeed, human bone is largely subjected to flexural stresses.

Three point bending tests show a completely different behavior between the two structures: in the longitudinal direction the bending strength of the bone-like composite is 15% more than that of the conventional laminate, and the bending stiffness is 42% higher than that of the laminate. The difference is principally due to the failure modes, which in turn depend on the internal organization. A peculiarity of the osteon-like material is that it does not show a catastrophic brittle failure; instead, it is characterized by a progressive failure, with damage evolution and growing. This phenomenon corresponds, on the stress-deflection curve, to a bumping region, as shown in Figure 7.13a. This region is not characterized by a drop in strength, but as the first damages appear, the whole specimen section seems not to be affected by them, maintaining its load-bearing capability. Observing the bone-like material during testing, we suppose that this behavior is due to that damages progressively affect different building blocks of the material: first the osteons, causing splitting and slipping at their interface; then the external layers, where the stress reaches its maximum, and finally the longitudinal GF. Indeed, the glass fibers breakage causes the final rupture of the material. The progressive failure is an advantage of the bio-inspired material; indeed, in case of structural applications, it allows the damage to be monitored and estimation on the residual life to be made, avoiding catastrophic failure and ensuring safety.

The classical laminate, instead, shows a completely linear behavior until breakage (Figure 7.13a). This behavior is typical of brittle fiber-reinforced composites. Failure mainly occurs by delamination at the interface between different layers.

Like the tensile and compressive behaviors, also the flexural behavior is affected by the marked anisotropy of the bio-inspired composite. Therefore, as expected, this material shows lower properties under transversal flexural loadings, in terms of bending stiffness and strength, due to the internal arrangement, which does not ensure continuity. In fact, the classical laminate has a bending strength three times higher than that of the osteon composite, and a bending stiffness 37% higher. In transversal tests, the osteon structure shows a purely linear behavior until rupture, whereas the laminate is not linear (Figure 7.13b). The former is due to the matrix, which plays a crucial role in this loading configuration, the latter instead, is due to the contribution of the various layers. In the case of the laminate, the stress-deflection curve can be divided in three parts: the first and the last parts, approximately linear, and one part in between, which connects the two slope changes. This curve represents the mode of failure and the contribution given by each component to the material. We suppose that in the first part, the load bearing contribution is given by the external $\pm 45^\circ$ carbon layers; in the middle part, the non linearity is due to the matrix contribution; finally in the last part, which corresponds to a macroscopic damage of the material, the middle $\pm 45^\circ$ carbon layers, subjected to compression, contribute to sustain the load. We suppose that fracture initiates where the maximum tensile stress is reached (*i.e.* at the opposite side to that where the load is applied), then propagates through the thickness. The failure modes of the two tested materials under longitudinal and transversal loading are shown in Figure 7.14. In these tests, the bending stiffness is calculated following the standard [3], by considering the data corresponding to the deformation range of 0.05-0.25%. Also, since in the transversal three point bending tests on the comparative laminate there was a high deflection, 10% higher than the support span length, a modified formula, suggested by the standard [3], is used to calculate the stress, including the effect of the curvature. The results of the three-point bending tests are summarized in Table 7.6.

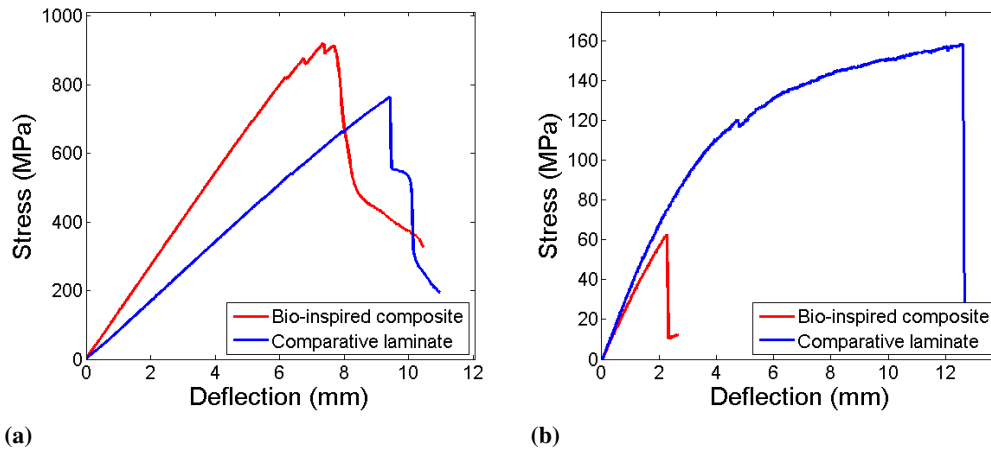


Figure 7.13: Comparison between the flexural behavior of the bio-inspired composite and that of the comparative laminate. (a) Stress-strain curve for the three-point bending tests on longitudinal configurations. (b) Stress-strain curve for the three-point bending tests on transversal configurations.

Table 7.6: Results of three-point-bending tests on the bio-inspired composite and on the comparative laminate, in both longitudinal and transversal directions.

		Longitudinal		Transversal	
		Bio-inspired composite	Comparative laminate	Bio-inspired composite	Comparative laminate
σ_f (MPa)	Average	880	782	59	156
	St.Dev.	30	26	3	4
	CV %	3.4	3.4	5.1	2.4
E_f (MPa)	Average	44296	31108	10585	14583
	St.Dev.	2195	595	2061	104
	CV %	5.0	1.9	19.5	0.7
Max deflection (mm)	Average	7.6	9.2	2.2	12.0
	St.Dev.	0.3	0.3	0.2	0.8
	CV %	4.0	3.2	9.0	6.5

7.3.4 Translaminar Fracture Toughness Tests

These tests are particularly interesting for the evaluation of the toughness of the bio-inspired structure and for the investigation of the fracture behavior. Human bone contains a large amount of cracks and maintains its load-bearing functions in spite of those cracks [6–8]. Synthetic composites, being non-living materials with a non-hierarchical structure show significant differences.

Figure 7.15 shows the load-displacement curves for two specimens: the osteon-like material and the comparative laminate. For the sake of brevity, being the results repeatable, only one

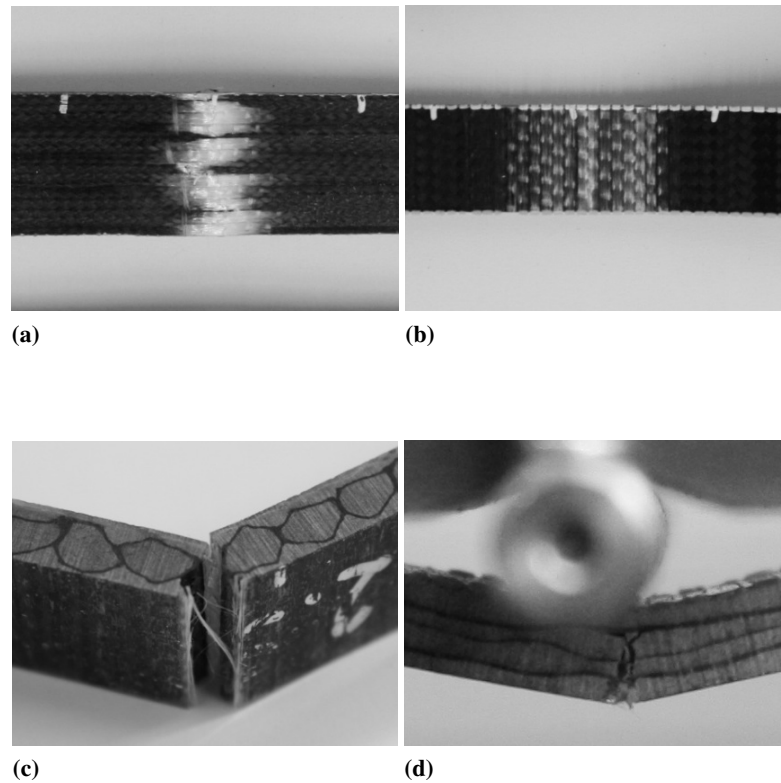


Figure 7.14: Longitudinal bending tests: failure mode of the bio-inspired composite (a) and of the comparative laminate (b). Transversal bending tests: failure mode of the bio-inspired composite (c) and of the comparative laminate (d).

representative curve for each specimen type is given. Then, a comprehensive comparison is given in Table 7.7, in terms of fracture toughness and strength.

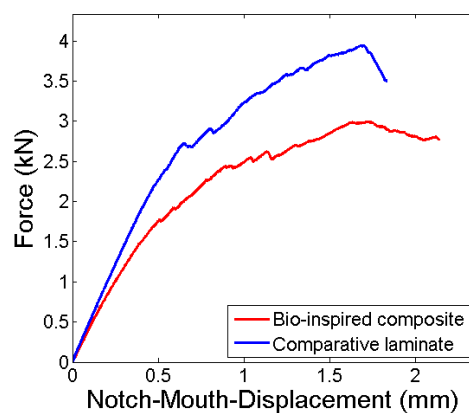


Figure 7.15: Comparison between the fracture behavior of the bio-inspired composite and that of the comparative laminate. Force - Notch-mouth-displacement curves for both the materials.

Table 7.7: Results of the translaminar fracture toughness tests on the bio-inspired composite and on the comparative laminate.

		Bio-inspired composite	Comparative laminate
K_{TL} (MPa \sqrt{m})	Average	26.87	32.68
	St.Dev.	2.93	1.12
	CV %	10.89	3.43
σ_{max} (MPa)	Average	379.32	452.07
	St.Dev.	43.55	16.89
	CV %	11.48	3.74

According to the standard [4], fracture toughness, E_{TL} , is calculated by means of Equation 7.1:

$$K_{TL} = (P/BW^{1/2})\alpha^{1/2}(1.4+\alpha)(3.97-10.88\alpha+26.25\alpha^2-38.9\alpha^3+30.15\alpha^4-9.27\alpha^5)/(1-\alpha)^{3/2} \quad (7.1)$$

where:

K_{TL} = applied stress intensity factor, MPa \sqrt{m} ;

P = applied load, MN;

α = crack aspect ratio, a/W , dimensionless, ($0 \leq \alpha \leq 1$);

a_n = notch length, m;

B specimen thickness, m;

W specimen width, m.

The average values of translaminar fracture toughness, determined for both the materials are given in Table 7.7. The results are comparable: however, the comparative laminate has a slightly higher fracture toughness (about 18%) than that of the bone-inspired composite. The same for the strength, which is 16% higher for the comparative laminate. It is interesting to note that the strength of the material in presence of crack is less than half of the strength of the material with a flawless section (*i.e.* by comparing it with the case of longitudinal tensile tests shown in Section 7.3.1), while in the case of the laminate it is 20% less. The lower value of translaminar fracture toughness for the bone-inspired material is due to the reinforcement, which is predominantly longitudinal; also, being the $\pm 45^\circ$ carbon fibers in a tubular shape, they do not contribute to prevent the crack growing, as in the comparative laminate, where they are flat textiles (*i.e.* NCF). In the osteon-structure an inter-osteon reinforcement, able to keep together the tubular structure working as a unique system, is missing. It is likely that the osteons create a discrete system, with a lack of continuity.

On the other hand, by looking at the failure mode, the osteon-like structure reproduces the "splitting" mode. Figure 7.16 shows the failure of both the biomimetic composite and the laminate. The initial notch, a_n , is highlighted with a white line, and the crack path with a red dashed

line. The conventional laminate fails for fiber-matrix debonding, and delamination: in Figure 7.16b we can see a longitudinal crack path, due to fiber-matrix debonding in the longitudinal layer, and a visible damaged area, ahead the crack tip; also, various small spread damages (of subsurface layers) are visible over all the specimen surface. In the case of the osteon-like material, the crack seems to propagate along the interface region between two osteons that is the weak region. To confirm this hypothesis, interrupted fracture toughness tests, monitored with an optical microscope are carried out. The results are shown in Section 7.3.5.

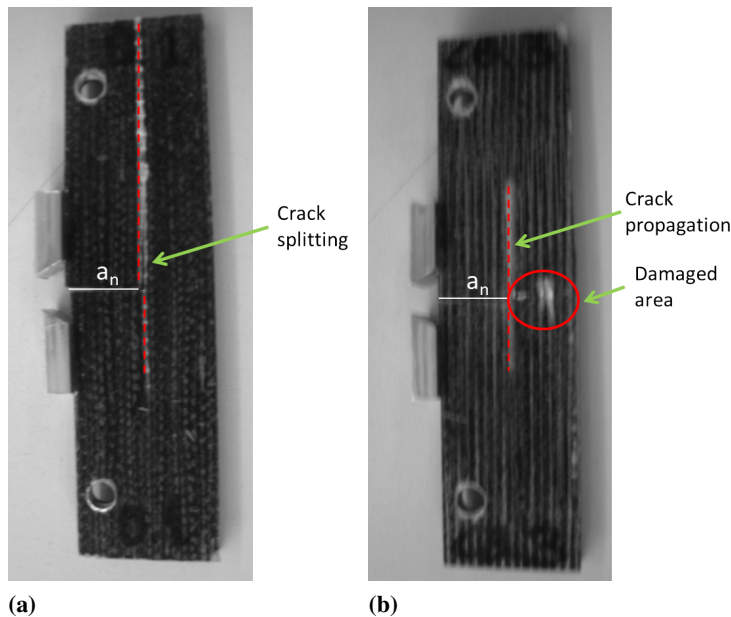


Figure 7.16: Comparison between the fracture behavior of the bio-inspired composite and that of the comparative laminate; the red dashed lines show the cracks. (a) Failure of bio-inspired composite: crack splitting. (b) Failure of the comparative laminate: crack propagation and damaged area near crack tip region.

7.3.5 Interrupted Fracture Toughness Tests

Interrupted fracture toughness tests allows the fracture process to be followed, by means of an optical microscope. The test is stopped for few second, maintaining the load constant, to allow the acquisition of microscopic images. Also in these tests, the osteon-like material shows the expected "splitting" mode of failure, as shown in Figure 7.17. Figure 7.18 shows the microscopic images, after each step of an entire test. The main cracks and the small ones, visible during the test, are highlighted with red dashed lines. The main cracks, which cause splitting leading to failure, are highlighted with yellow dashed lines. During the test it is possible to follow, thanks the microscope tools, the damage process, and to understand the failure mode in the osteon-like material. To understand the effect of the osteon structure, we also create initial notches with different elongation, and with the crack tip ending in either in the inter-osteon region and in the intra-osteon region. In the former case, the crack easily propagates along the osteon-osteon interface; in the latter, the crack first propagates in the matrix, perpendicular to the applied load, and then it deviates along the osteon-osteon interface leading to splitting.

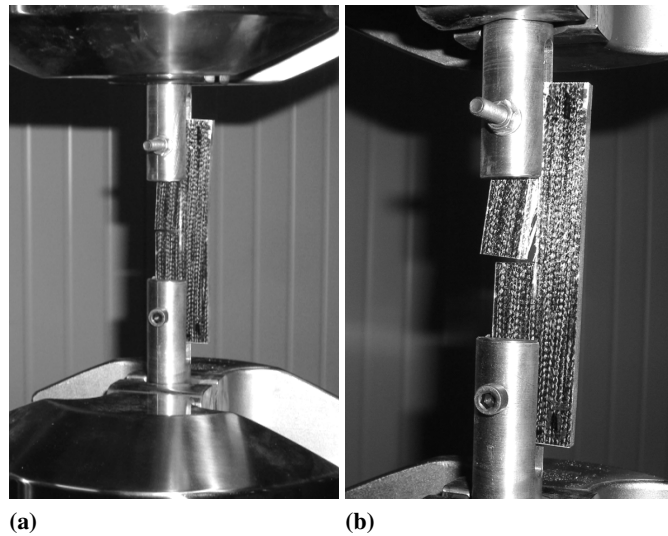


Figure 7.17: Pictures of the interrupted fracture toughness tests on the bio-inspired laminate. (a) Crack splitting during the test. (b) Failure.

To confirm this hypothesis, we also look at the microstructure, by cutting the specimens and observing the cross-section with an SEM.

7.3.6 Microscopic Analyses

The results of microscopic analyses for the bone-like composite and the comparative laminate are shown in Figure 7.19 and Figure 7.20, respectively. The images are referred to cross sections close to the failure regions. Figure 7.19a shows a cross section far from the crack path, whereas Figure 7.19b-7.19d shows the region where the main crack propagates; the crack region is highlighted with a dashed red line circle and the crack path with a dashed red line. Here the phenomenon of crack deviation and splitting is clearly visible. The crack, initially propagates in the intra-osteon region, then it deviates along the cement line. This process is very similar to the one described in Section 6.3.2 and shown in Figure 6.3. Figure 7.20 instead, shows the cross section of a specimen of comparative laminate. The section, being close to the failure region, shows many large damages, which affect the UD-GF layers. The carbon layers, which are the darker and thinner layers, do not show large damages. The UD-GF layers, especially those obtained by filament winding, show fiber-matrix debonding, fiber rupture and matrix failure. The SEM images confirm that in this material the damage is spread over the cross section of the material.

7.4 Remarks

Results are summarized in Table 7.8 for comparison, whereas Table 7.9 shows the advantages of the two materials. The new designed biomimetic composite shows a different mechanical behavior, owing to the different internal organization. The osteonic structure has been shown to have a positive effect in the osteon longitudinal direction in terms of stiffness and strength, except for the compressive strength. In transversal direction it shows some drawbacks, but

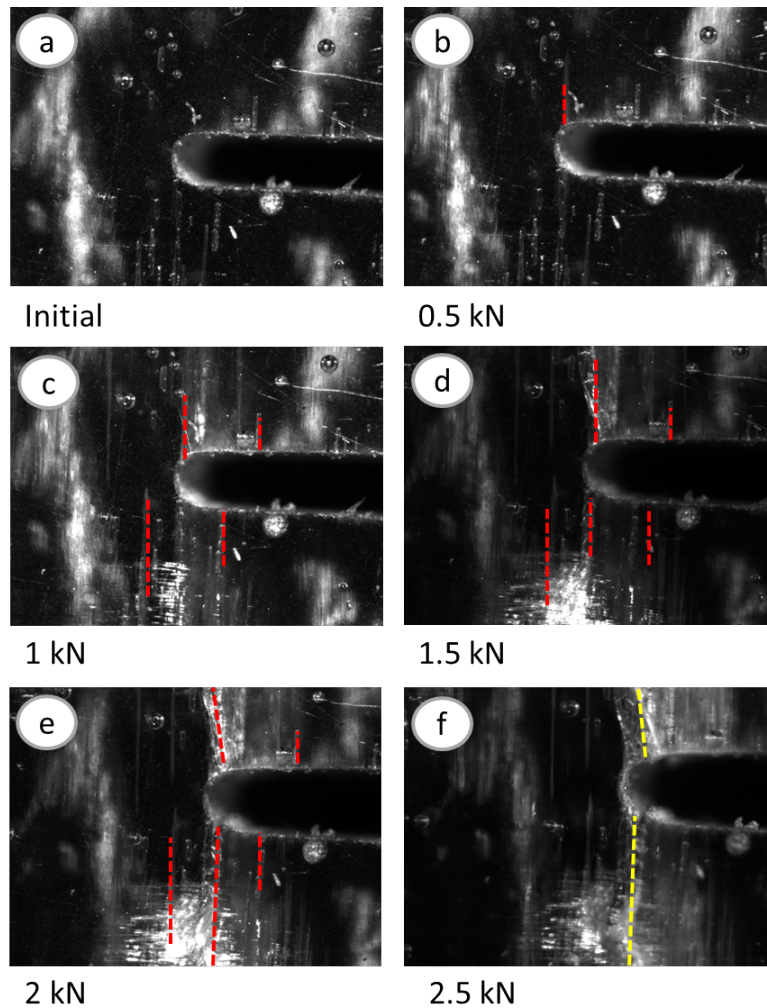


Figure 7.18: Microscopic images showing the region near the crack tip, during the interrupted fracture toughness tests on the bio-inspired laminate. The red dashed lines in subfigures (a)-(e) show the cracks formation and propagation. The yellow dashed lines in subfigure (f) show the main cracks propagation, leading to splitting failure mode.

maintaining a higher tensile stiffness compared to the conventional laminate. Hence, the classical composite generally performs better in transversal direction. This is due to the layered structure, where the interplay of various layers has revealed to play a crucial role in enhancing the transversal properties. This material also shows a slightly better response to fracture in presence of a crack, as shown by the translaminal fracture toughness tests. However, the failure mode of the new osteon-like composite has shown to replicate the crack splitting and deviation, typical of bone, though its shortcomings.

We believe that further improvements of the initial proposed design may allow one to overcome the limits in transversal direction response and enhance the fracture properties, leading to a biomimetic material with high performance.

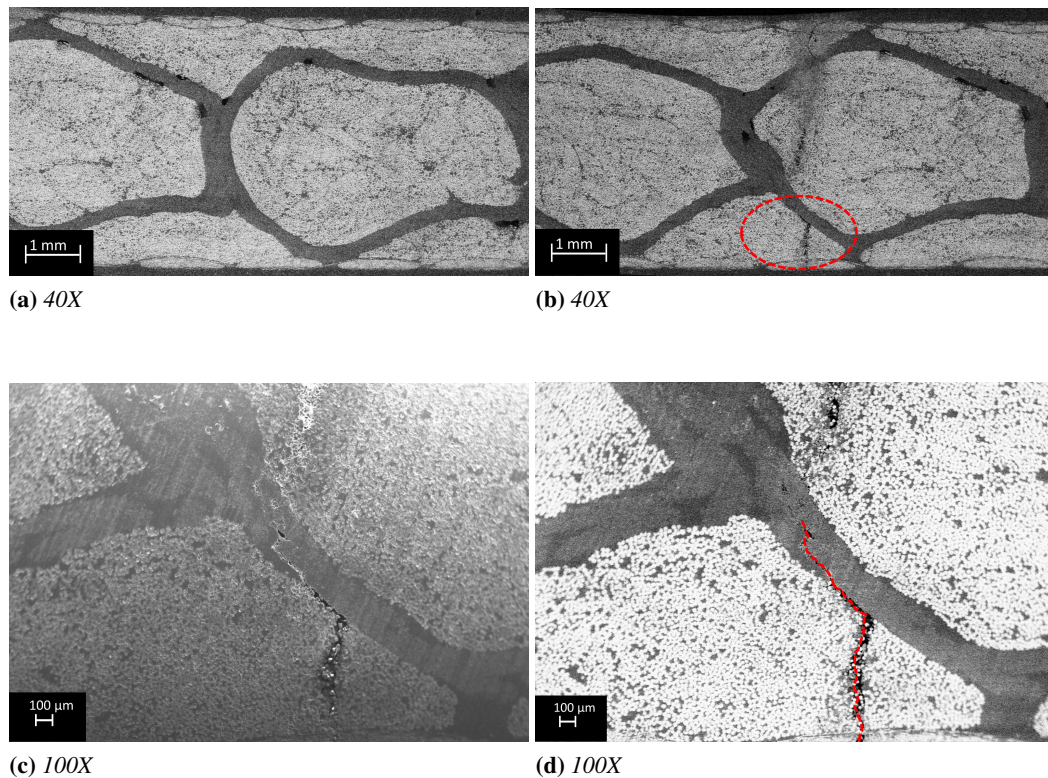
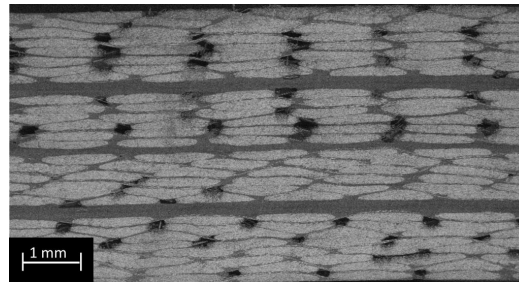
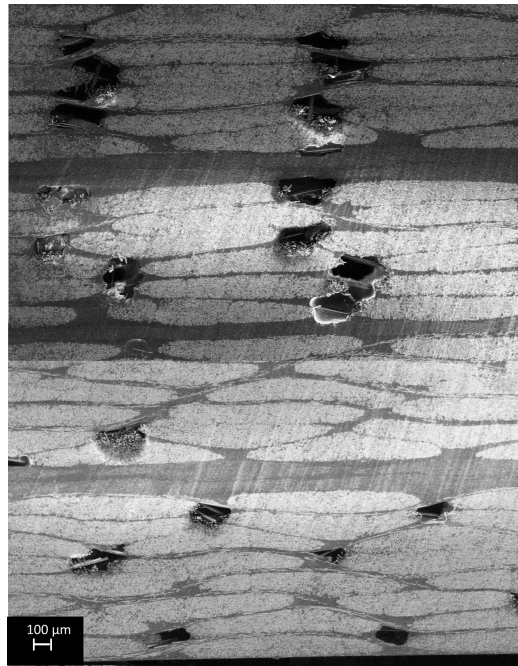


Figure 7.19: SEM images - with magnitude 40X and 100X - showing a cross-section of a specimen (bio-inspired material). (a) The image (from backscattered electrons) shows a region far from the crack propagation area. (b) The image (from backscattered electrons) shows the region where the main crack propagates; the crack region is highlighted with a dashed red line circle. (c) The image (from secondary electrons) shows the crack deviation, from the intra-osteone to the inter-osteone region. (d) The image (from backscattered electrons) shows the crack deviation, from the intra-osteone to the inter-osteone region; the crack path is highlighted with a red dashed line.



(a) 40X



(b) 100X

Figure 7.20: SEM images (from backscattered electrons) - with magnitude 40X and 100X - showing a cross-section, close to the cracked region, of a specimen (comparative laminate material). (a) The image, referred to the whole section, shows spread damages across the surface. (b) Union of two SEM images with an increased magnitude (100X).

Table 7.8: Results of the experimental testing conducted on the bio-inspired composite and on the comparative laminate, in both longitudinal and transversal directions.

Property	Unit	Longitudinal		Transversal	
		Bio-inspired composite	Comparative laminate	Bio-inspired composite	Comparative laminate
Tensile strength	(MPa)	797	568	28	65
Compressive strength	(MPa)	416	581	101	157
Flexural strength	(MPa)	880	782	59	156
Tensile modulus	(MPa)	46864	33245	14558	12366
Compressive modulus	(MPa)	↑	↓	↓	↑
Flexural modulus	(MPa)	44296	31108	10585	14583
Translaminar fracture toughness	(MPa \sqrt{m})	26.87	32.68	-	-
Fracture strength	(MPa)	379	452	-	-

Table 7.9: Final comparison between the bio-inspired composite and the comparative laminate, in both longitudinal and transversal directions.

Direction	Material type	Advantages
Longitudinal	Bio-inspired composite	Strength (tensile, flexural) Stiffness (tensile, compressive, flexural)
	Comparative laminate	Strength (compressive, fracture) Translaminar fracture toughness
Transversal	Bio-inspired composite	Stiffness (tensile)
	Comparative laminate	Strength(tensile, compressive, flexural) Stiffness(compressive, flexural)

Bibliography

- [1] D3039/D3039M-08, “Standard test method for tensile properties of polymer matrix composite materials,” 2008.
- [2] D3410/D3410M-03, “Standard test method for compressive properties of polymer matrix composite materials with unsupported gage section by shear loading,” *ASTM*, 2008.
- [3] 14125, “Fibre-reinforced plastic composites - determination of flexural properties,” *UNI EN ISO*, 2011.
- [4] E1922-04, “Standard test method for translaminar fracture toughness of laminated and pultruded polymer matrix composite materials,” *ASTM*, 2010.
- [5] R. O. Ritchie, M. J. Buehler, and P. Hansma, “Plasticity and toughness in bone,” *Physics Today*, vol. 62, no. 6, pp. 41–47, 2009.
- [6] R. Nalla, J. Kruzic, J. Kinney, and R. Ritchie, “Mechanistic aspects of fracture and r-curve behavior in human cortical bone,” *Biomaterials*, vol. 26, p. 217, 2005.
- [7] K. J. Koester, J. W. Ager, and R. O. Ritchie, “The true toughness of human cortical bone measured with realistically short cracks,” *Nature Materials*, vol. 7, no. 8, pp. 672–677, 2008.
- [8] M. E. Launey, M. J. Buehler, and R. O. Ritchie, “On the mechanistic origins of toughness in bone,” *Annual Review of Materials Research*, vol. 40, no. 1, pp. 25–53, 2010.

Part IV

Conclusion

Chapter 8

Conclusion

The objective of this work is to develop an integrated numerical-experimental biomimetic approach, to design a bio-inspired composite material. In particular, the new design proposed in this study is inspired to the intriguing structure of bone. Bone is a hierarchical composite material with a great combination of mechanical properties. In particular, bone is well known for its remarkable toughness, though it is mainly made of brittle mineral crystals (*i.e.* hydroxyapatite). This research consists of studying the hierarchical organization of bone, focusing on its structure-property relationship; in particular, analyzing the origin of its toughening mechanisms (relevant in the nano-to-micro scale range), with the aim of being reproduced in the design of a new bio-inspired composite. At the nanoscale an atomistic approach is used to study the mechanical properties of bone building blocks, the collagen organic fibers, the hydroxyapatite mineral crystals and their nanocomposites. From atomistic simulations we get information about the mechanical behavior of bone basic components, their interactions and the size effect on their mechanical performance, and in particular on the fracture behavior of the theoretically brittle mineral components. Simulation results have revealed the crucial role played by the interface interactions in the overall mechanical properties of such nanocomposites, and the large effect of confinement on both the collagen-hydroxyapatite nanocomposites and on the hydroxyapatite single crystals. The concept of confinement is very common for natural materials, confirming the importance of characteristic size in smart natural systems. At the meantime, a biomimetic approach is used to design and realize a new material, with the aim of replicating some of the toughening mechanisms operating in bone and harnessing them in engineering materials. In particular, to replicate the crack deflection and twisting mechanisms, occurring in bone at microscale, we propose a design inspired to the microstructural level of bone (*i.e.* osteon structure), with carbon fiber sleeves replacing the osteons and unidirectional glass fibers replacing the lamellae, all embedded into an epoxy resin. The proposed structure is then characterized under different loading conditions, and the results are compared with those obtained from the characterization of a comparative material (*i.e.* a classical laminate with the same type and amount of fibers and resin).

8.1 Remarks and Conclusions

In this study we show the possibility of realizing a *de novo* material, by copying the smart natural system of bone following an integrated numerical-experimental biomimetic approach. A schematic of this approach is given in Figure 8.1. The study of bone structure has remarked the importance of the hierarchical organization in determining the mechanical properties of bone

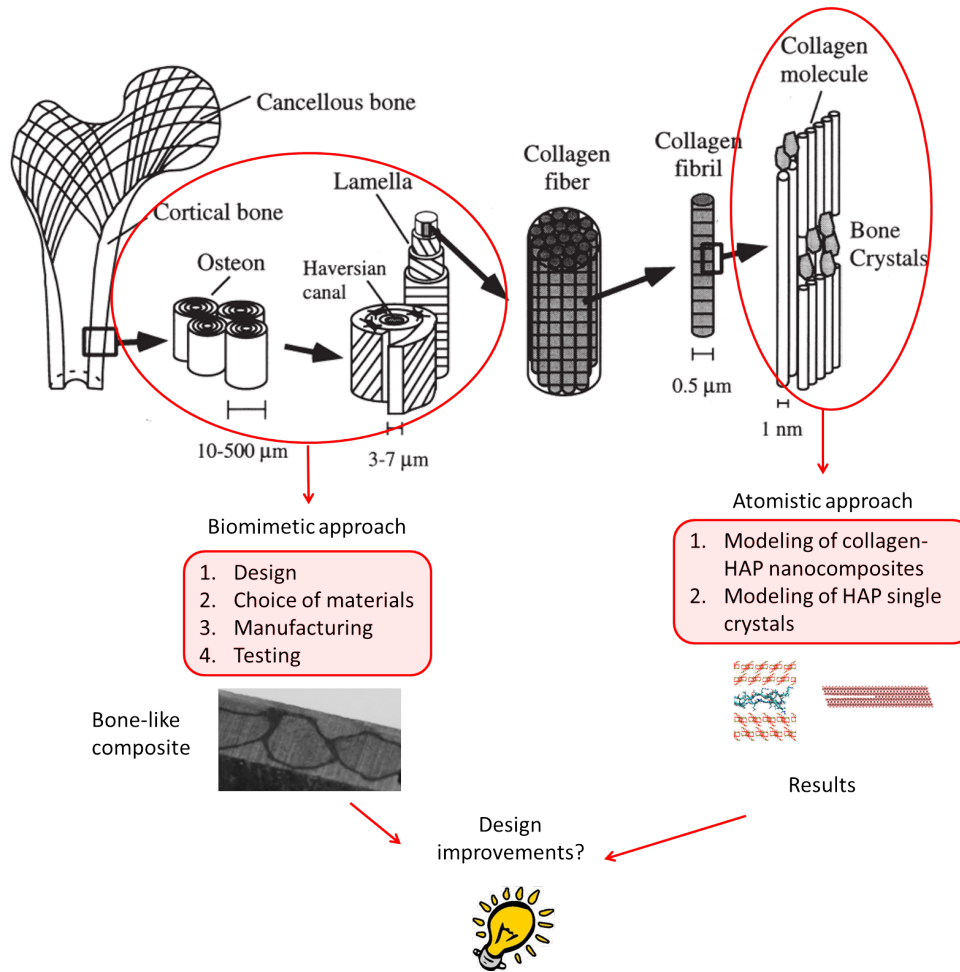


Figure 8.1: Drawing of bone hierarchical structure [1] and scheme of the research approach followed in this study.

tissue. The multilevel organization of bone explains its multifunctional properties: indeed, the different level organization allows for adaptation to different functions.

The strong structure-property relationship is also investigated through molecular dynamics simulations. The results of the atomistic study has revealed: *i*) the importance of collagen-hydroxyapatite surface interactions, enhanced by the presence of water, in load transfer (*i.e.* by shear), stiffness, strength, elastic stability and on the overall mechanical properties of the nanocomposite system, *ii*) the role of the confined size of these nanocomposite structures in enhancing the mechanical performance of the system, and *iii*) the role of the nanometer size of the mineral crystals in fracture response, ensuring high strength and a maximum tolerance of flaws.

Simulations of collagen-hydroxyapatite nanocomposites allows one to study the behavior of bone from an atomistic point of view. The results of these simulations have confirmed the importance of the presence of water, which mediates the interactions between the protein and the mineral, acting as a lubricant, hence increasing the interface shearing properties and the overall mechanical performance of the nanocomposite system. Also, the size confinement of the nanocomposite system has been shown to significantly increase the performance of the whole structure. Indeed, according to previous studies [2], it is not only the building blocks that make

Table 8.1: Final comparison between the bio-inspired composite and the comparative laminate, in both longitudinal and transversal directions.

Property	Type	Longitudinal		Transversal	
		Bio-inspired composite	Comparative laminate	Bio-inspired composite	Comparative laminate
Strength	Tensile	↑			↑
	Compressive		↑		↑
	Flexural	↑			↑
	Fracture		↑	-	-
Modulus	Tensile	↑		↑	
	Compressive	↑			↑
	Flexural	↑			↑
Translaminar fracture toughness			↑	-	-

bone so resilient. At an atomistic and molecular scale, the size effect plays a main role in determining the mechanical behavior of bone, leading to new phenomena, which do not occur at larger levels. Another important result of this study is the crucial role played by the intermolecular hydrogen bonds, in determining the resistance against slip. These bonds, present both in the collagen triple helix (intermolecular) and between the collagen and the hydroxyapatite (intramolecular), act as sacrificial bonds, and their continuous formation and breaking, acting as an energy dissipation medium, lead to an increase in the composite resistance to failure. This finding confirms previous studies [3].

Simulations, carried out on hydroxyapatite mineral crystals, show an increase in strength and toughness by systematically reducing the crystal size. We determine a critical size, corresponding to 4.15 nm, a value that indicates the threshold below which the material is insensitive to the presence of flaws. Indeed, in this case the material fails in a non-brittle mode, showing a homogeneous stress-field without high-stress concentration at the crack tip, and failure is governed by its theoretical strength rather than by the classical Griffith criterion of fracture propagation. This may allow one to think that nature selects the nanometer size to ensure an optimal combination of fracture strength and toughness.

Our results provide details on the mechanism of load transmission in collagen-hydroxyapatite nanocomposites, which can be mimicked in the design of bio-inspired composites for engineering applications. Indeed, in the second part of this study a first design of a bone-inspired material is proposed. On the basis of the observation of the microstructure of cortical bone, selected structural features of bone, the osteons, characteristic of the secondary haversian structure (*i.e.* μm to mm), are implemented in a new glass-carbon/epoxy synthetic composite, which could replicate the toughening mechanisms of crack deflection and twisting.

The osteon-like structure is chosen for the simple geometry and for the role played in enhancing the toughness, by deflecting and twisting the crack. Conventional structural materials, widely used in the field of composites, such as glass fibers, carbon fibers and epoxy matrix, are chosen for the new structural material. Some simplifications are introduced in the initial design to make it feasible, with respect to the available manufacturing process. The material, realized by manual lamination, is experimentally characterized, under tension, compression,

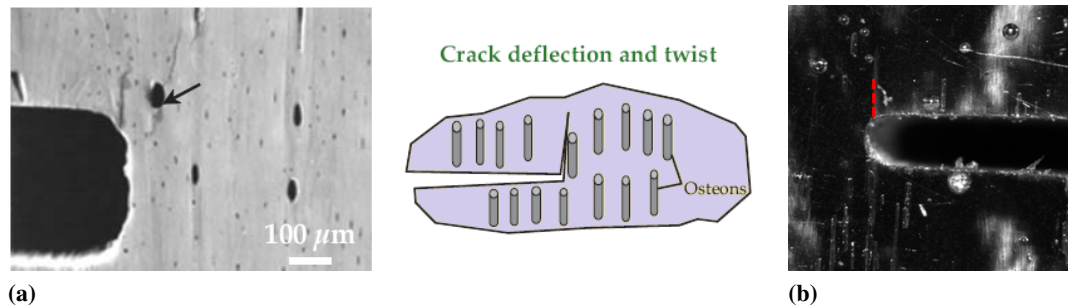


Figure 8.2: Comparison of the crack deflection mechanism in bone and in the bone-like material. (a) Crack deflection mechanism in bone: micrography and schematic [4]. (b) Crack deflection mechanism in the bone-like material: picture from the optical microscopy, during an interrupted fracture toughness test.

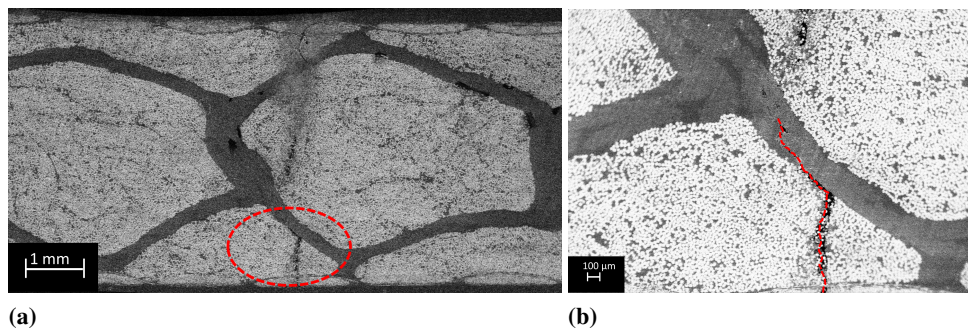


Figure 8.3: SEM images (from backscattered electrons) - with magnitude 40X and 100X - showing a cross-section of a specimen of the bone-inspired material. (a) The image shows the region where the main crack propagates; the crack region is highlighted with a dashed red line circle. (b) The image shows the crack deviation, from the intra-osteon to the inter-osteon region; the crack path is highlighted with a red dashed line.

and flexural loading, according to ASTM standards, and compared to a conventional laminate (built with the same type and ratios of raw materials) used for comparison. The results of the characterization are summarized in Table 8.1. The bio-inspired material has shown to behave differently from a traditional laminate. The difference are mainly due to the internal organization. In particular, the new composite generally shows better characteristics than the other one, in the osteon longitudinal direction, whereas the transversal direction has shown to be its weak point.

It is interesting to note that in longitudinal direction the osteon structure does not fail in purely brittle mode, in spite of its strongly anisotropy and brittle constituents. In fact, in both tensile and flexural loading conditions, the new material is characterized by a progressive damage, involving each osteon, before final failure occurs, making it suitable for structural applications. It is interesting to see how failure of each structural element (*i.e.* osteon) occurs separately from each other, and in sequence, progressively increasing the energy required for failure. We also perform microscopic analyses on the materials cross sections, to get an insight into the fracture process. These analyses show a phenomenon of crack deviation similar to that

occurring in bone (see Figure 8.2). In fact, during the translaminal fracture toughness tests, the crack path shows a deviation from the intra-osteon to the inter-osteon region (see Figure 8.3). Although the mechanisms of crack deviation has shown a significant similarity with that of bone, the design of the bone-inspired material need to be optimized.

Also, we should point out that the experimental results are affected by the internal defects present in both the materials. However, the bio-inspired material is manually produced for the first time, with a lot of difficulties and problems arisen during the process; the conventional laminate instead, is a well known process. An improvement in the manufacturing process will certainly lead to a decrease in the amount of defects and a consequent improvement of the mechanical behavior. The concept of bio-inspired material, presented in this study, is not meant to be a mere copy of what is found in nature, but instead it should provide a smart solution for engineering problems. Until now, it is only a first solution, which needs further improvements. Suggestions for improvements can be given by the results of atomistic simulations.

8.2 Future Work

The understanding of the mechanisms and the nature's secrets governing the interactions and the behavior of collagen-hydroxyapatite nanocomposites and the failure of such nanoconfined systems, can shed light on the design of the bone-inspired composite, leading to an improvement in the initial design. Also, the new findings on nanoconfined size of hydroxyapatite crystals can give an important contribution in the development of a new solution, providing further improvements.

In view of the obtained simulation results, the proposed design could be optimized, by adding reinforcing nano-structural platelet elements with proper aspect ratio and characteristic sizes, as suggested by the results of full atomistic simulations discussed in Chapter 5. These nanoparticles aim to reproduce the stiffening and toughening effects given by hydroxyapatite platelets in bone. Furthermore, since the surface interactions have revealed to play a significant role on the mechanical behavior of collagen-hydroxyapatite nanocomposite, a "glue-like system", providing "sacrificial local failure", can also be introduced in the new design to improve the interface strength, mimicking the role played by hydrogen bonds and porosity in the bone nanocomposites.

By observing the Haversian structure of bone and the mechanical behavior of the first proposed solution, we realize that the weak point of the bone-like composite is the mechanical response in transversal direction. Therefore, to improve the transversal behavior we need to enhance the osteon-osteon interactions, for instance by creating a multi-layer osteon structure, allowing simultaneous inter-osteon interactions in different directions (see Figure 8.4b). Another possible solution can be given by the addition of a weave composite fabric, alternatively placed under and over each osteon (see Figure 8.4c). Schematics of the initial solution and of some proposed improved solutions are given in Figure 8.4.

As discussed above, on the basis of the simulation results, we propose further improvements focused on two main aspects:

- the enhancement of the interface strength, by using a "glue-like" system;
- the inclusion of platelet like nanoparticles with a high aspect ratio, to enhance the surface interaction and the related mechanisms, aimed to play the role that hydroxyapatite plays in bone.

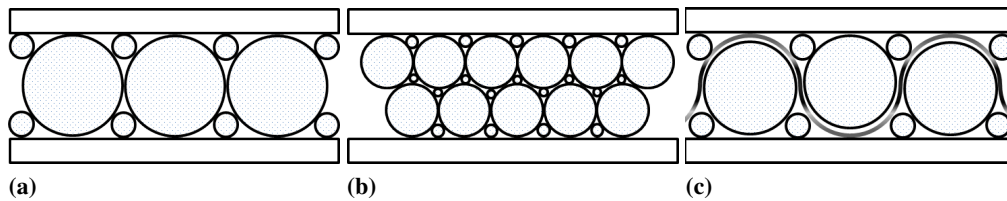


Figure 8.4: Schematic solutions of the internal structure of the bone-inspired composite. (a) Initial solution object of the present study. (b) Alternative proposed solution: multi-layer osteon structure. (c) Alternative proposed solution: inter-osteon woven layer to improve the osteon-osteon interactions, limiting their slipping.

These concept are clearly explained in Figure 8.5, where a schematic of the atomistic-based design is given.

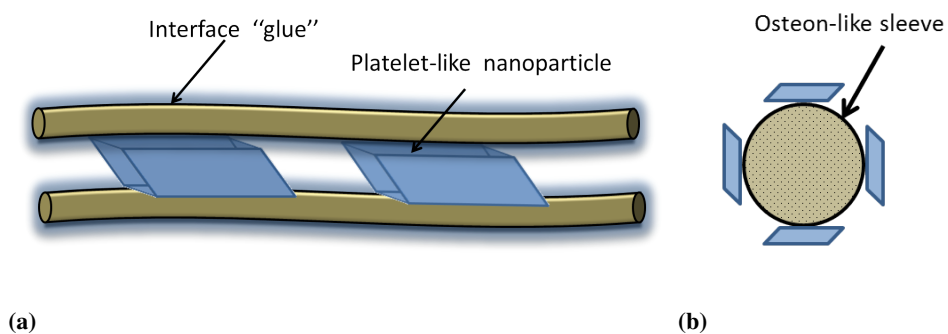


Figure 8.5: Schematic solution based on the results of atomistic simulations. (a) Representation of the osteon structure with improved adhesion at interface and platelet-like nanoparticles, inspired to the hydroxyapatite crystals. (b) Section of the osteon-like sleeve surrounded by platelet-like nanoparticles.

Bibliography

- [1] J. Y. Rho, L. Kuhn-Spearing, and P. Zioupos, “Mechanical properties and the hierarchical structure of bone,” *Medical Engineering & Physics*, vol. 20, no. 2, pp. 92–102, 1998.
- [2] H. Gao, B. Ji, I. Jager, E. Arzt, and P. Fratzl, “Materials become insensitive to flaws at nanoscale: Lessons from nature,” *Proceedings of the National Academy of Sciences*, vol. 100, no. 10, pp. 5597–5600, 2003.
- [3] G. E. Fantner, T. Hassenkam, J. H. Kindt, J. C. Weaver, H. Birkedal, L. Pechenik, J. A. Cutroni, G. A. G. Cidade, G. D. Stucky, D. E. Morse, and P. K. Hansma, “Sacrificial bonds and hidden length dissipate energy as mineralized fibrils separate during bone fracture,” *Nature Materials*, vol. 4, no. 8, pp. 612–616, 2005.
- [4] R. O. Ritchie, M. J. Buehler, and P. Hansma, “Plasticity and toughness in bone,” *Physics Today*, vol. 62, no. 6, pp. 41–47, 2009.

Part V

Appendix

Appendix A

Sample Input Script for LAMMPS

```
#-----  
#           collagen/HAP atomistic model  
#-----  
# Initialization  
units           real  
dimension       3  
boundary        f f f  
neigh_modify    delay 2 every 1  
#-----  
# Settings  
atom_style      full  
bond_style      harmonic  
angle_style     charmm  
dihedral_style  charmm  
improper_style  harmonic  
pair_style      lj/charmm/coul/charmm/implicit 8.0 10.0  
pair_modify     mix arithmetic  
special_bonds   charmm  
processors      64 16 1      #grid 1024 MPI+oMP processes  
#-----  
# Atom definition  
read_data       collagen-HAP.data  
#-----  
# Group info  
group           cterm id 703 1411 2114  
region          1 prism 5 12 4.5 25.5 1 44 -7.2 0 0  
               units box  
group           myfix region 1  
#-----  
# Minimization  
thermo          100  
thermo_style    custom step ke pe etotal temp press pxx  
               pyy pzz  
dump            1 all dcd 4000 minimize.dcd
```

```
min_style      sd
min_modify     dmax 0.5
minimize       0.0 1.0e-8 10000 100000
min_style      cg
min_modify     dmax 0.2
minimize       0.0 1.0e-8 2000 100000
#-----
# Equilibrium
timestep       0.5
fix            fixx myfix spring/self 20.0
velocity       all create 250.0 12345678 dist uniform
fix           2 all nve
fix           1 all langevin 250.0 300.0 1000.0 4279
compute        stressatom all stress/atom
dump           mystr all custom 20000 dump.stress id type x y z
              c_stressatom[1] c_stressatom[2] c_stressatom[3]
              c_stressatom[4] c_stressatom[5] c_stressatom[6]
undump        1
dump          1 all dcd 20000 equilibrium.dcd
restart       1000000 restart.*.equi
run          200000000
#-----
# Steered molecular dynamics
unfix         1
unfix         2
fix          2 all nve
fix          1 all langevin 300.0 300.0 1000.0 48279
fix          pull cterm smd cvel 10.0 0.00001 tether 113.26
              NULL NULL 0.0
undump       1
dump        1 all dcd 4000 stretching.dcd
restart     500000 restart.*.pull
fix        myforce all ave/time 1 100 1000 f_pull[1]
              f_pull[2] f_pull[3] f_pull[4] f_pull[5] f_pull[6]
              f_pull[7] file smd.force
run        200000000
```

Appendix B

Sample Script for Atom Definition in LAMMPS

Created by charmm2lammps v1.8.1 on Sun Jun 3 02:04:18 EDT 2012

```
16077 atoms
 9384 bonds
12909 angles
   0 dihedrals
   0 impropers

 5 atom types
 2 bond types
 1 angle types
 0 dihedral types
 0 improper types

-114.136      403.445 xlo xhi
-108.408      240.861 ylo yhi
 -26.889       50.000 zlo zhi
```

Masses

```
 1      15.999
 2      30.974
 3       40.08
 4      15.999
 5       1.008
```

Pair Coeffs

```
 1  0.252001  3.03253  0.252001  3.03253
 2   0.974    3.48573   0.974    3.48573
 3   0.1186   2.941391   0.1186   2.941391
 4   0.11703  3.092844   0.11703  3.092844
```

```
5          9e-06    1.404235          9e-06    1.404235
```

Atoms

```
1          1          3          2          1.132          14.255          12.038
2          2          3          2          4.712          13.603          6.889
3          3          3          2          2.357          16.269          8.599
4          4          3          2          4.712          13.603          10.308
5          5          3          2          8.199          14.309          8.599
6          6          3          2          3.58           10.23           8.599
7          7          3          2          9.424          10.882          13.748
8          8          3          2          5.937          10.176          12.038
9          9          3          2          9.424          10.882          10.329
10         10         3          2          7.067          16.377          12.038
11         11         4          -1.6          0           16.323          11.66
12         11         5          0.6           0           16.323          10.737
13         12         4          -1.6          0           16.323          8.22
.          .          .          .          .           .           .
.          .          .          .          .           .           .
.          .          .          .          .           .           .
.          .          .          .          .           .           .
.          .          .          .          .           .           .
.          .          .          .          .           .           .
.          .          .          .          .           .           .
.          .          .          .          .           .           .
.          .          .          .          .           .           .
16077      6633      1          -1.4          285.408          38.702          24.559
```

Bond Coeffs

```
1          545          0.96
2          610          1.27
```

Bonds

```
1          1          11          12
2          1          13          14
3          2          15          16
4          2          15          17
.          .          .          .
.          .          .          .
.          .          .          .
.          .          .          .
.          .          .          .
.          .          .          .
.          .          .          .
.          .          .          .
9384      2          16073      16077
```

Angle Coeffs

```
1          82          129.75          77          3.54
```

Angles

1	1	16	15	19
2	1	16	15	18
3	1	16	15	17
.
.
.
.
12909	1	16076	16073	16077

Appendix C

Material Properties

C.1 Carbon Fiber Sleeves

Technical characteristics (from the datasheet).

Geometry: Tubular with woven carbon fibers

Fiber type: carbon

Fiber commercial name: Torayaca T300 67 tex (1k)

Diameter: 2.5-11 mm

Thickness: 0.18 mm

Width: 5 mm

Number of filaments: 40

Weight: 2.75 g/m

Cost: 2.3 €/m

C.2 Glass Fibers

Technical characteristics (from the datasheet).

Class: Rowing

Fiber type: E glass

Commercial name: Glass Roving 2400 tex (silane)

Weight: 2.4 g/m

Density: 2.54 g/cm³

Tensile Strength: 3952 MPa

Young's Modulus: 73 GPa

Strain at break: 3.5-4%

Cost: 2.3 €/m

C.3 Glass-Non-crimp Fabric

Technical characteristics (from the datasheet).

Class: Non-crimp fabric (NCF)

Fiber type: E glass

Fabric type: Interglas 92145, plain wave

Fabric Commercial name: Glass Fabric 220 g/m³ (Aero) Unidirectional (UD)

Weight: 220 g/m²

Cost: 6.73 €/m

Resin consumption: 2.54 g/m² ¹

Laminate thickness: 0.242 mm ¹

Laminate weight: 393 g/m² ¹

C.4 Carbon-Non-crimp Fabric

Technical characteristics (from the datasheet).

Class: Non-crimp fabric (NCF)

Fiber type: carbon

Fabric type: Style 469, plain wave

Fiber commercial name: Torayaca T300J67 tex (1k)

Fabric commercial name: Carbon fabric 93 g/m²

Weight: Carbon fabric 93 g/m²

Cost: 70.24 €/m

Resin consumption: 107 g/cm² ¹

Laminate thickness: 0.149 mm ¹

Laminate weight: 200 g/m² ¹

¹Data referred to a laminate with 35% vol. fibers.

C.5 Resin

Technical characteristics (from the datasheet).²

Density: 1.13-1.17 g/cm³

Viscosity: 700-1100

Equivalent weight: 166-185 g/eq

Refractive index: 1.548-1.552

Cost: 11.2 €/m

C.6 Hardner: RIMH 134

Technical characteristics (from the datasheet).²

Density: 0.93-1 g/cm³

Viscosity: 10-80

Refractive index: 1.49-1.50

Amine value: 550-700 mg_{KOH}/g

Cost: 14.2 €/m

C.7 Hardner: RIMH 137

Technical characteristics (from the datasheet).²

Density: 0.93-0.98 g/cm³

Viscosity: 10-50

Refractive index: 1.460-1.463

Amine value: 400-600 mg_{KOH}/g

Cost: 14.2 €/m

²Data referred to room temperature (*i.e.* 25°).